Tropospheric Carbon Monoxide: Satellite Observations and Their Applications

Stuart Neil MacCallum

Doctor of Philosophy
The University of Edinburgh
2008

Declaration

This thesis has been composed by myself, and all the work reported herein is my own work, except where explicitly otherwise stated.

Stuart MacCallum
August 2008

Acknowledgements

I would like to thank my supervisor Dr. Christopher Merchant for his advice and encouragement. I would also like to thank my second supervisor Dr. David Stevenson, and Dr. Hugh Pumphrey for their assistance.

This work has made use of the resources provided by the Edinburgh Compute and Data Facility (ECDF). (http://www.ecdf.ed.ac.uk/). The ECDF is partially supported by the eDIKT initiative. (http://www.edikt.org.) Many thanks to those involved at the ECDF for providing an excellent computing resource that made much of this work possible.

Thanks also to everyone who helped out from the School of Geosciences. The words of wisdom, computing aid, and laughs were much appreciated.

Thanks to the MacCallums and the Lucies for their support and encouragement.

Finally, special thanks to Alison for all her love and support throughout.

Table of Contents

Abstract

Tropospheric Carbon Monoxide:

Satellite Observations and Their Applications

Carbon monoxide (CO) is present in the troposphere as a product of fossil fuel combustion, biomass burning and the oxidation of volatile hydrocarbons. It is the principal sink of the hydroxyl radical (OH), thereby affecting the concentrations of greenhouse gases such as CH_4 and O_3. Consequently, CO has an atmospheric lifetime of 1-3 months, making it a good tracer for studying the long range transport of pollution.

Satellite observations present a valuable tool to investigate tropospheric CO. The Atmospheric InfraRed Sounder (AIRS), onboard the Aqua satellite, is sensitive to tropospheric CO in ~50 of its 2378 channels. This sensitivity to CO, combined with the daily global coverage provided by AIRS, makes AIRS a potentially useful instrument for observing CO sources and transport.

An optimal estimation retrieval scheme has been developed for AIRS, to provide CO profiles from near-surface altitudes to 150 hPa. Through a validation study, using CO profiles from in-situ aircraft measurements, this retrieval scheme has been shown to provide CO observations with strong correlations to *in situ* measurements. Compared to the operational AIRS v4 CO product this retrieval scheme is shown to provide total column CO retrievals with a reduced bias relative to the *in situ* measurements (~ -10% to ~ -1%). In addition, the optimal estimation retrieval is shown to provide improved estimation and characterization of the retrieval errors.

Further validation work has been carried out through comparison with the established CO observations from the MOPITT instrument, onboard the Terra satellite. Good agreement (correlation coefficient > 0.9, and bias < 1.0 ppbv) between the instruments is observed in the mid-troposphere. At this level, the optimal estimation scheme is shown to remove a positive bias of ~10 ppbv, relative to MOPITT, that is present in the AIRS v4 CO product. The AIRS instrument is also shown to be less sensitive to CO in the lower troposphere than MOPITT. AIRS is also demonstrated to provide fewer pieces of independent information about the vertical structure of CO at tropical latitudes, where higher thermal contrast increases the sensitivity of MOPITT.

Through time series analysis, the capability of AIRS to detect seasonal trends in CO is demonstrated. The potential of AIRS to be used to track, both horizontal and vertical, CO transport is explored. AIRS is shown to be capable of tracking horizontal transport, and to have potential to track vertical transport when combined with another satellite sensor.

Chapter 1. Introduction

1.1. Carbon Monoxide in the Atmosphere

Carbon monoxide (CO) is an important pollutant in the atmosphere. CO abundances range from about ~40 parts per billion (ppb), in regions far from CO sources (e.g. the remote southern hemisphere), to concentrations > 500 ppb in areas of regional scale pollution. In the urban environment or local areas of biomass burning, CO levels can exceed one part per million (ppm) [Novelli, 1999]. The principal direct sources of tropospheric CO are biomass burning and wildfires [Andreae and Merlet, 2001], and anthropogenic emissions from technological sources (e.g. vehicle exhausts and industry) [Olivier *et al.*, 1999]. Biofuels are another significant source of anthropogenic CO emissions. Combined, these sources account for approximately 1350 Tg yr^{-1} (~50%) of the total global CO emissions [Intergovernmental Panel on Climate Change, 2001**].** This high level of contribution from human activities results in CO concentrations in the Northern hemisphere being about twice those in the Southern hemisphere. There are also natural primary sources of CO in the boundary layer, with emissions from the oceans (~50 Tg yr^{-1}) and vegetation (~150 Tg yr^{-1}). Strong emission patterns coupled with a lifetime of 1-3 months [Intergovernmental Panel on Climate Change, 2001] result in large CO gradients in the atmosphere and distinct regional patterns of variability. As there are such significant and (particularly for the case of biomass burning) highly variable CO sources at the surface, the highest and most variable CO concentrations occur in the boundary layer.

In the troposphere there are also significant secondary sources of CO in the form of the oxidation of volatile organic compounds by the hydroxyl radical, OH (~1350 Tg yr^{-1}). This is principally through the oxidation of methane, ~690 Tg yr^{-1}, with a significant contribution from isoprene, ~330 Tg yr^{-1}[Pfister *et al.*, 2008]. The chemical reactions governing CO production through the oxidation of methane (CH_4) via formaldehyde (HCHO) are presented in Eqs. 1.1 to 1.4.

$$CH_4 + OH (+O_2) \rightarrow CH_3O_2 + H_2O \qquad \textbf{(1.1)}$$

$$CH_3O_2 + NO \rightarrow CH_3O + NO_2 \qquad \textbf{(1.2a)}$$

$$CH_3O_2 + HO_2 \rightarrow CH_3OOH + O_2 \qquad \textbf{(1.2b)}$$

$$CH_3OOH + hv \rightarrow CH_3O + OH \qquad \textbf{(1.2c)}$$

$$CH_3O + O_2 \rightarrow HCHO + HO_2 \qquad \textbf{(1.3)}$$

$$HCHO + hv \rightarrow H_2 + CO \qquad \textbf{(1.4a)}$$

$$HCHO + hv \rightarrow H + HCO \qquad \textbf{(1.4b)}$$

$$HCO + O_2 \rightarrow CO + HO_2 \qquad \textbf{(1.4c)}$$

Because CH_4 is well distributed, due to its long lifetime of ~8 years, there is little regional and seasonal variation in its contribution to CO. Granier *et al.* [2000] illustrate that what variation there is occurs between continental and ocean regions, with lower contributions from CH_4 observed over the continents. This is a result of strong chemical loss of OH through higher emissions of isoprene and other VOCs.

The importance of CO in the troposphere lies in its role in affecting the oxidizing capacity of the atmosphere through reaction with OH. CO is the principal sink of OH in the troposphere, accounting for about 50% (1500-2700 Tg yr^{-1}) of the OH sink and may account for about 40-60% of the hydro-peroxy (HO_2) radical production [Kanakidou and Crutzen, 1999]. As a result CO indirectly influences the concentration of greenhouse gases, such as O_3 and CH_4. Kanakidou and Crutzen [1999] demonstrate that a 50% decrease in industrial CO emissions would increase OH by ~3.5%, which would reduce CH_4 concentrations through enhanced photochemical loss. The effect of CO concentrations on O_3 concentrations is strongly dependent on the relative concentration of nitrogen oxides, NO_x. In clean environments, where NO_x concentrations are low, the oxidation of CO by OH reduces O_3 concentrations through reactions with HO_x (Eqns. 1.5 to 1.10).

$$CO + OH \rightarrow H + CO_2 \quad \textbf{(1.5)}$$

$$H + O_2 + M \rightarrow HO_2 + M \quad \textbf{(1.6)}$$

$$HO_2 + O_3 \rightarrow OH + 2O_2 \quad \textbf{(1.7)}$$

$$CO + OH \rightarrow CO_2 + H \quad \textbf{(1.8)}$$

$$H + O_2 + M \rightarrow HO_2 + M \quad \textbf{(1.9)}$$

$$2CO + O_3 + OH \rightarrow 2CO_2 + H_2O \quad \textbf{(1.10)}$$

However, in regions where NO_x concentrations are high (industrial regions and areas of biomass burning) CO is a precursor to the formation of O_3. This occurs through NO_x catalysed reactions with HO_2 (the concentration of which is enhanced by CO). These reactions are detailed in Eqns. 1.5, 1.6, and 1.11 to 1.14.

$$CO + OH \rightarrow H + CO_2 \quad \textbf{(1.5)}$$

$$H + O_2 + M \rightarrow HO_2 + M \quad \textbf{(1.6)}$$

$$HO_2 + NO \rightarrow NO_2 + OH \quad \textbf{(1.11)}$$

$$NO_2 + hv \rightarrow NO + O \quad \textbf{(1.12)}$$

$$O + O_2 + M \rightarrow O_3 + M \quad \textbf{(1.13)}$$

$$CO + 2O_2 \rightarrow O_3 + CO_2 \quad \textbf{(1.14)}$$

Although the chemical reactions of CO leading to production and destruction of O_3 both result in the net production of CO_2 (Eqns. 1.10 and 1.14), the contribution of this *in situ* source is small relative to the total source of CO_2. The net formation (or destruction) of O_3 is very important, as in addition to being a greenhouse gas, tropospheric O_3 is also a harmful pollutant that can cause crop damage and human health problems [Intergovernmental Panel on Climate Change, 2007]. As the interaction of CO with OH has such a significant influence on the chemical composition of the atmosphere, with potential impacts on climate and living matter, it is important that tropospheric CO is well understood.

Although the global CO burden is strongly affected by the CO sources described previously, seasonal trends in CO are dominated by variations in the concentration of

OH. During the summer months in each hemisphere, high levels of solar illumination causes an increase in O_3 photolysis which, through subsequent reaction with H_2O (Eqns. 1.15 and 1.16), raises the OH concentrations and the oxidizing potential of the atmosphere [Edwards *et al.*, 2004].

$$O_3 + hv \rightarrow O(^1D) + O_2 \tag{1.15}$$

$$O(^1D) + H_2O \rightarrow 2OH \tag{1.16}$$

This natural increase in OH allows more CO to be removed from the atmosphere, reducing CO concentrations during the summer months. As the oxidizing potential of the atmosphere exhibits natural seasonal variations, the relative timing of CO emission events becomes important. Edwards *et al.* [2004] show that winter time emissions are relatively more important, as the lifetime of CO is considerably longer during the winter months.

The lifetime of CO (~1-3) months enables CO from major emission events, such as large scale biomass burning, to be transported across large distances around the globe. Therefore, strong CO emission regions can cause significant increases in CO concentrations in areas far from the source, and can consequently impact on air quality and health in these areas. The advent of satellite retrievals of CO offers tremendous opportunity for using CO as a tracer for investigating pollution transport, and also the variability of CO sources.

1.2. CO Observations

1.2.1. Historical Observations

The first measurements of atmospheric CO were made in the late 1940s using spectroscopic techniques [Migeotte, 1949]. In the late 1960s the importance CO to the oxidizing capacity of the atmosphere was realized [McConnell *et al.*, 1971]. This period also saw the development of gas chromatic methods for CO measurements and work using these techniques illustrated variations in CO concentrations with latitude, season, and the degree of pollution in the air mass. Details of the spectroscopic and gas chromatographic techniques for CO measurement are described in detail in Novelli [1999].

Until the end of the 20th century, observations of atmospheric CO were largely limited to those from surface sites and airborne measurement campaigns. However, there were two short-lived space-borne measurement campaigns. The first of these was the Measurement of Air Pollution from Satellites (MAPS) experiment. This nadir viewing gas filter radiometer was flown onboard the Space Shuttle for brief periods in 1981, 1984 and 1994 [Reichle *et al.*, 1999]. MAPS provided the first set of coherent global observations of the distribution of CO in the troposphere and thus gave an insight into the potential of satellite observations of CO. The potential to observe long-range transport of pollution was demonstrated using by Chan *et al.* [2000] and Newell *et al.* [1999]. Connors *et al.* [1999] highlighted the potential of such observations for looking at seasonal variability of CO sources, while Lamarque *et al.* [1999] showed that chemical transport models could be improved through the assimilation of MAPS CO observations.

The second space-borne instrument was the Interferometric Monitor for Greenhouse gases (IMG). It was a high spectral resolution Fourier transform interferometer, flown onboard the ADEOS satellite [Clerbaux *et al.*, 1999]. Unfortunately this instrument was short-lived, providing only nine months of data over 1996 and 1997. Despite its short lifetime, IMG provided an insight into the potential of space-borne high spectral resolution sounders (such as AIRS) for the retrieval of trace gases [Clerbaux *et al.*, 2003]. The retrieval of meteorological parameters (such as temperature and humidity profiles) from IMG spectra was demonstrated by Lubrano *et al.* [2000]. As highlighted by Clerbaux *et al.* [1999] accurate estimates of such parameters is necessary for accurate retrievals of CO. Although both the MAPS and IMG instruments were short-lived, they successfully illustrated the potential of satellite observations to provide a picture of the global distribution and variability of CO.

1.2.2. Current Observations

Since 2000 a number of satellite instruments capable of observing tropospheric CO have become operational. These can be broadly split into four categories, defined by the spectral characteristics (thermal infra-red, short-wave infra-red, and microwave), and the viewing geometries (nadir and limb) of the instruments. Table 1.1 provides a comparison of some of the basic properties of the instruments in each of these categories. From Table 1.1 it is clear that there is a wide range of different operating characteristics in the current satellite instruments. These differences give rise to a variety of CO products, providing information about CO across different altitude ranges.

The first of current satellite instruments to begin operational observations of CO was the Measurements of Pollution in the Troposphere (MOPITT) satellite instrument, launched onboard the TERRA satellite in 1999 [Deeter *et al.*, 2003]. This is a nadir viewing instrument that uses similar technology to the earlier MAPS instrument. MOPITT brought advances in CO observations, with improvements in global coverage and accuracy compared to the earlier space-borne instruments (MAPS and IMG). Continuous observations of CO by MOPITT enabled more extensive investigations into seasonal cycles and interannual variability [Edwards *et al.*, 2004], and improved observations of pollution transport [Heald *et al.*, 2003]. Kar *et al.* [2004] demonstrated that MOPITT retrievals contained information about the vertical structure of CO in the troposphere and proposed that MOPITT could be used in the study of the vertical transport of CO. MOPITT observations of CO have also been used in inverse modeling studies to investigate the variability of CO sources [Heald *et al.*, 2004]. Further details about MOPITT and its CO observations are given in the MOPITT comparison work (Chapter 5**)**. As MOPITT is a well established and extensively validated instrument [Emmons *et al.*, 2004] instrument, it is often used as a benchmark for other satellite instruments, as in this study (Chapter 5).

In addition to MOPITT there are a number of other currently operational satellite instruments that are capable of observing CO. The ENVISAT payload carries two of these instruments: the SCanning Imaging Absorption spectroMeter for Atmospheric CHartographY (SCIAMACHY) [Buchwitz *et al.*, 2005] and the Michelson Interferometer for Passive Atmospheric Sounding (MIPAS) [Belotti *et al.*, 2006]. These are two quite distinct instruments. SCIAMACHY is a nadir viewing instrument measuring scattered, reflected and transmitted solar radiation in the Near Infra-Red (NIR). Its main advantage over MOPITT and other IR sounding instruments is its greater sensitivity to CO in the lower troposphere and boundary layer. SCIAMACHY also operates in a limb-viewing mode but retrievals from such observations are not provided as a routine data product. MIPAS is a limb viewing IR sounder and is only sensitive to CO at altitudes above about 6 km. The NASA Aura satellite also houses two CO sensitive instruments: the Microwave Limb Sounder (MLS) [Filipiak *et al.*, 2005] and the Tropospheric Emission Spectrometer (TES) [Beer, 2006]. As for SCIAMACHY and MIPAS, the two Aura instruments are very different and provide CO information at different levels in the atmosphere. TES is a nadir viewing IR Fourier transform spectrometer, providing CO observations in the troposphere, while MLS operates as its name describes and provides CO measurement in the stratosphere and upper troposphere. TES can also operate in a limb-viewing mode but routine limb-view measurements were discontinued in April 2005 [Rinsland *et al.*, 2006].

We shall consider the Atmospheric Infra-Red Sounder (AIRS). This nadir viewing IR sounding instrument and was launched on board the Aqua satellite in 2002 [Aumann *et al.*, 2003]. Like the other nadir-viewing IR instruments, AIRS is most sensitive to CO in the mid-troposphere [McMillan *et al.*, 2005]. Although it shares similar sensitivity with some of the other instruments, it does offer one distinct advantage, that is, considerably greater global coverage on a daily basis. As CO retrievals from AIRS are the main focus of this work, further details about the instrument are given in §1.2.3.

Instrument Type	**Nadir IR**	**Nadir SWIR**	**Limb Microwave**	**Limb IR**
Operational Example	AIRS, MOPITT, and TES	SCIAMACHY	MLS	MIPAS
λ	~ 4.7 µm	2265–2380 nm	1.2-1.3 mm	4.1-5.5µm
Altitude Sensitivity	MT-UT Low sensitivity in LT	Equal sensitivity from LT to UT	UT and lower stratosphere	MT-UT (> ~6km)
Day/Night Operation	Both	Day	Both	Both

Table 1.1 Intercomparison of the types of CO observing instruments currently operational on satellite platforms. LT, MT, and UT represent lower, mid, and upper-troposphere respectively.

In this brief introduction to CO observations there are two main points to be noted. The first of these is the relatively short period over which global observations of CO have been available from satellite instruments. These new observations provide a means of improving our understanding of CO and consequently, improve our ability to model the chemical, physical and climatological properties of the atmosphere. The second key point to note is the large variety in the satellite instruments, both in terms of the methods they use and the form of the CO observation they provide. Such diversity presents us with potentially vast amounts of information about CO. However, at the same time it poses new problems in deciphering the true picture of CO from such different types of observations, and in maximizing the information through combinations of these instruments.

1.2.3. The Atmospheric Infra-Red Sounder (AIRS)

The AIRS instrument, launched onboard NASA's Aqua satellite in 2002, is a cross-track scanning grating spectrometer with 2378 high spectral resolution channels covering a spectral range of ~3.7 to ~16µm [Aumann *et al.,* 2003] . Aqua operates in a sun-synchronous, near-polar orbit, at an altitude of 705.3 km. Some further characteristics of the Aqua satellite are given in Table 1.2.

Launch Date	May 4, 2002
Equatorial Crossing	1:30 p.m., ascending node
Altitude	705.3 km
Inclination	98°
Period	99 minutes
Eccentricity	0.0015
Instrument Payload	Atmospheric Infra-Red Sounder (AIRS) Advanced Microwave Sounding Unit (AMSU) Humidity Sounder for Brazil (HSB) Advanced Microwave Scanning Radiometer for EOS (AMSR-E) Moderate-Resolution Imaging Spectroradiometer (MODIS) Clouds and the Earth's Radiant Energy System (CERES)

Table 1.2 General information about the Aqua satellite, including details of orbit characteristics and the payload.

AIRS measures the outgoing infra-red radiation at the top of the atmosphere at high spectral resolution ($\lambda\backslash\Delta\lambda = 1200$) in three non-contiguous wavelength bands (given in Table 1.3). An example AIRS spectrum for a cloud-free ocean footprint is shown in Figure 1.1. The AIRS scan geometry and characteristics (detailed in Figure 1.2 and Table 1.3) give AIRS nearly full global coverage twice daily (day and night). This excellent spatial and temporal coverage is one of the key advantages of the AIRS instrument, as will be discussed in later chapters.

Spectral Coverage	3.74 - 4.61 µm 6.20 - 8.22 µm 8.80 - 15.4 µm
Spectral Resolution	$\lambda\backslash\Delta\lambda = 1200$
Instrument Field of View	1.1°
Scan Angle	±48.95
Ground Footprint	90 per scan, 22 ms per footprint
Swath width	1650 km
Radiometric Calibration	± 3% absolute error

Table 1.3 Characteristics of the Atmospheric Infra-Red Sounder (AIRS).

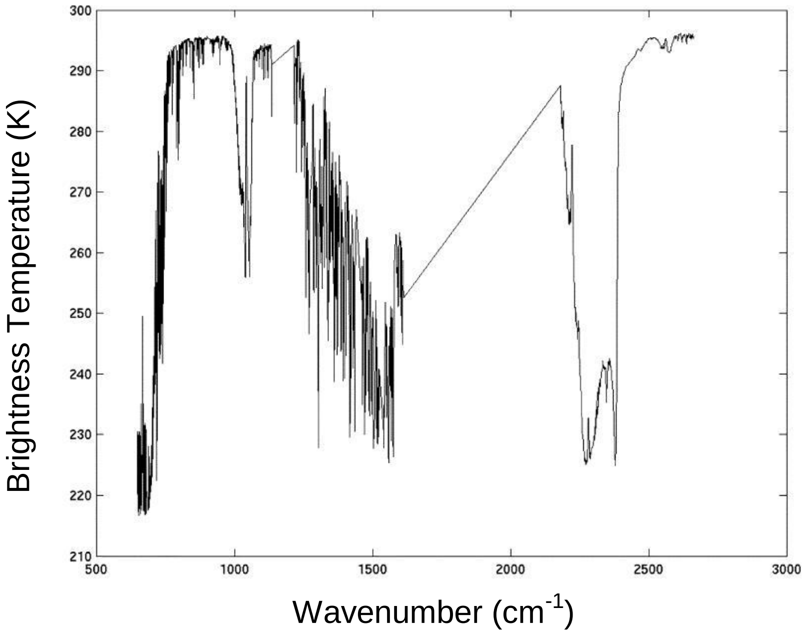

Figure 1.1 Example of the full AIRS spectrum, taken from Aumann *et al.* [2003]. This spectrum is from a single cloud-free ocean footprint.

AIRS operates in synchronous with another of Aqua’s instruments, the Advanced Microwave Sounding Unit (AMSU), in a system designed to provide new and improved measurements of cloud properties, atmospheric temperature and humidity, and surface temperatures. The scan geometries of the two instruments are shown in Figure 1.2. AIRS has a spatial resolution of 13.5 km at nadir, while AMSU provides coverage at a resolution of 40 km at nadir. The two instruments operate such that each AMSU footprint is collocated with a set of 3x3 AIRS footprints, as shown in

Figure 1.2. These sets of 3x3 AIRS observations are used to determine the AIRS "cloud cleared radiance" product (described in §3.6.1), used in the CO retrieval scheme developed in this project (Chapter 3). Among the measurement improvements offered by AIRS is the ability to obtain atmospheric temperature and humidity profiles with accuracy equivalent to radiosondes: temperature profiles with 1K accuracy in 1 km vertical layers, and humidity profiles accurate to 10% in 2 km layers. Such an improvement in satellite retrievals meets the level of accuracy and the global coverage required for improvements in numerical weather prediction (NWP), one of the main objectives of the AIRS instrument suite.

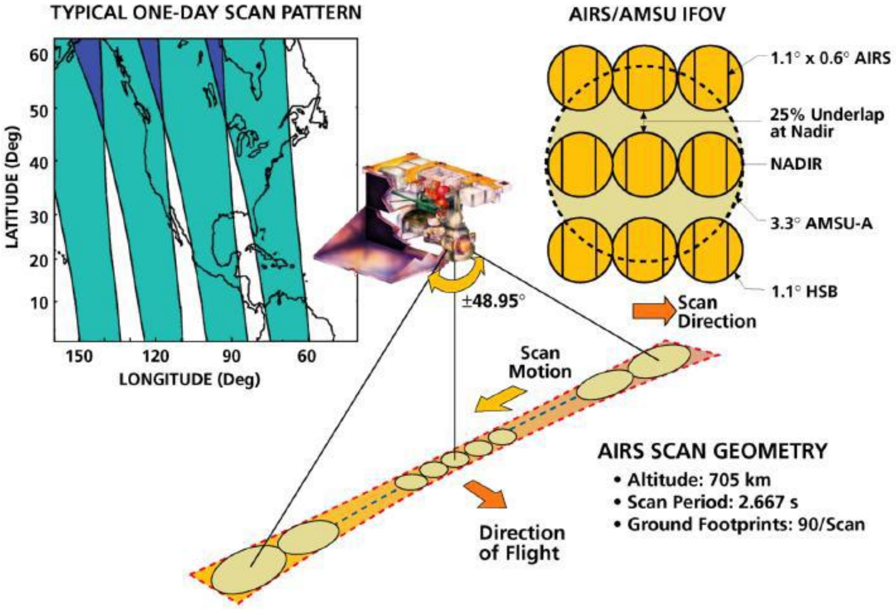

Figure 1.2 AIRS scan geometry and typical one-day scan pattern. Image taken from http://www-airs.jpl.nasa.gov/

The ability of the AIRS/AMSU system to measure the key elements of the atmospheric state to high accuracy and precision is not only useful for NWP, but also benefits retrievals of other atmospheric constituents such as CO. Improvements in such retrievals should follow from better characterization of the atmospheric state, as uncertainties in the retrieval scheme are reduced.

For CO retrievals, only ~50 of the 2378 channels are sensitive to CO (Chapter 3), and are used in the retrieval scheme. Although not used directly for CO retrievals, many of the other AIRS channels are involved in the CO retrieval through their contribution to the retrievals of temperature and water vapour. The channels used for CO retrievals lie at the edge of the 3.74 - 4.61 μm AIRS measurement band, close to the 1.0 vibration-rotation CO fundamental at 4.67 μm [Goody and Yung, 1995]. Utilising cloud-cleared radiances [Chahine, 1974] in this spectral region enables CO retrievals to be made using AIRS even in the presence of significant cloud cover [Susskind *et al.*, 2003]. It is the high density global coverage that makes AIRS a particularly useful instrument for observing CO.

1.2.4. Development of a New CO Retrieval Scheme for AIRS

The AIRS CO product (v4), the operational product through the time period of this study[1], uses a retrieval scheme based on the singular value decomposition (SVD) of a set of empirically determined, vertically overlapping representation functions [McMillan *et al.*, 2005]. The CO retrieval methodology (described in more detail in Chapter 3) follows that outlined by Susskind *et al.* [2003] for AIRS O_3 retrievals and uses the forward radiative transfer model described by Strow *et al.* [2003]. McMillan *et al.* [2005] demonstrated that AIRS CO retrievals were accurate to ~10% in the northern hemisphere and highlighted the potential of AIRS to provide insights into an aspect of the global carbon cycle.

Although the success of the AIRS v4 CO product has been demonstrated by McMillan *et al.* [2005] an alternative retrieval scheme, based on optimal estimation techniques [Rodgers, 2000], is developed here. This is done in order to provide an independent assessment of the use of AIRS for CO observation using a more optimal and theoretically sound method (e.g. as used for the MOPITT [Deeter *et al.*, 2003] and TES [Bowman *et al.*, 2006] instruments). As well as providing an independent validation of the AIRS CO product, it is thought that the optimal estimation method may offer improvements in the quality of the retrieval error information, a key feature of any retrieval product if it is to be used in quantitative analysis [Luo *et al.*, 2007].

---

[1] On 25th July 2007 a new AIRS CO product (v5) was launched by the AIRS science team. Further details of this are given in Appendix A.

1.3. Objectives of This Study

The first objective of this study is to develop an alternative CO retrieval scheme for the AIRS instrument. Due to its unique ability to provide near-global coverage on a daily basis AIRS has great potential for monitoring global CO. Use of optimal estimation methods [Rodgers, 2000] should offer improvements over the AIRS v4 CO product, particularly in the quality of the error estimates and in understanding the informational aspects of CO retrieval. As such, the techniques of Rodgers [2000] are applied to the problem of CO retrievals from AIRS.

Following from the development of an optimal estimation retrieval scheme for CO, this study shall validate the new CO product and explore its performance. This is done through comparisons with in-situ aircraft measurements and the well established MOPITT CO product.

Finally, some of the potential of this new CO product for the analysis of global CO is demonstrated. This is achieved through analysis of an annual CO data set, investigating global and regional variations in CO and exploring the potential of AIRS for tracking the transport of pollution.

A brief description of each chapter is as follows:

Chapter 2. An introduction to the theory of the optimal estimation retrieval methods used in this study, and alternative retrieval methods, including that used in the operational AIRS CO retrieval algorithm.

Chapter 3. The application of the theory of *chapter 2* to the specific task of measuring atmospheric CO concentrations from AIRS. This chapter outlines the development of the retrieval scheme and describes in more detail the AIRS retrieval algorithm.

Chapter 4. Validation of the new retrieval scheme with in-situ aircraft measurements.

Chapter 5. A global comparison study of the new AIRS CO retrieval with the AIRS v4 and MOPITT CO products. The relative performance of the new CO product is explored.

Chapter 6. Seasonal trends in global and regional CO in the mid-troposphere. The potential of AIRS for showing source variability and CO transport is demonstrated through time series analysis.

Chapter 7. A case study looking at CO emissions from biomass burning in Indonesia in October 2006.

Chapter 8. Summary and future work.

Chapter 2. Retrieval Theory

2.1. Fundamentals of Inverse Theory

The *inverse problem* refers to the challenge of inferring something about the atmospheric state from indirect instrument measurements (e.g. the CO concentration from a satellite instrument's radiances). In order to solve the *inverse problem*, it is necessary to understand the process of measurement. This will be expressed by a *forward model*, which describes the physics of the measurement process. For the case where the instrument response is linear with changing atmospheric state, the measurement process can be expressed as:

$$\mathbf{y} = \mathbf{F}(\mathbf{x}) + \boldsymbol{\varepsilon} = \mathbf{Kx} + \boldsymbol{\varepsilon}. \qquad \textbf{2.1}$$

Here, the instrument measurements are represented by **y**, the *measurement vector*, with dimension *m*. The atmospheric state is defined by the *n*-dimensional state *vector*, **x** (e.g. a vertical profile of CO concentrations). The relationship between state and measurement vectors is described by the forward model, **F(x)**, which is an approximation to the detailed physics of the atmosphere. It is also necessary to include an estimate of the measurement and forward modelling error, **ε**.

If the forward model, **F(x),** is linear within the error bounds of the retrieval, it can be represented by the $m \times n$ *weighting function matrix*, **K**. Each element of **K** is the partial derivative of a forward model element with respect to a state vector element, i.e. $K_{ij} = \dfrac{\partial F_i(\mathbf{x})}{\partial x_j}$. These weighting functions describe the sensitivity of the instrument measurements to different elements of the state vector, e.g. the sensitivity of channel radiances to temperature at different altitudes in the atmosphere, as shown in Figure 2.1. Defining the forward model in this way reduces the problem to that of solving a set of linear equations. If $m < n$, there are fewer measurements than unknowns, the problem is under-constrained. If $m > n$ the equations may be over-constrained if the *m* channels are highly independent. It is possible for there to be more measurements than unknowns ($m > n$) and for the set of equations to be under-constrained. This occurs when each measurement contains essentially the same information about the state, **x**, as is the case for CO retrievals using AIRS (Chapter 3). Weighting functions of this form are frequently available as an output product from radiative transfer models that may be used as the forward model. Alternatively they can be obtained by brute force methods, running the forward model for different perturbations of the state.

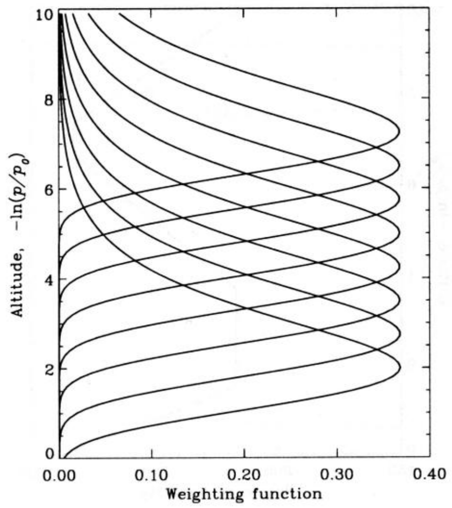

Figure 2.1 A set of synthetic weighting functions representing a typical nadir sounder measuring thermal emission. The vertical coordinate is –ln(p/p_0), where p is pressure and p_0 is surface pressure. Taken from Rodgers [2000].

2.2. The Maximum a Posteriori Solution (MAP)

2.2.1. Bayes' Theorem

When measurement error is considered, a range of values of **x** exist such that **F(x)** agrees with **y** to within **ε**. It is therefore necessary to describe the uncertainty in the measurements and the resulting uncertainty in the retrievals. Rodgers [2000] (§2.3 and §4.1) derives a method for doing this based on Bayes' theorem of probability. Bayes' theorem defines the probability density function (*pdf*) of the state vector, **x** given the measurement vector, **y**. This is known as the posterior *pdf*, given by:

$$P(\mathbf{x}|\mathbf{y}) = \frac{P(\mathbf{y}|\mathbf{x})P(\mathbf{x})}{P(\mathbf{y})}, \qquad \mathbf{2.2}$$

where:

P(**x**) is the prior *pdf* of the state **x**, meaning P(**x**)d**x** is the probability before measurement that **x** lies within the range (**x**, **x** + d**x**).

P(**y**) is the prior *pdf* of the measurement, **y**. In practice this is only a normalising factor and can often be ignored.

P(**y**|**x**) is the conditional *pdf* of **y** given **x**. This is the *pdf* describing the probability of **y** for a particular value of **x**.

2.2.2. Prior Information and Covariance Matrices

Considering the inverse problem in this way introduces the concept of having prior information about both the state and measurement vectors, including information about their errors. It is common in retrieval schemes to start with some initial estimate of the state vector. In optimal estimation methods, such as MAP, this is referred to as the *a priori*, $\mathbf{x_a}$. This could be as basic as a fixed value of the parameter of interest at all levels in the atmosphere, but is typically determined from sources such as climatology or model output. Accompanying the *a priori* is the *prior covariance matrix,* $\mathbf{S_a}$, equivalent to P(**x**) in Bayes' theorem. $\mathbf{S_a}$ is a square matrix of dimension *n*, with diagonal elements equal to the variances of the elements of $\mathbf{x_a}$. Along with this measure of the uncertainty of the $\mathbf{x_a}$, the off-diagonal elements of $\mathbf{S_a}$ represent the prior knowledge of correlations between different elements of $\mathbf{x_a}$, typically correlations between different atmospheric levels. As with the *a priori*, the covariance matrix $\mathbf{S_a}$ can be derived from sources such as climatology, model output, or a training set of *in situ* data. This prior information acts as both a starting point for the retrieval and as a constraint for cases where the information about **x** contained with the measurements is limited. If there is little information about **x** in the measurements or the noise levels are high, the retrieval and its associated error covariance matrix will tend to those of the prior.

Prior knowledge of the experimental error is also represented by a covariance matrix, $\mathbf{S}_\varepsilon$. In its most basic form the *observational error covariance matrix* will contain the estimated instrumental noise in the measurements, **y**, in the form of variances held in its diagonal elements. Further to this the off-diagonal elements may contain information about any inter-channel correlations. As shall be outlined, errors in the forward model are also incorporated into $\mathbf{S}_{\varepsilon}$.

The instrument measurement and its uncertainty (and therefore that of the forward model) may be affected by a number of parameters defining the atmospheric state. It is not necessary to include these in the state vector **x** and perform retrievals of them. Instead, it is possible to consider the problem as a retrieval of **x**, and incorporate the uncertainty in the other forward model parameters **b** in the error covariance matrix, $\mathbf{S}_{\varepsilon}$. This method allows retrievals of **x** to be made using model parameters, **b**, from independent retrievals (or other sources such as climatology), while still accounting for the effect of their uncertainty in the retrieval of **x**, using the substitution:

$$\mathbf{S}_{\varepsilon} \rightarrow \mathbf{S}_{\varepsilon} + \mathbf{K}_b \mathbf{S}_b \mathbf{K}_b^T . \qquad \mathbf{2.3}$$

Here $\mathbf{K}_\mathbf{b}$ and $\mathbf{S}_\mathbf{b}$ represent the weighting functions and the error covariance matrix for the model parameters, **b**.

2.2.3. MAP

Bayes' theorem provides a framework for introducing prior knowledge of the instrument characteristics and the parameter we are attempting to measure, along with information about uncertainties in both. This framework can be developed to find the profile, $\hat{\mathbf{x}}$, for which P(**x**|**y**) has the highest value. Rodgers [2000] defines this solution as the *Maximum A Posteriori* (MAP) method and describes it in detail. A brief summary follows.

Errors in real measurements are usually represented by Gaussian statistics, so the *pdfs* can be assumed to take the form of a Gaussian distribution of the form:

$$P(\mathbf{v}) = \frac{1}{(2\pi)^{\frac{n}{2}} |\mathbf{S}|^{\frac{1}{2}}} \exp\left(-\frac{1}{2} (\mathbf{v} - \bar{\mathbf{v}})^T \mathbf{S}^{-1} (\mathbf{v} - \bar{\mathbf{v}}) \right), \qquad \mathbf{2.4}$$

where **v** is a random vector with mean $\bar{\mathbf{v}}$ and covariance matrix **S**.

Taking the natural logarithm of this equation, the terms of Eq. 2.2 can be written as:

$$-\ln P(\mathbf{x}) = (\mathbf{x}-\mathbf{x}_a)^T \mathbf{S}_a^{-1}(\mathbf{x}-\mathbf{x}_a) + c_1 \qquad \mathbf{2.5}$$

and

$$-\ln P(\mathbf{y} \mid \mathbf{x}) = (\mathbf{y}-\mathbf{Kx})^T \mathbf{S}_\varepsilon^{-1}(\mathbf{y}-\mathbf{Kx}) + c_2, \qquad \mathbf{2.6}$$

where c_1 and c_2 are constants.

Substituting Eqs. 2.5 and 2.6 into Eq. 2.2 and assuming a Gaussian distribution for the posterior *pdf*, with expected value $\hat{\mathbf{x}}$ and covariance $\hat{\mathbf{S}}$, Rodgers [2000] shows that the MAP solution for $\hat{\mathbf{x}}$ can be written as:

$$\hat{\mathbf{x}} = \mathbf{x}_a + \left(\mathbf{K}^T\mathbf{S}_\varepsilon^{-1}\mathbf{K} + \mathbf{S}_a^{-1}\right)^{-1}\mathbf{K}^T\mathbf{S}_\varepsilon^{-1}(\mathbf{y}-\mathbf{Kx}_a), \qquad \mathbf{2.7}$$

with covariance:

$$\widehat{\mathbf{S}} = \left(\mathbf{K}^T\mathbf{S}_\varepsilon^{-1}\mathbf{K} + \mathbf{S}_a^{-1}\right)^{-1}. \qquad \mathbf{2.8}$$

The retrieved state, $\hat{\mathbf{x}}$ (Eq. 2.7), is the most probable state, given the measurements and prior knowledge of the state and the forward model. Eq. 2.8 returns the covariance matrix of the retrieved state, providing information about the uncertainty in the retrieval and the sources of this uncertainty (see §2.2.5). Through comparison of $\hat{\mathbf{S}}$ and $\mathbf{S_a}$ the relative contribution of $\mathbf{x_a}$ to the retrieval can be determined.

2.2.4. The Gain Matrix and the Averaging Kernels

The *gain matrix* **G** can be described as a generalised inverse of **K**. It is a measure of the sensitivity of the retrieval to the measurements, which is the same as the sensitivity to measurement error. It can be expressed as:

$$\mathbf{G} = \left(\mathbf{K}^T\mathbf{S}_\varepsilon^{-1}\mathbf{K} + \mathbf{S}_a^{-1}\right)^{-1}\mathbf{K}^T\mathbf{S}_\varepsilon^{-1}. \qquad \mathbf{2.9}$$

The *averaging kernel matrix*, **A**, provides a measure of the sensitivity of the retrieved state to the true state. It is the product of the gain matrix and the weighting function matrix.

$$\mathbf{A} = \frac{\partial\hat{\mathbf{x}}}{\partial\mathbf{x}} = \mathbf{GK}. \qquad \mathbf{2.10}$$

This is an extremely useful quantity as it provides information about the source of the retrieved values, $\hat{\mathbf{x}}$, in terms of contributions from different elements of the true state vector, **x**. For example, in a retrieval of a profile of CO, **A** can reveal whether the retrieved CO amount at a given altitude is truly a measure of CO at that altitude or if it contains strong contributions from CO at other altitudes. The rows of **A** represent the relative contribution of the true state, **x**, to the retrieved state, $\hat{\mathbf{x}}$, for each level in the profile. In the ideal case **A** would be a unit matrix. In reality, the rows of **A** are generally peaked functions, as in Figure 2.2. The level at which they peak indicates which level of **x** is dominating the value of $\hat{\mathbf{x}}$ at the level corresponding to the given row of **A**. Ideally the rows of **A** would peak at the level of $\hat{\mathbf{x}}$ that they correspond to. However, this may not always be the case and it is possible for $\hat{\mathbf{x}}$ at a given level to be dominated by the true state at a different level.

In the example of the CO profile retrieval, another useful piece of information that can be derived from the rows of **A** is the vertical resolution of the profile. An optimistic estimation of this is the *full width at half maximum* (FWHM) of the rows of **A**. Any profile features smaller than this will be smoothed out in the retrieved profile.

The number of independent pieces of information about **x** contained in the measurement can be estimated as the number of *degrees of freedom for signal* (DOFS). Considering the general case of measuring a vector **y** with *m* degrees of freedom and assuming Gaussian statistics, the most probable state is the one which minimises

$$\chi^2 = (\mathbf{x}-\mathbf{x}_a)^T \mathbf{S}_a^{-1}(\mathbf{x}-\mathbf{x}_a) + \varepsilon^T \mathbf{S}_\varepsilon^{-1}\varepsilon, \qquad \textbf{2.11}$$

where $\varepsilon = \mathbf{y} - \mathbf{Kx}$. From Eqs. 2.7 and 2.9 the minimum of this function occurs at

$$\hat{\mathbf{x}} - \mathbf{x}_a = \mathbf{G}(\mathbf{y} - \mathbf{Kx}_a) = \mathbf{G}[\mathbf{K}(\mathbf{x}-\mathbf{x}_a) + \boldsymbol{\varepsilon}]. \qquad \textbf{2.12}$$

At this minimum the expected value of χ^2 is equal to the number of degrees of freedom, which is equal to the number of measurements, *m*. This value can be split into a contribution from the signal (d_s) and the degrees of freedom for noise (d_n).

$$d_s = \mathrm{E}\left\{(\hat{\mathbf{x}}-\mathbf{x}_a)^T \mathbf{S}_a^{-1}(\hat{\mathbf{x}}-\mathbf{x}_a)\right\} \qquad \mathbf{2.13}$$

$$d_n = \mathrm{E}\left\{\hat{\varepsilon}^T \mathbf{S}_\varepsilon^{-1}\hat{\varepsilon}\right\} \qquad \mathbf{2.14}$$

Rodgers [2000] shows that this measure of the information content can be calculated from the averaging kernel matrix, defining it as the trace of **A**:

$$d_s = tr(\mathbf{A}). \qquad \mathbf{2.15}$$

A visual estimation of the number of degrees of freedom of the signal can be made by looking at the averaging kernels. Roughly speaking, each distinct peak at unity on different levels corresponds to one degree of freedom of the signal. As the degree of overlap between averaging kernels increases, the number of degrees of freedom of the signal will decrease.

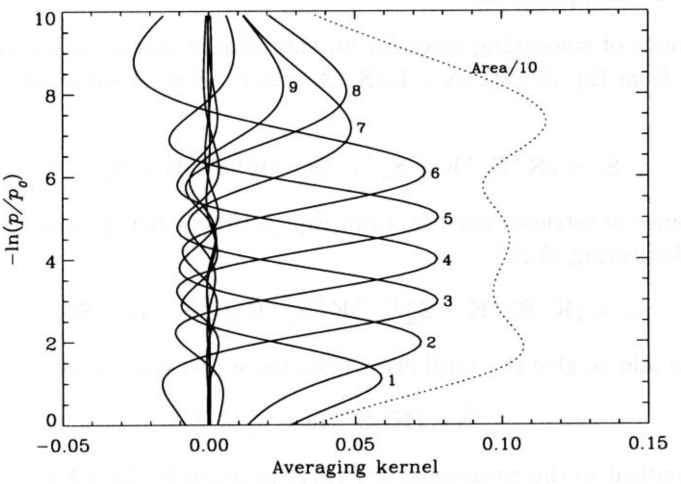

Figure 2.2 Averaging kernels for the simulated nadir temperature sounding case, from Rodgers [2000]. The vertical coordinate is $-\ln(p/p_0)$, where p is pressure and p_0 is surface pressure. The dotted line represents the total integrated area under the averaging kernels.

2.2.5. Retrieval Errors

In some cases where the problem is slightly non-linear, a solution can be found by linearizing the forward model about some reference state. Taking the reference state to be the prior state (not essential but often convenient) $\mathbf{x} = \mathbf{x}_a$ and $\mathbf{b} = \hat{\mathbf{b}}$, where $\hat{\mathbf{b}}$ is the best estimate of the forward model parameters, the retrieved state can be written as:

$$\hat{\mathbf{x}} = \mathbf{x}_a + \mathbf{A}(\mathbf{x} - \mathbf{x}_a) + \mathbf{G}\varepsilon_y, \qquad \mathbf{2.16}$$

where $\varepsilon_y = \mathbf{K}_b(\mathbf{b} - \hat{\mathbf{b}}) + \varepsilon$, and represents the total error relative of the measurement and forward model.

The total error can be considered to be the difference between the true state and the retrieved state and can be written as:

$$\hat{\mathbf{x}} - \mathbf{x} = (\mathbf{A} - \mathbf{I})(\mathbf{x} - \mathbf{x}_a) + \mathbf{G}\varepsilon + \mathbf{G}\mathbf{K}_b(\mathbf{b} - \hat{\mathbf{b}}). \qquad \mathbf{2.17}$$

This can be decomposed into three terms each representing a different source of contribution to the total error in the retrieval.

1. The smoothing error, $(\mathbf{A}\text{-}\mathbf{I})(\mathbf{x}\text{-}\mathbf{x}_a)$, is the error associated with the smoothing of the true state by the averaging kernels. Its covariance matrix is given by:

$$\mathbf{S}_s = (\mathbf{A} - \mathbf{I})\mathbf{S}_a(\mathbf{A} - \mathbf{I})^T. \qquad \mathbf{2.18}$$

2. The measurement error, $\mathbf{G}\boldsymbol{\varepsilon}$, is the error due to instrumental noise and has a covariance matrix of:

$$\mathbf{S}_m = \mathbf{G}\mathbf{S}_\varepsilon\mathbf{G}^T. \qquad \mathbf{2.19}$$

3. The model parameters error, $\mathbf{G}\mathbf{K}_b(\mathbf{b} - \hat{\mathbf{b}})$, represents the error in the retrieval due to uncertainty in the model parameters. Its covariance matrix is given by:

$$\mathbf{S}_p = \mathbf{G}\mathbf{K}_b\mathbf{S}_b(\mathbf{G}\mathbf{K}_b)^T. \qquad \mathbf{2.20}$$

Combining these error covariance matrices gives the total error covariance matrix.

$$\mathbf{S}_T = \mathbf{S}_s + \mathbf{S}_m + \mathbf{S}_p. \qquad \mathbf{2.21}$$

This is identical to the *a posteriori* error covariance matrix given by Eq. 2.8. The ability to break down the total error into these components is a useful diagnostic tool for evaluating the performance of a retrieval scheme.

2.2.6. The Non-Linear Case

In the previous sections the methodology for solving linear or nearly linear problems (where linearization around a prior state is adequate) has been defined. For moderately non-linear problems the linearization about a prior state is still sufficient for error analysis, but is no longer suitable for finding a solution. To find the optimal solution for a moderately non-linear problem, further numerical and iterative methods must be employed.

One possible approach to solving the moderately non-linear case is the Gauss-Newton iterative method. From the Bayesian solution for the linear problem Rodgers [2000] shows that the maximum probability state $\hat{\mathbf{x}}$ can be obtained by finding the zero of the gradient of the cost function:

$$-2\ln P(\mathbf{x}\,|\,\mathbf{y}) = [\mathbf{y}-\mathbf{F}(\mathbf{x})]^T \mathbf{S}_\varepsilon^{-1}[\mathbf{y}-\mathbf{F}(\mathbf{x})] + [\mathbf{x}-\mathbf{x}_a]^T \mathbf{S}_a^{-1}[\mathbf{x}-\mathbf{x}_a] + c, \qquad \mathbf{2.22}$$

where c is a constant. At each iteration, i, to find the zero gradient of the cost function, the retrieved state can be expressed as:

$$\mathbf{x}_{i+1} = \mathbf{x}_a + \left(\mathbf{S}_a^{-1} + \mathbf{K}_i^T \mathbf{S}_\varepsilon^{-1} \mathbf{K}_i\right) \mathbf{K}_i^T \mathbf{S}_\varepsilon^{-1}\left[\mathbf{y} - \mathbf{F}(\mathbf{x}_i) + \mathbf{K}_i(\mathbf{x}_i - \mathbf{x}_a)\right], \qquad \mathbf{2.23}$$

where $\mathbf{x}_i$ is the most recent retrieved state and $\mathbf{K}_i = \mathbf{K}(\mathbf{x}_i)$.

The cost function for a moderately non-linear problem may be seriously non-quadratic away from the solution. In such a case, the Gauss-Newton may unsuitable, resulting in slow convergence or convergence to a solution that may even increase rather than decrease the residual. For problems of this nature, an alternative iterative scheme, such as the Levenberg-Marquardt method, is required. The Levenberg-Marquardt method introduces a parameter, γ, that is used to control the step size at each iteration. Rodgers [2000] describes an example of this method in more detail and defines the retrieved state at the i_{th} iteration of the Levenberg-Marquardt method to be:

$$\mathbf{x}_{i+1} = \mathbf{x}_i + \left[(1+\gamma_i)\mathbf{S}_a^{-1} + \mathbf{K}_i^T \mathbf{S}_\varepsilon^{-1} \mathbf{K}_i\right]^{-1} \left\{\mathbf{K}_i^T \mathbf{S}_\varepsilon^{-1}[\mathbf{y} - \mathbf{F}(\mathbf{x}_i)] - \mathbf{S}_a^{-1}[\mathbf{x}_i - \mathbf{x}_a]\right\}, \qquad \mathbf{2.24}$$

where γ_i is the step size parameter at the i_{th} iteration. At each step in the iteration, the value of γ_i is updated based on the change in the cost function, controlling both the direction of descent and the step size. There are numerous potential methods that may be used to select a value for γ_i at each step in the iteration, and also a number of variants of the method described in Rodgers [2000]. As the Levenberg-Marquardt method tends to be more computationally expensive, the simpler Gauss-Newton method was preferred for use in the retrieval scheme developed in this project. Using the Gauss-Newton method convergence to a solution was typically achieved in a small number of iterations, indicating that this method is suitable for this project.

In any iterative scheme, some test for convergence is required. The aim of such a test is to allow enough iterations to return a solution close to the true maximum probability state, say an order of magnitude smaller than the error of the solution. At the same time the scheme must avoid unnecessary iterations that would be required to result in no change in the solution at machine precision. There are three different kinds of tests for convergence that can be applied at each iteration. Checks can be made on the size of (a) the reduction of the cost function, (b) the gradient of the cost function, or (c) the step size (in state or measurement space). One possible test is to look at the size of the radiance residuals, $\boldsymbol{y} - \boldsymbol{F}(\boldsymbol{x}_i)$, at each iteration. These will tend to zero with successful convergence. For retrievals of CO using AIRS, the measurement vector, and therefore the vector of residuals, consists of over 50 elements (Chapter 3). To simplify the decision making process for convergence an alternative single-value test was sought. Rodgers [2000] defines such a test for cases where $n \leq m$ as:

$$d_i^2 = (\mathbf{x}_i - \mathbf{x}_{i+1})^T \hat{\mathbf{S}}^{-1} (\mathbf{x}_i - \mathbf{x}_{i+1}) << n \qquad \textbf{2.25}$$

This is an inexpensive test to carry out as $\hat{\mathbf{S}}^{-1}$ is already calculated as part of the iteration, Eqs. 2.8 and 2.23. As this test is straightforward to implement and requires minimal additional computation, it was selected for use in the retrieval scheme developed during this project.

2.3. Alternative Retrieval Methods

2.3.1. Introduction

Rodgers [2000] states that in "most circumstances the maximum amount of information will be extracted from a set of measurements when we use a full non-linear retrieval which minimises a cost function based on all of the data and an appropriate *a priori*". Such methods (i.e. MAP) are described as optimal estimation techniques. There are a variety of other methods of solving the inverse problem, outlined in depth by Rodgers [2000]. Some of these will be briefly described here to give an introduction to alternative methods.

2.3.2. Representation Functions and the Constrained Exact Solution

In this method a set of continuous functions, such as sines and cosines, or polynomials are defined to represent the profile. These representation functions **W** are combined with the weighting functions **K**, reducing the problem to that of solving a set of simultaneous equations, given by **C=KW**. The solution is given by:

$$\hat{\mathbf{x}} = \mathbf{W}(\mathbf{KW})^{-1}\mathbf{y} = \mathbf{Gy}. \qquad \mathbf{2.26}$$

If suitable representation functions are used then this method performs well in the absence of noise. However, even small levels of noise can result in the very poor retrievals. The gain matrix, **G**, is equivalent to that of 2.9, and provides a measure of the sensitivity to measurement error. If the matrix **C=KW** is ill-conditioned then the sensitivity to measurement error, through **G**, may be large. This can be a particular problem for instruments with significant overlap between influence functions, where **K** is nearly singular. In such cases, differences arising from noise are wrongly interpreted as reflecting subtle information about the state and can result in extremely inaccurate retrievals. A better choice of representation functions can improve the retrievals but the determination of the optimal representations can be somewhat of an ad-hoc process. There are two other important points to be taken from this. The first is that the measurements cannot provide all the information about the profile. The second is that it is an unreasonable expectation to be able to find an exact solution. A solution within the bounds of experimental error is a more sensible target.

As is shown in §3.3, there is significant overlap in the influence functions for CO retrievals using the AIRS instrument. Consequently, a representation function solution may not be suitable for such retrievals. However, the addition of some constraints to the representation function solution can limit the inherent problems with noise. This is known as the constrained exact solution and a form of this is used in the operational AIRS CO retrieval algorithm, developed by the AIRS science team. Their method applies singular value decomposition to the matrix of simultaneous equations, **C**. This enables eigenvalues that contribute more to the error term than the profile to be dropped, thus constraining the retrieval. The method used in the operational AIRS CO retrieval algorithm is described in more detail in §3.7.

2.3.3. Least Squares Solution

This method minimises the sum of the squares of the differences between the actual measurements and those calculated from the forward model. For the non-linear case, linearization about some estimate of the solution results in equations similar to those from optimal methods. In essence it is the optimal estimation solution with no *a priori* information.

2.3.4. Twomey-Tikhonov

This method was the first to tackle the issues of error sensitivity and constraints in the retrieval problem. It is based on the minimisation of a cost function that includes departures of the solution from both the measurements and an *a priori*. The balance of this trade off is achieved through subjective tuning of a weighting parameter, an obvious disadvantage over optimal methods.

2.4. Summary

The theory of the optimal estimation techniques [Rodgers, 2000] used in this study has been described along with a brief introduction to alternative retrieval methods, including the method used in the algorithm for operational AIRS CO retrievals. All these alternative methods offer the benefit of not requiring *a priori* covariance matrices, and in some cases an *a priori* profile is also not necessary. In some situations the construction of a suitable *a priori* covariance matrix may be very difficult, giving non optimal methods the advantage. However, when prior knowledge is available it would seem advantageous not to discard such information.

The key advantage of optimal estimation over these other techniques is the robust error information intrinsic to the retrieval. As was illustrated in §2.2.5, not only does it provide an estimate of the total error in the retrieved profile, but this error can be attributed to different contributors/components. If retrievals of atmospheric properties are to be used in quantitative analysis or incorporated into meteorological or chemical models, robust error estimates of this sort are essential.

Chapter 3. Development of the AIRS CO Retrieval

3.1. Introduction

In this chapter, the simulation work carried out to develop a new AIRS CO retrieval scheme is described. From here on, this retrieval scheme developed at the University of Edinburgh (and its components) will be referred to as the “UoE” retrieval. A full radiative transfer model is used to determine the AIRS channels sensitive to CO and illustrate the varying sensitivity with altitude. The work done in the development of the prior covariance is also detailed. Finally, a line-by-line (LBL) radiative transfer model is used to simulate AIRS CO retrievals and demonstrate the potential of the new retrieval scheme.

3.2. AIRS Sensitivity to CO

Of the 2378 high spectral resolution channels of the AIRS instrument, only those at the edge of the 3.74 to 4.61 μm band, close to the 1.0 vibration-rotation fundamental centred at 4.67 μm [Goody and Yung, 1995], would be expected to have any significant sensitivity to CO. In order to ascertain which channels may be useful for use in a CO retrieval scheme, some simulation work was carried out. This was done using the LBL radiative transfer model, Reference Forward Model (RFM) version 4.25 [Dudhia, 2005]. RFM was developed at Oxford University and is based on GENLN2 [Edwards *et al.*, 1992]. It operates in conjunction with the HITRAN 2000 database [Rothman *et al.*, 2003], enabling high resolution radiance simulations, taking account of the effect of a large number of absorbing molecules. RFM outputs radiances at fixed wavenumber intervals. AIRS channel radiances were simulated by convolving the RFM output with the spectral response functions for the AIRS channels [Hannon *et al.*, 2006].

Using the Air Force Geophysics Laboratory (AFGL) US standard profiles [Anderson *et al.*, 1986] as input to RFM, the sensitivity of the AIRS band-3 channel radiances to CO was investigated. Simulating the AIRS channel radiances for different scalings of the US standard CO profile revealed that only 113 of the band-3 channels were affected by CO. Of these, only the 53 channels closest to the CO fundamental at

4.67 μm were found to be significantly affected, with observed radiance changes larger than the instrument noise level, for a 10 times scaling in the US standard CO profile (Figure 3.6b). Here the instrument noise level is defined as the radiance corresponding to the Noise Equivalent Differential Temperature (NEDT) at 250 K, obtained from the AIRS channel properties file. Figure 3.1 shows the effect of CO concentration on the AIRS channel radiances, for those channels sensitive to CO. Similar analysis using alternative AFGL profiles (not shown) revealed differences in the sensitivity of the AIRS channels to CO, compared to those from the analysis using the US standard profile. As the sensitivity to CO is dependent upon the atmospheric conditions, it was deemed appropriate to retain the potentially optimistic estimate of the CO sensitive channels (from the US standard profiles), in the interest of not discarding potentially useful information

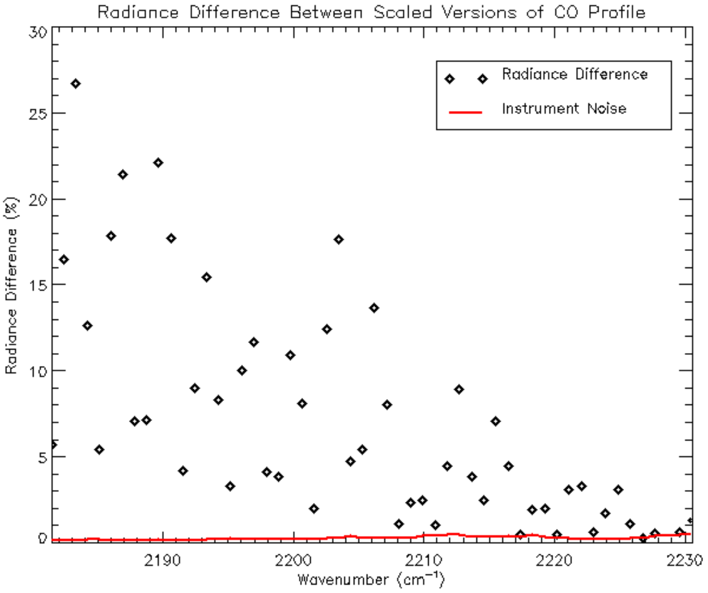

Figure 3.1 Percentage radiance difference between simulations of a scaled version (10x) of, and the unadjusted US standard CO profile. Only channels where the radiance difference is above instrument noise levels are shown.

3.3. Weighting functions

The sensitivity to CO of the set of 53 AIRS channels selected in §3.2 was further investigated, using RFM to generate the weighting functions for each channel with respect to CO, $\mathbf{K}_{\mathbf{CO}}$. RFM calculates $\mathbf{K}_{\mathbf{CO}}$ for a 1% CO perturbation, applied as a triangular function with altitude (i.e. a 1% perturbation is applied at a given altitude, with 0.67% and 0.33% perturbations applied to adjacent levels). These weighting functions are shown in Figure 3.2. Unlike the synthetic weighting functions from the example of Rodgers [2000] (Figure 2.1), where the weighting functions are consistent in magnitude and peak at a different altitudes, the peaks of $\mathbf{K}_{\mathbf{CO}}$ vary considerably in magnitude and occur over a small range of altitudes. This suggests that all of the 53 AIRS channels are most sensitive to CO in the mid-troposphere, between about 400 and 600 hPa, with some channels being considerably more sensitive than others, as can also be seen in Figure 3.1. The high degree of overlap between the weighting functions suggests that the AIRS radiances do not contain any more than one piece of independent information about CO. Some subtle distinctions in shape are present in the weighting functions, which may give rise to an increase in the number of pieces of independent information about CO, when instrument noise is considered. This possibility is addressed in §3.5.

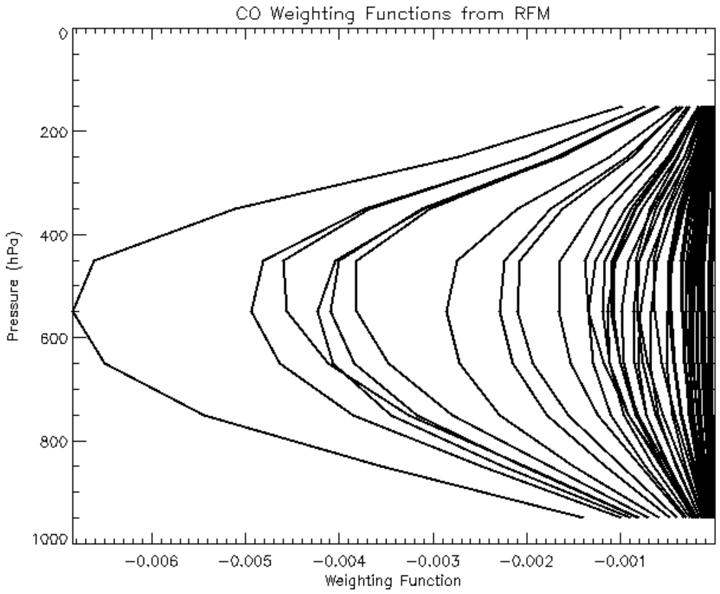

Figure 3.2 CO weighting functions for the 53 AIRS channels sensitive to CO, from RFM simulation of the US standard atmosphere.

Weighting functions for temperature, $\mathbf{K}_{\mathbf{T}}$ and water vapour, $\mathbf{K}_{\mathbf{H2O}}$ (with perturbations on each profile level of 1K and 1% respectively), were also generated for the set of 53 channels, Figure 3.3. These show that some of the channels that look to be most sensitive to CO also have a dependence on the temperature and water vapour in the lower troposphere. Although the temperature and water vapour profiles are not included as retrieval products, their influence on the channel radiances necessitates their inclusion as forward model parameters, **b**. It is also necessary to incorporate error estimates for these parameters into the retrieval scheme in some robust way.

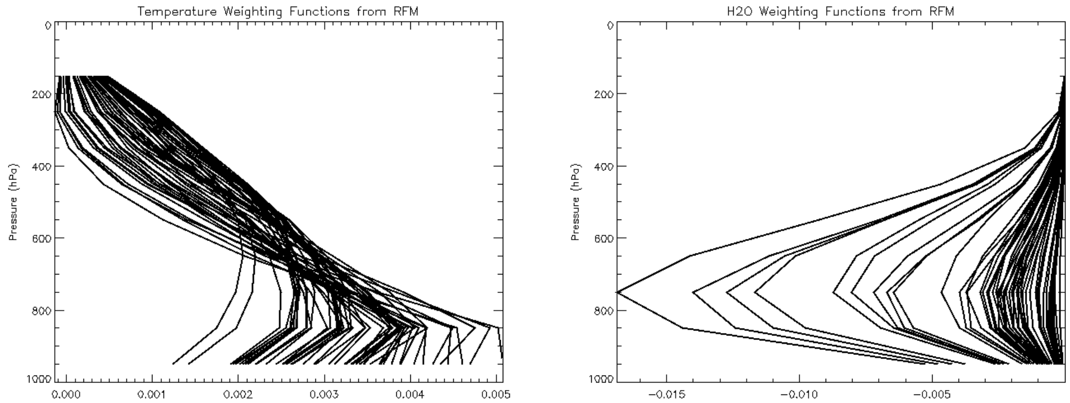

(a) (b)

Figure 3.3 Weighting functions for (a) temperature ($\mathbf{K_T}$) and (b) water vapour ($\mathbf{K_{H2O}}$) for the 53 AIRS channels sensitive to CO. $\mathbf{K_T}$ and $\mathbf{K_{H2O}}$ were calculated from RFM simulations of the US standard atmosphere.

3.4. Prior Information

As outlined in §2.2.2 key components of the MAP retrieval method are an initial estimate of the state, $\mathbf{x_a}$, and its covariance matrix, $\mathbf{S_a}$. Also of importance is the observational error covariance matrix, $\mathbf{S_\varepsilon}$. The development and selection of each of these for MAP retrievals of CO using the AIRS instrument is discussed in the following sections.

3.4.1. The Observational Error Covariance Matrix, $\mathbf{S_\varepsilon}$

In the absence of any information about the correlations between AIRS channels, $\mathbf{S_\varepsilon}$ was initialised as a square matrix of dimension, $m = 53$, with diagonal elements equal to the variance associated with the instrument noise (defined as in §3.2). This simple representation of $\mathbf{S_\varepsilon}$ was used for preliminary work, looking at a simplified linear retrieval with (model parameter) noise free simulations. Simulation work was also carried out with forward model parameter errors included (in $\mathbf{S_\varepsilon}$ using Eq. 2.3) and with the inclusion of cloud cleared radiance estimates in $\mathbf{S_\varepsilon}$.

3.4.2. The *a priori* Profile, $\mathbf{x_a}$

The AFGL US standard CO profile (shown in Figure 3.6) was selected for $\mathbf{x_a}$, for consistency with the “first guess” CO profile used in the AIRS v4 retrieval scheme, [McMillan *et al.*, 2005]. This CO profile is more representative of northern hemisphere regions near CO sources than it is of clean southern hemisphere regions far from CO sources. Using this profile as a global prior may introduce a positive bias in retrievals over areas with low CO concentrations. However, as discussed in Chapter 2**,** the MAP retrieval scheme provides an estimate of the contribution from the prior, thus providing some insight into any such bias.

3.4.3. The Prior Covariance Matrix

Selecting a suitable covariance matrix, $\mathbf{S_a}$, is not a trivial task. A simple diagonal matrix, with diagonal elements equal to the variance for an estimated uncertainty of 50% at each level in the profile, was taken as the starting point in developing a suitable $\mathbf{S_a}$. This enabled a preliminary assessment of a simple linear MAP retrieval, using simulated AIRS data.

Using a simple diagonal covariance matrix does not make full use of the prior information that may be available. It is reasonable to assume that there is some degree of correlation between CO at different altitudes and if such information is available it can be incorporated into $\mathbf{S_a}$. One potential source of data for generating $\mathbf{S_a}$ is *in situ* data from radiosondes or aircraft measurements. Due to the relatively sparse global coverage and lack of coherency between different measurement campaigns, constructing $\mathbf{S_a}$ from such data was not pursued in depth. The aircraft data set that was considered as a source for $\mathbf{S_a}$, was earmarked for use in a validation study of the UoE retrieval scheme, thus making it unsuitable as the source data for $\mathbf{S_a}$. Instead, output from a chemical transport model was investigated as a potential source of data.

Output from the 3-D Lagrangian chemical transport model, STOCHEM [Collins *et al.*, 1997], was used to generate $\mathbf{S_a}$. Twelve months of monthly mean CO profiles on nine evenly spaced pressure levels (950 to 150 hPa) and a 5°x5° longitude/latitude grid were used. Some basic statistics of the STOCHEM data are shown in Figure 3.4 (a) and the resultant prior covariance matrix in Figure 3.4 (b). The STOCHEM data has a mean profile considerably lower than the AFGL US standard profile used as the *a priori*. As mentioned in §3.4.2 the US standard profile is more representative of northern hemisphere regions, so is probably higher than the true global mean. Shindell *et al.* [2006] illustrated that CTMs typically estimate lower CO concentrations than observations, which could be another factor contributing to the large difference between the mean STOCHEM profile and the US standard profile.

The prior covariance matrix from the STOCHEM data shows the highest variances and covariances at the lowest levels in the atmosphere. This is a sensible result as the highest variability would be expected closest to the main CO source (the surface). $\mathbf{S_a}$ from the STOCHEM data also contains relatively high covariances between levels near the surface and levels near the top of the atmosphere, higher than those between more closely spaced levels in the upper-troposphere. To investigate whether these high covariances between lower and upper-troposphere levels were a result of using monthly mean CO profiles, Sa was calculated using a small sample of CTM data on regular and closely spaced time steps. This data was obtained from the REanalysis of the TROpospheric chemical composition over the past 40 years (RETRO) project. The data consisted of output from the MOZECH (ECHAM5-MOZ) CTM [Auvray *et al.,* 2007]; CO profiles on 31 pressure levels, on a 3-hourly time step over a 7 day period. Profiles were interpolated onto the STOCHEM pressure levels before the basic statistics of the data set and the covariance matrix were generated as for the STOCHEM data (Figure 3.5). Data from MOZECH covers a larger range of values than the STOCHEM data but has similar mean and standard deviation in the lower to mid-troposphere. At higher altitudes the mean MOZECH values are considerably higher than those from STOCHEM and US standard CO profile. The covariance matrices are broadly similar in terms of values and structures, with both exhibiting the highest variances and covariances at the near surface levels. There is some reduction in the covariances between lower and upper troposphere levels and also a reduction in covariances between middle and upper troposphere levels, in the

MOZECH $\mathbf{S_a}$. As the covariance matrices generated from the output of the two models were similar, the effect of averaging the CO profiles in the STOCHEM case was not deemed to be important in the construction of $\mathbf{S_a}$.

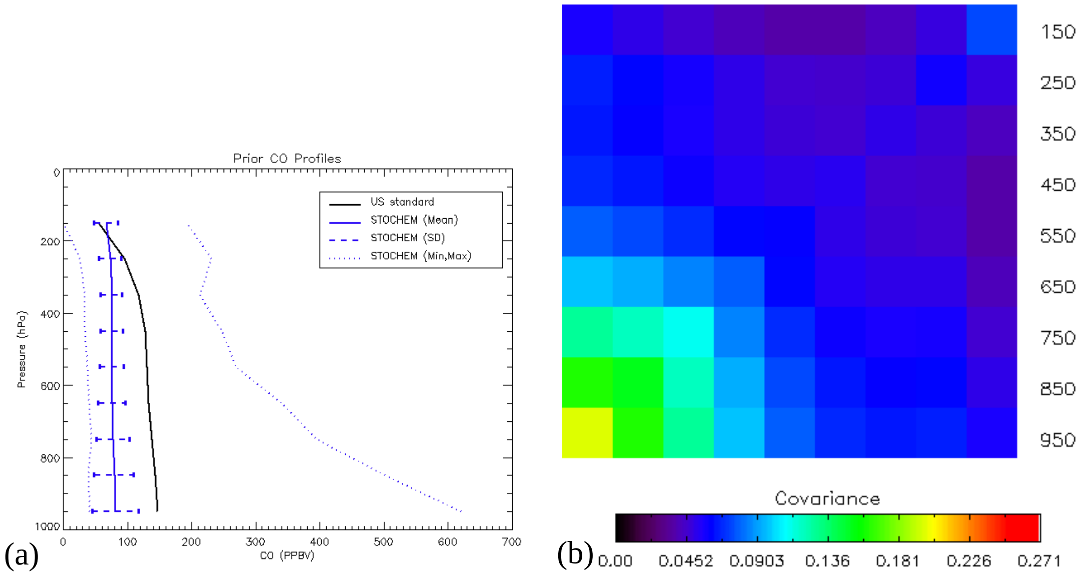

Figure 3.4 (a) Global mean, minimum, and maximum CO profiles from 12 months of STOCHEM data on 5°x5° longitude/latitude grid. (b) Covariance matrix, $\mathbf{S_a}$, calculated from the STOCHEM data described in (a). X-axis represents profile levels from 950 hPa to 150 hPa (left to right).

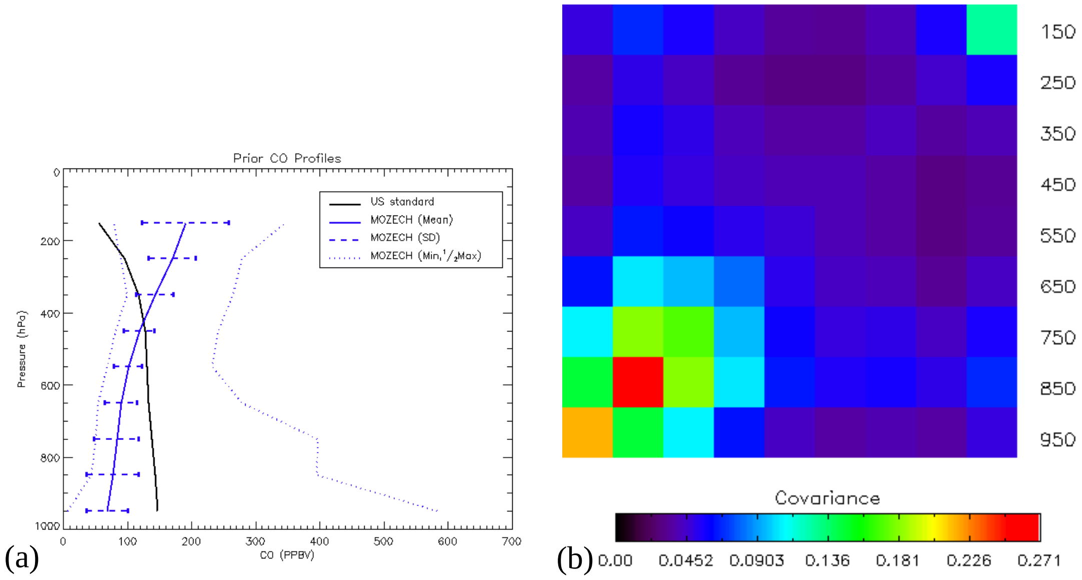

Figure 3.5 (a) Global mean, minimum, and maximum CO profiles from 7 days of MOZECH data on 5°x5° longitude/latitude grid. (b) Covariance matrix, $\mathbf{S_a}$, calculated from the MOZECH data described in (a). X-axis represents profile levels from 950 hPa to 150 hPa (left to right).

Although $\mathbf{S_a}$ from the two models were similar, there were still concerns about the high covariance values between lower and upper troposphere levels. Consequently an alternative covariance matrix was constructed using $\mathbf{S_a}$ from STOCHEM as a starting point, with covariances at these levels adjusted to lower values, decreasing with increasing separation between levels. The magnitudes of these manually adjusted values are based on the equivalent values from a covariance matrix calculated from a set of aircraft profiles, described in §4.2. As this set of aircraft profiles was assembled for use in a validation study of the retrieval scheme, it was inappropriate to use $\mathbf{S_a}$ from the aircraft profiles in the retrieval scheme. The resulting $\mathbf{S_a}$ (generated from STOCHEM data with a manual adjustment based on $\mathbf{S_a}$ from aircraft profiles) is shown in Figure 3.6 and is the alternative to the diagonal assumption in §3.5.

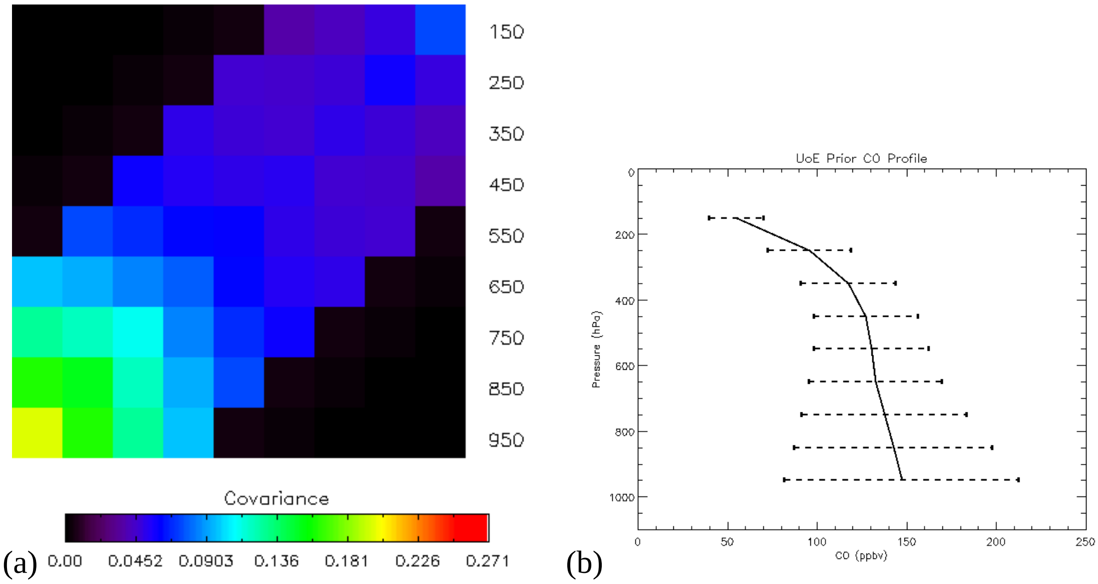

Figure 3.6 Prior information used in UoE retrievals. (a) $\mathbf{S_a}$ from STOCHEM data with a manual gradient applied to some off-diagonal elements. (b) $\mathbf{x_a}$ from AFGL US standard atmosphere with associated errors from $\mathbf{S_a}$.

In order to use the prior information illustrated in Figure 3.6 in the retrieval scheme, the CO profiles ($\mathbf{x_a}$, $\mathbf{x_i}$, and $\hat{\mathbf{x}}$) are all defined relative to the mean STOCHEM profile (i.e., $\mathbf{x_a} = \mathbf{x_{US\ Std}} / \mathbf{x_{STOCHEM}}$). This effectively applies the STOCHEM distribution around a new mean (US standard profile), which may bias the distribution of the retrievals. Maximum retrieved CO values are not expected to be adversely affected by this, but it is possible that retrievals of low CO values may be positively biased. As the observation of CO sources is a key motivation for developing the retrieval scheme, the risk of biases in low CO values was deemed acceptable. Results in Chapter 5 and Chapter 6 suggest that any such biases in low CO values are small.

3.5. Simulated Retrievals

Using the covariance matrices and *a priori* information described in §3.4 the MAP retrieval scheme was tested using RFM-simulated AIRS data. Results using the diagonal $\mathbf{S_a}$ and $\mathbf{S_a}$ from STOCHEM data with the manual gradient applied (Figure 3.6), are shown in the following sections.

3.5.1. CO Retrieval

The performance of the retrieval scheme in terms of the accuracy of the retrieval was investigated by attempting retrievals of the US standard CO profile scaled by a factor of 1.2, and using the AFGL tropical profiles as the atmospheric state. Figure 3.7 shows the retrieved profiles from the iterative retrieval scheme of Eq. 2.23 for the two versions of $\mathbf{S_a}$, for “noise free” simulations. These “noise free” simulations do not include errors from model parameters (such as the temperature profile) or errors in the channel radiances. They do however contain the baseline estimate of instrument noise, as defined in §3.2. This is necessary to ensure stability of the retrieval scheme. Figure 3.7 illustrates the effect on $\hat{\mathbf{x}}$ of the prior information about inter-level CO correlations, held in $\mathbf{S_a}$. Assuming no inter-level correlation, $\hat{\mathbf{x}}$ tends strongly to $\mathbf{x_a}$ at low and high altitudes. In this example the introduction of the off-diagonal covariances improves the accuracy of $\hat{\mathbf{x}}$ considerably at these levels.

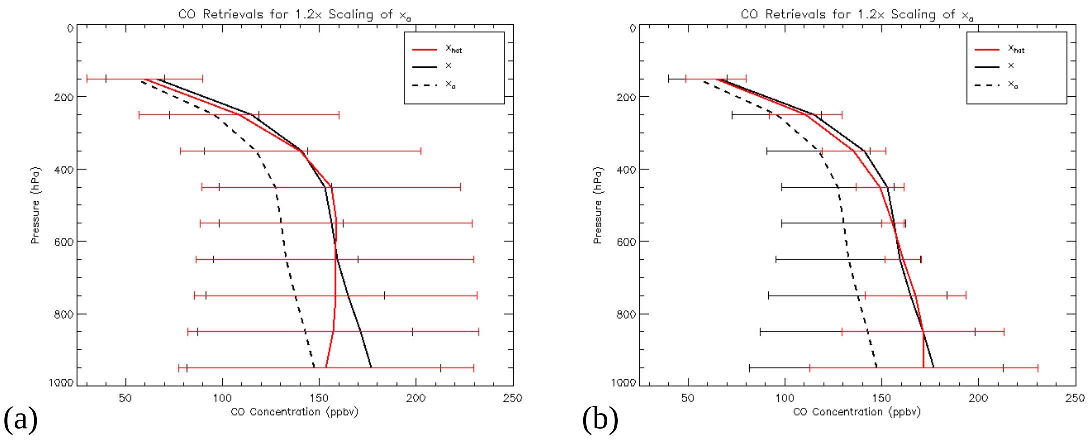

Figure 3.7 Noise-free simulated retrievals of the US standard CO profile scaled by a factor of 1.2. (a) Diagonal $\mathbf{S_a}$. (b) $\mathbf{S_a}$ from STOCHEM with adjustment of off-diagonal elements. Horizontal error bars represent prior (black) and retrieval (red) error estimates.

In addition to the “noise free” simulations, retrievals were also carried out with full error characterisation. Estimates of the various errors incorporated in the retrieval scheme were derived from the AIRS level-2 data products. Mean values of the errors were calculated over one day (24/10/06) for the tropics region (latitude bounds of ±30°). The resulting error estimates used in this simulation work are given in Table 3.1.

Parameter	**Temperature**	**H_2O**	**Surface T**	**Emissivity**	**Radiance**
Error	0.62 K	14.4 %	1.17 K	0.05	1.31 %

Table 3.1 Daily mean error estimates of AIRS L2 products used in the retrieval scheme, for the latitude region ±30°. Errors for temperature and H_2O represent the mean errors on STOCHEM profile levels. These error estimates are used throughout the simulation work of Chapter 3.

Including noise in the retrieval scheme significantly degrades the performance of the retrieval. This is illustrated in Figure 3.8b, where $\hat{\mathbf{x}}$ now lies approximately midway between the prior estimate, $\mathbf{x_a}$, and the true profile $\mathbf{x}$, at all levels (for the case using the UoE version of $\mathbf{S_a}$). Although the accuracy of the retrieval is reduced, the need to include information about inter-level correlations in $\mathbf{S_a}$ is again highlighted by the fact $\hat{\mathbf{x}}$ obtained using the diagonal $\mathbf{S_a}$ tends strongly to $\mathbf{x_a}$ at the top and bottom of the profile Figure 3.8b.

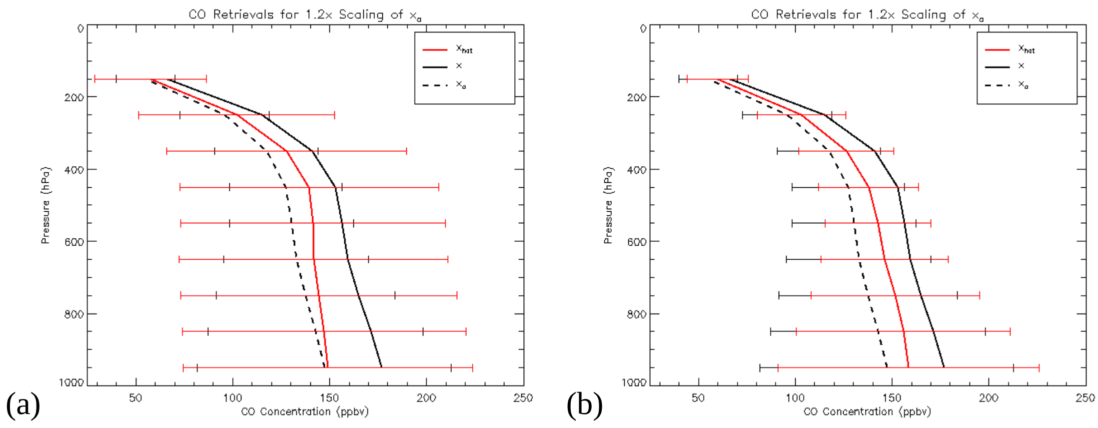

Figure 3.8 Simulated retrievals with noise added for the US standard CO profile scaled by a factor of 1.2. (a) Diagonal $\mathbf{S}_a$. (b) $\mathbf{S}_a$ from STOCHEM with adjustment of off-diagonal elements. Horizontal error bars represent prior (black) and retrieval (red) error estimates.

The results from the simulated retrievals with noise (Figure 3.8) highlight some potential issues with the UoE retrieval scheme. The most obvious of these is the sensitivity of the UoE retrieval to noise. A possible reason for what appears to be a high sensitivity to noise is potential double counting of errors within the retrieval scheme. In this example, estimates of both the errors in channel radiances and the errors in model parameters (defining the atmospheric state) are included. Although the cloud cleared radiance errors do not have the errors in the AIRS L2 products used to define the atmospheric state incorporated into them directly, they do however contain a contribution from errors associated with the atmospheric state. In the determination of the cloud cleared radiances, AMSU observations are used to define the atmospheric state for clear sky simulations, and errors in these observations are propagated through the cloud clearing method and contribute to the final radiance error estimates (§3.6.1). Consequently, including the cloud cleared radiance errors and the model parameter errors in the UoE retrieval is likely to provide an overall overestimate of the errors in the retrieval scheme, by effectively including two contributions from errors in defining the atmospheric state. It may be possible to reduce the effect of this double counting of errors if a full error covariance matrix were available for the AIRS cloud cleared radiances, rather than the diagonal matrix of variances available for this study. If the cloud cleared radiance errors do have significant contributions from errors in the atmospheric state, then the off-diagonal elements are likely to share some of the structure of $\mathbf{S}_\varepsilon$ calculated from the model parameter errors (Eq. 2.3). Increasing the information content about the measurement errors in this way is likely to damp the contribution from $\mathbf{S_a}$, and increase the information content of the retrieval.

In an effort to demonstrate the possible impact of this potential double counting of errors, further simulations were carried out including only the cloud cleared radiances estimates in the retrieval (no model parameter errors were included). The results from these simulations are shown in Figure 3.9. Here the UoE scheme Figure 3.9b provides a significantly more accurate retrieval than for the case where model parameter errors are also included (Figure 3.8b). Although the retrieval is considerably improved by the exclusion of the model parameter errors, it was deemed important to include them, due the uncertainty in the degree to which such errors are incorporated in the cloud cleared radiance error estimates.

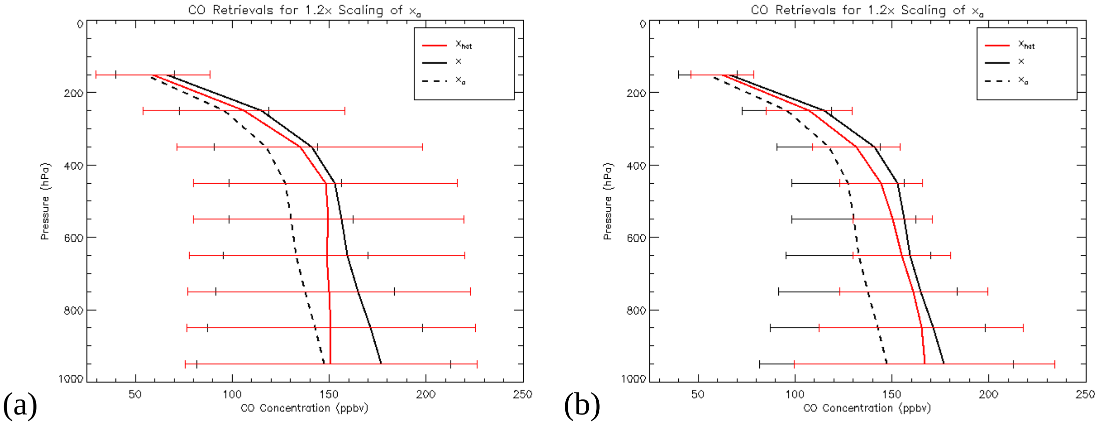

Figure 3.9 Simulated retrievals with only channel radiance noise estimates added (no model parameter noise included) for the US standard CO profile scaled by a factor of 1.2. (a) Diagonal $\mathbf{S_a}$. (b) $\mathbf{S_a}$ from STOCHEM with adjustment of off-diagonal elements. Horizontal error bars represent prior (black) and retrieval (red) error estimates.

3.5.2. Retrieval Error

Incorporating some inter-level correlations of CO into the retrieval scheme also significantly improves the retrieval error, as shown in Figure 3.10. Without the inter-level correlations, there is negligible difference between the prior and posterior error estimates at the extremes of the profile, and only a relatively small improvement in the error estimate at mid-troposphere levels. When $\mathbf{S_a}$ includes information about inter-level correlations there is a much greater improvement in the error estimate at mid-troposphere levels, along with significant improvements in the lower and upper levels.

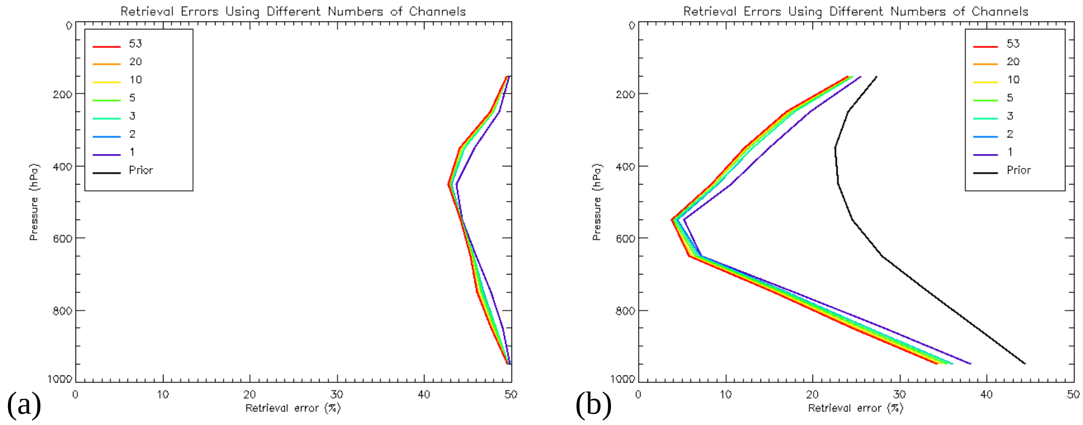

Figure 3.10 Retrieval errors for noise free simulated retrievals of the US standard CO profile scaled by a factor of 1.2. (a) Diagonal $\mathbf{S_a}$. (b) $\mathbf{S_a}$ from STOCHEM with manual adjustment (§3.4.3). Each colour represents a retrieval using the number of channels indicated in the legend.

The retrieval errors for simulations with noise included are shown in Figure 3.11 for retrievals using the UoE $\mathbf{S_a}$ only. These show the retrieval errors for the case of full error characterisation and the case where only the channel radiance errors are included (Figure 3.11 (a) and (b) respectively). It is clear that including noise in the retrieval significantly increases the error in the retrieval (relative to the noise-free case, Figure 3.10b). However there is still considerable reduction in the error (~5% at 550 hPa) relative to the prior.

Figure 3.11 also shows the effect the number of channels used in the retrieval has on the retrieval error. Retrieval errors are plotted for retrievals with increasing numbers of channels used in the retrieval, with channels added in order of highest to lowest contribution to the number of degrees of freedom of the signal. For the case where only the channel radiance errors are included, there is very little change in the retrieval error between the 10 and 53 channel cases. Although this suggests a large number of superfluous channels are used, when the model parameter errors are also included a larger number of channels are required to provide retrieval errors close to those of the 53 channel case. This is because the sensitivity of each channel to CO varies for different atmospheric conditions (as mentioned in §3.2). Having redundant channels can help average out noise and ensures that the best channels for different conditions are always present. Consequently all 53 CO sensitive channels are retained in the retrieval scheme.

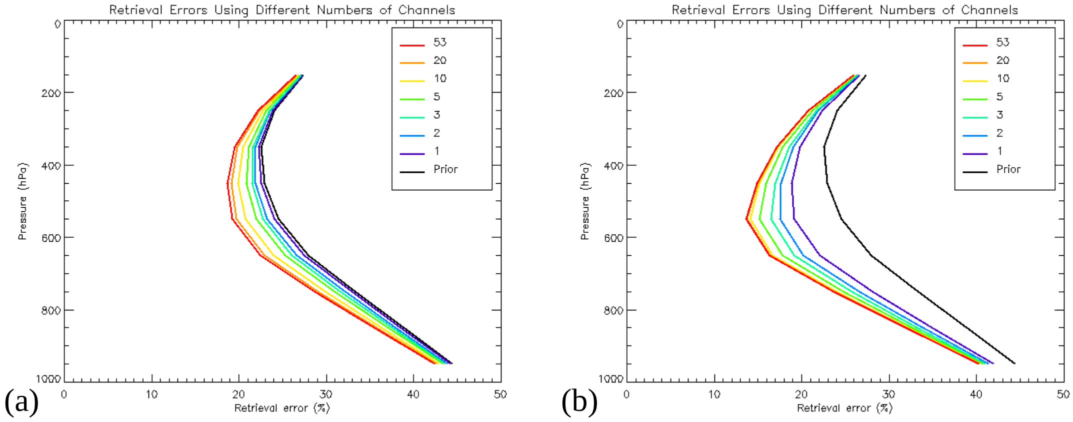

Figure 3.11 Retrieval errors for simulated retrievals of the US standard CO profile scaled by a factor of 1.2, with noise included. (a) Errors in channel radiances and model parameter errors included. (b) Only channel radiance errors included. For both (a) and (b) $\mathbf{S_a}$ from STOCHEM with manual adjustment has been used. Each colour represents a retrieval using the number of channels indicated in the legend.

Some additional error analysis was carried out to try to gain a better understanding of the relative contributions of the different error sources to the total retrieval error. Using Eqns. 2.18 to 2.21 the total retrieval error was split into its components (smoothing, measurement and model parameter error). These error components are shown in Figure 3.12, for the case of full error characterisation and the case where only the channel radiance errors are included (Figure 3.12 (a) and (b) respectively). In Figure 3.12a, the smoothing error provides the dominant contribution to the total retrieval error. Given the averaging kernels (Figure 3.14a) this is not a surprising result, as they indicate there is a very limited amount of information about the vertical structure of the CO profile contained within the AIRS observations. The consequence of this lack of vertical structure information is significant smoothing of the true CO profile, and therefore the introduction of significant errors in the retrieval.

Errors from measurement noise are the next largest contributor to the total retrieval error. This suggests that the retrieval is very sensitive to the errors in the cloud cleared radiances, so it is likely that the retrieval performance will be degraded in situations where the cloud clearing algorithm returns high error values (e.g. where there is large uncertainty in the atmospheric state or in regions where there is large variance in cloud cover across the AIRS scene).

Only a small contribution from the model parameter errors is observed Figure 3.12a. However the inclusion of these errors also affects the smoothing error contribution (see Eqns.2.9, 2.10, and 2.18). Comparison with the errors from the case with model parameter errors excluded (Figure 3.12b) reveals that it is this additional contribution to the smoothing error that is main reason for the increase in retrieval error between the two cases.

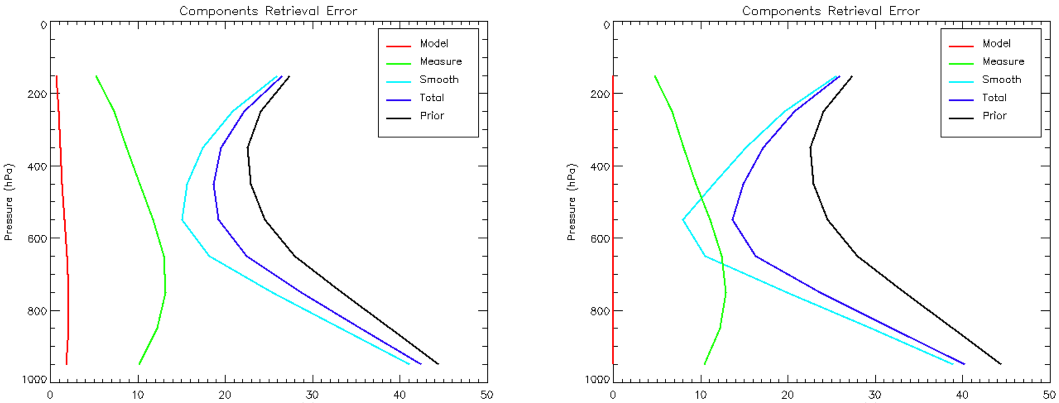

(a) (b)

Figure 3.12 Components of the retrieval error for simulated retrievals of the US standard CO profile scaled by a factor of 1.2, with noise included. (a) Errors in channel radiances and model parameter errors included. (b) Only channel radiance errors included.

In addition to looking at the contributions to the total retrieval derived from Eq. 2.21, retrievals were carried out with the input errors (Table 3.1) considered individually. The resulting total retrieval errors at 550 hPa for each of the input errors are given in Table 3.2. As the addition of model parameter errors to the retrieval (Eq. 2.3) introduces correlations between instrument channels to the observational error covariance matrix, $\mathbf{S}_\varepsilon$, these results only give a general idea of the relative contributions of the different sources of input error. Table 3.2 suggests that errors in the cloud cleared radiance estimates and the surface temperature will typically be the largest contributors to the total retrieval error. As the errors in both of these parameters are generally larger over land surfaces, the retrieval scheme is expected to perform better over ocean regions than over land (a result observed in Chapter 5).

Table 3.2 also illustrates the effect of including non-zero off-diagonal elements in the observational covariance matrix, $\mathbf{S}_\varepsilon$. Comparison of the retrieval error between the model parameter free case (NEDT) and the cases with model parameters included (e.g. NEDT + T) shows that the addition of some model parameter errors can reduce the retrieval error. This is a consequence of information about inter-channel correlations being introduced through non-zero off-diagonal elements in $\mathbf{S}_\varepsilon$ (through Eq. 2.3).

Input Error Source	**Retrieval Error (%)**
NEDT	5.8
AIRS	13.6
NEDT + T	3.8
NEDT + H_2O	4.0
NEDT + T_{surf}	11.0
NEDT + ε	3.4
NEDT + all	4.1
AIRS + all	19.2

Table 3.2 Retrieval errors for retrievals with input errors considered individually.

There are some other potential sources of error that have not been included in the retrieval scheme, as their impact on the retrievals was deemed insignificant relative to contributions from the error sources previously discussed. Aumann *et al.* [2006] demonstrate the absolute calibration accuracy at 2616 cm^{-1} to be < 0.2 K, with better than 16 mK/yr stability. This is small relative to typical errors in the cloud cleared radiances. Another possible source of error is the spectral response functions (SRFs), characterised by the spectral centroid, width, and shape. The accuracy requirements for this are discussed by Aumann and Strow [2001] and shown to be met. Errors in the SRFs (in terms of location of the centroids, width and shape) are small and their potential contribution to errors in CO retrievals considered negligible. Finally, errors in the forward model used to simulate the AIRS channel radiances may have a potential impact on the CO retrievals. Errors in the forward model arise through uncertainties in the spectroscopic data (the HITRAN database) and also through the parameterisations used to describe the physical and chemical state of the atmosphere. Again, estimates of the errors in the forward model were not incorporated in the retrieval scheme as they were thought to be small relative to the errors in the cloud cleared radiances, and because there was thought to be a degree of double counting of the model parameter errors in the retrieval scheme (§3.5.1).

3.5.3. Averaging Kernels

In addition to the simulated retrievals using the AFGL tropical atmosphere as the atmospheric state, equivalent simulations were also carried out using the AFGL US standard atmosphere. The averaging kernels, **A**, calculated for the AFGL US standard and Tropical atmospheres are shown in Figure 3.13. These are from noise-free retrievals using the UoE $\mathbf{S_a}$. For the case of the US standard atmosphere, all of the averaging kernels share a similar shape and peak at mid-troposphere levels. This informs us that the AIRS instrument is predominantly sensitive to CO in the mid-troposphere and that each level of the retrieved CO profile will contain a significant contribution from CO in the mid-troposphere. The broad shape of the averaging kernels indicates that the vertical resolution of $\hat{\mathbf{x}}$ will be poor, with profile features smaller than about 6 km smoothed out. As outlined in §2.2.4 an estimate of the number of degrees of freedom of the signal, d_s, can be obtained through visual inspection of the averaging kernels. If there is minimal overlap between the averaging kernels, then each distinct peak represents one degree of freedom. Comparison of the averaging kernels for the two different atmospheres reveals that the AIRS observations for the tropical atmosphere contain more independent pieces of information than those for the US standard atmosphere. From Figure 3.13 d_s for the US standard atmosphere would be estimated to be about 1.0, while d_s for the tropical atmosphere lies between 1.0 and 2.0, as there is more distinction between the averaging kernels at different levels. This is the expected result due to the higher thermal contrast between surface and atmosphere, and between altitude levels, for the tropical atmosphere. From this we may expect the retrieval scheme to perform better in the tropics than at mid-latitudes, and for retrievals of more limited quality to be obtained in high latitude regions.

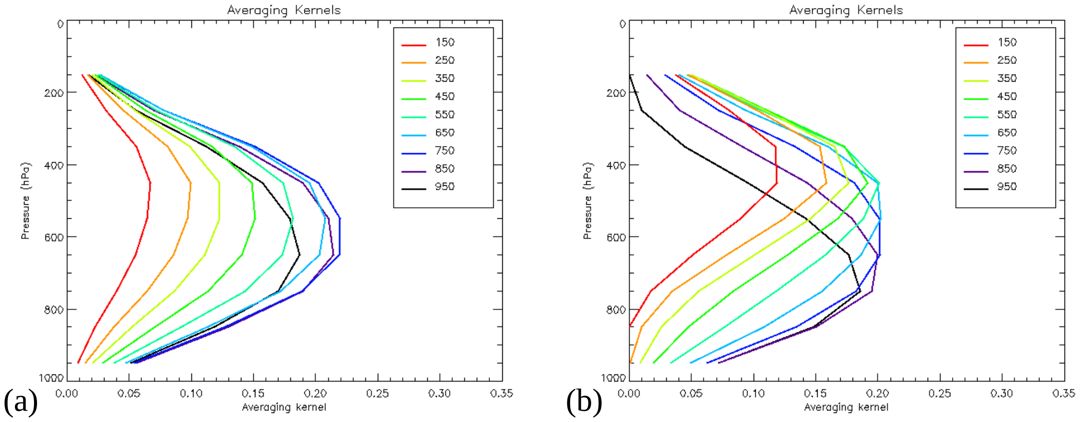

Figure 3.13 Averaging kernels calculated from noise free simulations of the AFGL atmospheres using the UoE $\mathbf{S_a}$. (a) US standard atmosphere. (b) Tropical atmosphere.

Averaging kernels are also shown for simulations with noise included in the retrieval, for the tropical atmosphere only (Figure 3.14). The addition of noise to the retrieval scheme has a significant effect on the averaging kernels calculated for the tropical atmosphere. This is illustrated in Figure 3.14, where the averaging kernels for simulations with noise included in the retrieval are shown for the tropical atmosphere. Distinctions between the averaging kernels of different levels that were present in the noise free case (Figure 3.13b) are not present when noise is included in the retrieval, with the averaging kernels for the tropical atmosphere now showing more resemblance to those calculated for the noise free US standard atmosphere. Figure 3.14 suggests that even in the tropics the AIRS observations will provide no more than one piece of independent information about the CO profile. However, in cases where there are low levels of uncertainty in the cloud cleared radiances and model parameters, some of the potential information about vertical structure, illustrated in Figure 3.13, may be present.

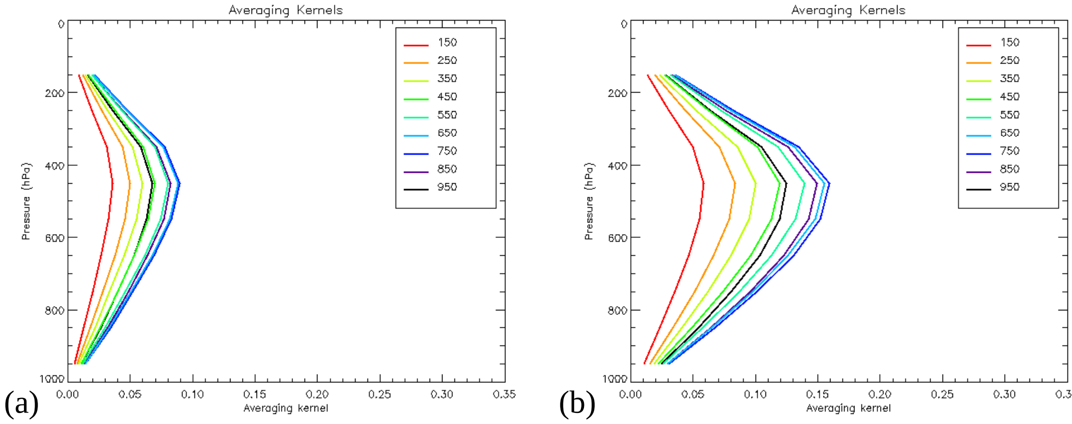

Figure 3.14 Averaging kernels calculated from simulations of the AFGL tropical atmosphere with noise included in the retrieval, and using the UoE $\mathbf{S_a}$. (a) Errors in channel radiances and model parameter errors included. (b) Only channel radiance errors included.

3.5.4. Degrees of Freedom of Signal, d_s

Following on from the estimations of d_s from visual analysis of the averaging kernels (Figure 3.13), d_s was calculated using Eq. 2.15. This was carried out for the AFGL US standard and tropical atmospheres, using the UoE $\mathbf{S_a}$. The effect on d_s of the number of channels used in the retrieval scheme was investigated, with channels added in order of the size of their contribution to d_s. This was done for simulations using channel noise estimates from the AIRS channel properties file (§3.2) and using the daily mean values from AIRS L2 data (Figure 3.15 and Figure 3.16 respectively). As we would expect, d_s decreases when model parameter error is included and also when the daily mean channel radiance error is used. As estimated in §3.5.3, d_s is larger for the Tropical atmosphere than the US standard atmosphere, with $d_s \approx 1.0$ and 1.15 respectively for the noise free case, when the maximum number of channels are used ($d_s \approx 0.3$ and 0.4 when daily mean radiance errors are included). Figure 3.15 and Figure 3.16 also show that only a small number of channels are required to produce d_s close to the maximum value (obtained when all channels are used). However, the ordering of the channels in terms of their contribution to d_s is not the same for the two different atmospheres. Figure 3.15 and Figure 3.16 also show that the channel ordering is not the same between the cases with and without model parameter error included, illustrated by the fact that more channels are required to give d_s close to the maximum, when the channel ordering for the “no $\mathbf{S_b}$” case is applied to retrievals with model parameter errors included. This behaviour is a consequence of the contribution of individual channels being dependent on the atmospheric state and the errors in the retrieval scheme. As there may be considerable variations in both the atmospheric state and the errors incorporated into the retrieval scheme, this result supports the decision to retain all 53 potentially sensitive channels in the retrieval scheme.

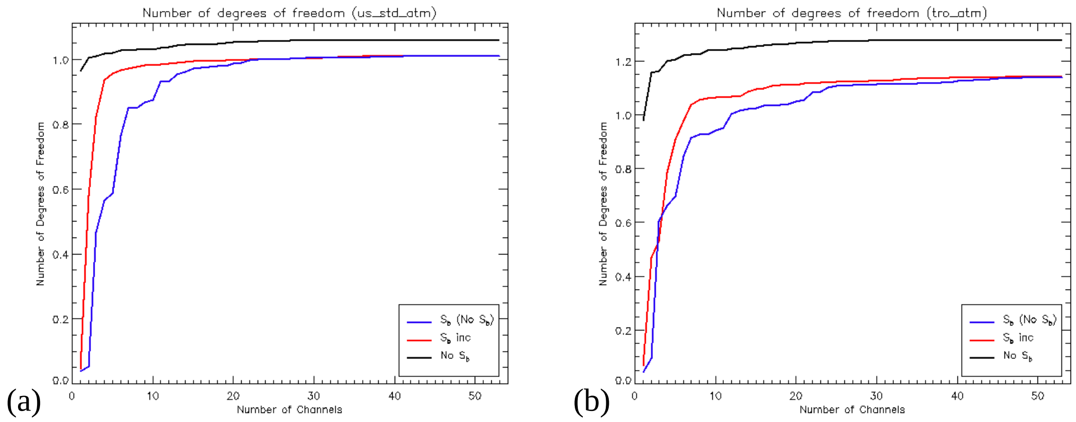

Figure 3.15 Number of degrees of freedom of signal, d_s, with increasing number of channels used in retrieval (added in order of largest contribution to d_s) for US standard (a) and tropical (b) AFGL atmospheres. Each line represents d_s calculated from retrievals using different channel ordering as follows: no model parameter errors included (No $\mathbf{S_b}$), model parameter errors included ($\mathbf{S_b}$ inc), and retrievals for the case with model parameters included but using the channel ordering of the "No $\mathbf{S_b}$" case ($\mathbf{S_b}$ (no $\mathbf{S_b}$)). These plots are for simulations with the channel radiance error taken from the AIRS channel properties file (§3.2) rather than the mean value from AIRS data.

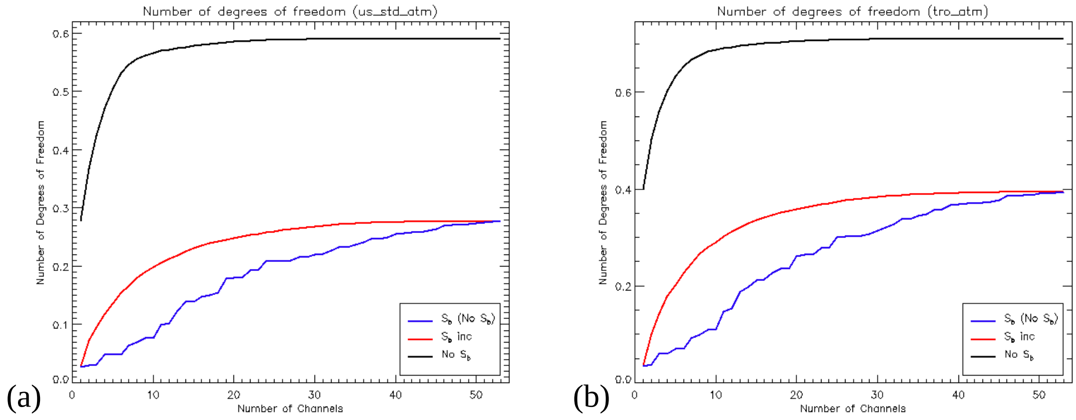

Figure 3.16 Number of degrees of freedom of signal, d_s, with increasing number of channels used in retrieval (added in order of largest contribution to d_s) for US standard (a) and tropical (b) AFGL atmospheres. Each line represents d_s calculated from retrievals using different channel ordering as follows: no model parameter errors included (No $\mathbf{S_b}$), model parameter errors included ($\mathbf{S_b}$ inc), and retrievals for the case with model parameters included but using the channel ordering of the "No $\mathbf{S_b}$" case ($\mathbf{S_b}$ (no $\mathbf{S_b}$)). These plots are for simulations with the channel radiance error taken to be the daily mean value from AIRS data.

3.6. Application to AIRS data

3.6.1. Inputs to the Retrieval Scheme

The retrieval scheme outlined in Chapter 2 and earlier sections of this chapter was applied to radiances from the AIRS instrument. Table 3.3 lists the AIRS level-2 (L2) data products that are used, and where they are incorporated into the retrieval scheme.

AIRS L2 Product Variables	Corresponding Symbol
Cloud cleared radiances	$\mathbf{y}$
Error in cloud cleared radiances	$\mathbf{S_\varepsilon}$
Temperature profile	$\mathbf{x_b}$
H_2O profile	$\mathbf{x_b}$
Surface temperature	$\mathbf{x_b}$
Surface emissivity	$\mathbf{x_b}$
Errors in above profiles and surface values	$\mathbf{S_b}$

Table 3.3 AIRS level-2 data products used in the UoE retrieval scheme and where they are incorporated.

In all retrievals the AIRS L2 cloud cleared radiances, for the 53 CO sensitive channels, are used to represent the measurement vector, **y**. The AIRS cloud clearing method [Chahine, 1974] uses observations from a number of adjacent field of views (FOVs) to infer what the radiances in the clear portions of the scene would be. This method does not require accurate modelling of cloud properties, but instead relies on two key assumptions: only the relative amount of each cloud type varies across FOVs (the radiative properties are identical), and that the FOVs have the same characteristics in the clear portions of their scenes. Using these assumptions the cloud cleared radiances, $\hat{R}_i$, for each channel, *i*, are calculated from sets of 3x3 AIRS pixels using Eq. 3.1 [Susskind *et al.*, 2003]:

$$\hat{R}_i = R_{i,AVG} + \sum_{k=1}^{K} \eta_k \left(R_{i,AVG} - R_{i,k}\right), \tag{3.1}$$

where $R_{i,k}$ and $R_{i,AVG}$ are the radiances for the k_{th} pixel and the average radiance over the set of 9 pixels respectively. The parameter η_k is determined for each of the 9 FOVs, using observations from a set of I (=76) cloud filtering channels, lying primarily in between lines of the 15 µm and 4.2 µm CO_2 bands, with some additional channels in the window regions. Estimates of $\hat{R}_i$ from simulations are substituted into Eq. 3.1 and η_k determined using a weighted least squares solution.

The estimates of $\hat{R}_i$ are recalculated in a four stage iterative scheme, using the current best estimate of the surface and atmospheric properties that are consistent with observations from the AMSU-A instrument. New estimates of η_k are obtained from this iterative scheme, along with a noise covariance matrix, containing estimates of the errors in these cloud cleared radiances. These error estimates contain an estimate of the instrumental noise along with contributions from errors in the estimated values of parameters such as the surface skin temperature, surface emissivity, and profiles of temperature and water vapour.

The cloud cleared product is output on the spatial resolution of the AMSU footprints (i.e. 1 footprint per set of 3x3 AIRS pixels). Susskind *et al.* [2003] propose that the use of this cloud clearing method enables retrievals of various physical parameters to be made in the presence of substantial cloudiness, up to 80%. These cloud cleared radiances are accompanied by error estimates, which are incorporated into the retrieval scheme in the form of the variances along the diagonal of $\mathbf{S}_\varepsilon$. In some cases these error estimates are lower than the instrumental noise from the channel properties file. For such cases the noise estimates from the channel properties file were incorporated into $\mathbf{S}_\varepsilon$ in place of the estimates from the L2 product. This was done to maintain a conservative error estimate and to maintain stability in the retrieval scheme.

The profile and surface parameters listed in Table 3.3 are not included directly in the retrieval scheme itself but are used an input to the forward model. As described in §2.2.2 the error estimates for these forward model parameters are incorporated into the retrieval scheme through $\mathbf{S}_\varepsilon$ (Eq. 2.3).

3.6.2. The Forward Model

If retrievals are to be made from the satellite data in real time, then it is necessary to use a much faster forward model than that used (RFM) in the simulation work of §3.5. For application to AIRS data the line-by-line radiative transfer model, RFM, was replaced by the fast forward model RTTOV (Radiative Transfer for TOVS) [Matricardi *et al.*, 2001]. This model was developed by the EUMETSAT NWP satellite application facility. While RFM uses a LBL approach (where the absorption and emission of radiation by each molecular transition is considered in turn over the spectral range of interest), RTTOV operates using a fast model of the transmittances of the atmospheric gases. This fast model is derived from accurate LBL transmittances, calculated for a set of diverse atmospheric profiles. The monochromatic transmittances are convolved with the AIRS spectral response functions and, using a set of predictors, are used to calculate channel-specific regression coefficients. This set of regression coefficients allows RTTOV to compute transmittances for any input profile. It is this method of parameterization of the transmittances that gives rise to the increased computational efficiency over LBL models.

As discussed by Matricardi *et al.* [2001], RTTOV radiances exhibit a degree of accuracy such that errors from the fast transmittance algorithm do not add significantly to the errors that are likely to be present in the LBL model. An extensive inter-model comparison study is described by Saunders *et al.* [2007], with specific focus on simulating AIRS radiances. Saunders *et al.* [2007] demonstrate good agreement between RTTOV and RFM, both in terms of radiances and Jacobians, with the standard deviation of the differences between the models being less than the instrumental noise levels of AIRS.

The AIRS L2 products listed in Table 3.3 were used to run this model to estimate the AIRS radiances and the weighting functions ($\mathbf{F}(\mathbf{x}_i)$ and $\mathbf{K}_i$ respectively, in Eq. 2.23) at each iteration. As previously, the AFGL standard was used as the *a priori*, $\mathbf{x}_a$, and as the initial linearization point for the retrieval. At each iteration the most recent estimate of the CO profile, $\mathbf{x}_i$, was used as input to RTTOV, while all other model parameters were held constant, as they are not part of the retrieval product.

3.7. AIRS v4 Retrieval Algorithm

The UoE and AIRS v4 retrieval schemes operate by attempting to minimize the weighted difference between the observed radiances and those calculated using a forward model, by varying the geophysical state. While the UoE retrieval constrains the solution using prior knowledge of the state (in the form of $\mathbf{S_a}$) the aim of the AIRS science team is to use an algorithm that "relies exclusively on the signal to noise of the observations to indicate the degree to which the information contained in the radiances should be believed, and does not involve use of an estimate of the accuracy of the background field" [Susskind *et al.*, 2003]. To this end the AIRS v4 algorithm was developed using a form of the constrained exact solution (§2.3.2) with the solution constrained using singular value decomposition (SVD).

In the AIRS v4 algorithm, the tropospheric CO profile is represented by a set of four vertically overlapping trapezoidal functions, empirically derived from simulations [McMillan *et al.*, 2005]. As highlighted in §2.3.2, representation function solutions can be badly affected by even low levels of noise. Consequently the AIRS v4 algorithm includes a constraint matrix, **H**, in the notation of Susskind *et al.* [2003]. This is analogous to the prior covariance matrix, $\mathbf{S_a}$, in the UoE retrieval, but rather than using a fixed constraint matrix, the AIRS v4 algorithm calculates **H** at each iterative step in the retrieval. In the method of Susskind *et al.* [2003] **H** is calculated from the information content of ($\mathbf{K^T S_\varepsilon^{-1} K}$) by singular value decomposition (Eq. 3.2).

$$\boldsymbol{\Lambda} = \boldsymbol{U}^T\left[\boldsymbol{K}^T\boldsymbol{S_\varepsilon}^{-1}\boldsymbol{K}\right]\boldsymbol{U} \qquad \mathbf{3.2}$$

Where **U** is the eigenvector matrix of ($\mathbf{K^T S_\varepsilon^{-1} K}$), **K** is the Jacobian matrix, and $\mathbf{S_\varepsilon}$ is the noise covariance matrix. The resultant matrix, **Λ**, is a diagonal matrix with elements equal to the eigenvalues, λ. To constrain the solution, the least significant eigenvectors are damped proportional to their eigenvalue, giving the constraint matrix:

$$\boldsymbol{H} = \boldsymbol{U}\Delta\boldsymbol{\Lambda}\boldsymbol{U} \qquad \textbf{3.3}$$

Where $\mathbf{\Delta\Lambda}$ represents the damped eigenvectors.

The AIRS science team view this method of constraint to be more robust than using a static prior covariance matrix, $\mathbf{S_a}$ [Barnet, 2005], on the basis that a poorly estimated $\mathbf{S_a}$ has the potential to introduce biases to the retrieval, making it suboptimal. Although this is true, the use of a suitable static prior covariance matrix and optimal estimation techniques allows the retrieval scheme to take advantage of all the available information. As the MAP retrieval has inherent information about the contribution from the prior, it should be possible to detect and characterise any biases introduced by $\mathbf{S_a}$. Although the AIRS v4 algorithm does not use prior covariance matrix, it is still influenced by the “first guess” profile [Warner *et al.*, 2007].

In addition, the representation functions and SVD introduce their own potential to return suboptimal retrievals. As the representation functions are determined empirically from simulations, they indirectly introduce prior information to the retrieval, and as noted by Susskind *et al.* [2003] a “judicious choice” of these functions is required. The calculation of the constraint matrix, **H**, at each iteration using SVD requires a choice of parameters for applying the damping. Again a poor choice of these parameters has potential to make the retrieval suboptimal. Due to these required choices, the AIRS v4 retrieval scheme may be considered no less arbitrary than the UoE scheme (which requires choices of $\mathbf{x_a}$ and $\mathbf{S_a}$). As is shown in Chapter 4 and Chapter 5**,** the AIRS v4 algorithm is more biased relative to aircraft and MOPITT observations, and does not have the benefit of a well developed theory of errors.

Chapter 4. Validation Study

4.1. Introduction

Having demonstrated the potential of the UoE retrieval scheme through simulations (Chapter 3) the UoE method was further tested by means of a validation study. The purpose of this validation study was two-fold: to provide a simple demonstration of the operation of the retrieval scheme when applied to AIRS data, and to gain an understanding of the value of these retrievals. In order to do this a set of *in situ* profiles from aircraft was used as the “truth” data for validation. Aircraft data were chosen over other potential sources (e.g. data from ground based Fourier Transform Spectrometers) to avoid difficulties involved in comparing retrievals from two different remote sensing instruments [Rodgers and Connor, 2003]. The range of geographical locations and altitudes covered by aircraft measurement campaigns, and their relative ease of availability also support the use of such data in validation work. As such, *in situ* aircraft data have frequently been used in the validation of retrievals of different atmospheric parameters from satellite instruments (e.g. Emmons *et al.* [2004] and Gettelman *et al.* [2004]).

Although commonly used in the validation of satellite retrievals, aircraft data also has its limitations for such work. The key limitation when considering the comparison of *in situ* aircraft profiles with satellite data is the difference in geographical measurement scales. Aircraft profiles consist of point measurement, whereas satellite observations cover relatively large spatial scales (both horizontally and vertically). It is also the case that aircraft measurements may not be coincident in time with satellite overpasses. Even in targeted aircraft campaigns, where temporal coincidence is good, the time taken to record the aircraft profile will result in some discrepancy between aircraft measurement and satellite observation times. These differences in spatial and temporal sampling give rise to the potential for aircraft and satellite to observe very different atmospheric conditions (e.g. if the aircraft were to fly through a localised CO plume). As a result of these limitations, care must be taken when collating aircraft data for validation and when analysing the results.

4.2. Validation Data Set

4.2.1. In Situ Data

As discussed in §4.1, validation of the UoE retrieval scheme was carried out using a data set of *in situ* aircraft profiles, constructed specifically for this study. This data set consisted of over 132 profiles, collated from three independent measurement campaigns, covering a range of locations around Central and North America, and around the UK (Figure 4.1). As is usual with such an exercise, considerable effort was required to standardise the aircraft measurements between campaigns, and to apply consistent quality control across the data set, details of which are outlined in §4.2.5.

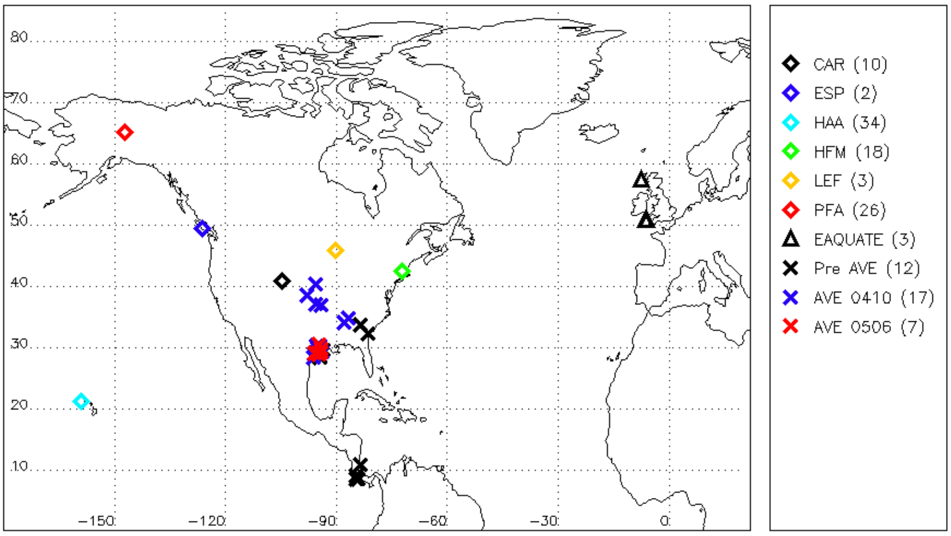

Figure 4.1 Locations of the *in situ* aircraft CO profiles used in the validation study. Numbers in parenthesis indicate the number of profiles from each aircraft campaign/station (detailed in §4.2.2 to §4.2.4). Aircraft data covers three measurement campaigns: NOAA CMDL (CAR, ESP, HAA, HFM, LEF, PFA), the Aura Validation Experiment (Pre AVE, AVE 0410, AVE 0506), and EAQUATE (EAQUATE).

4.2.2. NOAA CMDL

Over half of the *in situ* profiles were taken from six measurement stations in the NOAA CMDL (Climate Monitoring and Diagnostics Laboratory) data set [ERSL, 2007]. These cover a range of locations across North America (including Alaska) and over the Pacific Ocean, near Hawaii. The altitude range covered by the profiles varies over the range of ~0.5 km to ~13 km, with most profiles covering a range of

~1 km to ~8 km. Only data points which passed all CMDL quality checks were used. The number of CMDL profiles available for use in this validation study was limited by the relatively poor coincidence between the *in situ* measurements and the AIRS overpass times for many of the CMDL recording stations. NOAA CMDL use an automated flask sampling method that collects whole air samples at different altitudes during the flight. CO concentrations are then determined from these samples in the laboratory, using gas chromatography and HgO reduction techniques [Novelli *et al.*, 1998]. All measurements are referenced to the CMDL/WMO CO scale and have typical errors of ~3 ppb [Novelli *et al.*, 2003].

4.2.3. Aura Validation Experiment (AVE)

The other main source of *in situ* data was NASA's Aura Validation Experiment [Gaunce, 2007], with flight paths originating from Houston, Texas, and San Jose, Costa Rica. As the objective of this campaign was to provide validation data for instruments on NASA's Aura satellite, part of the A-train, the measurement times closely match those of the AIRS overpasses. Some instruments onboard the Aura satellite, such as the Microwave Limb Sounder (MLS), focus more on measurements in the stratosphere. As a result this data set contains more measurements at higher altitudes than the CMDL campaign, with profiles covering altitude ranges of ~0 km to ~20km. The AVE aircraft campaign measures CO using a tuneable diode laser absorption spectrometer (TDLAS), Argus, flown onboard WB-57F aircraft. This instrument operates at 2111.5 cm^{-1}, detecting the CO P(8) absorption line. It is a fully autonomous instrument and is capable of making measurements of CO every 2 seconds. Calibration is carried out both pre-flight and during flight, using the NOAA CMDL standards as reference. CO measurements from Argus are accurate to ~3% [Lopez *et al.*, 2008].

4.2.4. European AQUA Thermodynamic Experiment (EAQUATE)

Some *in situ* profiles were also obtained from the EAQUATE campaign [Taylor, 2005], operated by the Facility for Airborne Atmospheric Measurements (FAAM). These flights provided CO profiles in locations around the coast of the U.K.. As for the AVE campaign, the coincidence with AIRS overpasses is good for the

EAQUATE data. The altitude range covered by the profiles is ~0 km to ~11 km. CO measurements are made using the Aero-Laser Gmbh AL5002 Fast Carbon Monoxide (CO) Monitor. This is a resonance fluorescence instrument that provides measurement speed and accuracy comparable with the TDLAS instrument used in the AVE campaign [Gerbig *et al.*, 1999].

4.2.5. Constructing the Data Set

Having identified suitable aircraft measurement campaigns, some additional work was required to extract and format data from these campaigns into a coherent data set, appropriate for comparison with the AIRS CO retrievals. This process involved both the processing of the *in situ* aircraft data and the selection and processing of coincident AIRS data. As the format of the *in situ* aircraft data differed across the measurement campaigns (e.g. different profile levels and mixtures of profiles and flight path measurements) it was necessary to process this data into a single profile format across all measurement campaigns.

The CMDL campaign consisted of only profile data, but both AVE and EAQUATE contained a mixture of profile and fixed-altitude flight path data. Ascending and descending profiles were extracted from the data for each flight and were treated as independent CO profiles. Only profiles with measurements at altitudes within the range of levels used in the *a priori* profile, $\mathbf{x_a}$, were used. Treating the data in this way helped to limit the spatial and temporal variations present in the measurements of each profile, allowing more accurate collocation with the AIRS observations. Some of the aircraft data also contained in-flight calibration measurements. Where such measurements were present in a profile, linear interpolation using the measurements at the surrounding levels were used to replace the CO calibration values.

It was also necessary to apply some quality control measures in the construction of the *in situ* data set. Quality control flags present in the aircraft data sets were used to filter out poor quality measurements. Where possible, data flagged to be of low quality was replaced by linearly interpolation from measurements at surrounding levels. Care was taken not to perform such interpolation over large altitude ranges, with profiles suffering from low quality measurements over significant altitude ranges either truncated or removed from the data set. Having performed the processing steps discussed above, the aircraft profiles were then interpolated onto the STOCHEM pressure levels, within the pressure range of the *in situ* profiles, to provide a coherent set of *in situ* profiles. No extrapolation or substitution of a reference profile was carried out for levels beyond this range.

Having assembled the data set of *in situ* profiles, a data set of collocated AIRS data was collated using the following criteria: within ±6 hours and ±1° latitude and longitude from the mean observation time and location of the *in situ* profile. Before comparisons with aircraft data were made the UoE CO retrievals meeting the coincidence criteria were averaged for each *in situ* measurement.

4.3. Methods of Comparison

4.3.1. Percentage *a priori*

An important consideration when trying to analyse the effectiveness of an optimal estimation retrieval is the degree of contribution from the *a priori*. There is little use in comparing retrievals that are dominated by the *a priori* with *in situ* measurements, as this only really shows that there is little information available in the measurements, while revealing how close the *a priori* is to the true state. A more useful analysis of the performance of the retrieval can be made by filtering the data using the percentage *a priori* statistic. This is defined as the ratio of the diagonal elements of $\mathbf{S_a}$ and $\hat{\mathbf{S}}$ (Eq. 4.1):

$$PP(i) = 100.0 \times \left(\frac{\hat{\mathbf{S}}(i,i)}{\mathbf{S}_a(i,i)} \right), i = 1,...,n. \tag{4.1}$$

By only considering retrievals where $PP < 50\%$, a clearer picture of the accuracy of the retrieval can be obtained. Due to the lack of sensitivity of the AIRS instrument to

CO near the surface and in the upper-troposphere (illustrated by the averaging kernels in Figure 3.13 and Figure 3.14), the percentage *a priori* figure is unlikely to fall below 50% at these levels. Instead of rejecting such data, the entire profile is considered to have passed the percentage *a priori* test if $PP < 50\%$ for levels at 350, 550 and 750 hPa. As the AIRS v4 CO retrieval does not employ optimal estimation techniques, equivalent information is not available in the AIRS L2 product. The AIRS v4 retrievals are excluded from the analysis on the basis of the QUAL_CO flag (in the AIRS L2 data), set when the retrieval is replaced by “first guess” profile. Only data where this flag is not set is considered in the validation study.

4.3.2. Averaging Kernel Transformation

Direct comparison of the CO retrieval with *in situ* observations (or other remote sounding observations) provides a useful insight into the performance of the retrieval scheme. Although it is very useful for understanding and illustrating some features of the retrieval, such as the resolution, it is perhaps not the most appropriate method of comparing CO observations from independent sources. This is due to the fundamental nature of the inverse problem, where the retrieval is the best estimate of the state given the measurements and prior knowledge, rather than a simple direct measurement of the actual state. Rodgers and Connor [2003] propose some techniques to enable more appropriate comparisons to be made. One of these techniques is to apply the averaging kernels, **A**, from the retrieval to the *in situ* profiles using the transformation:

$$\mathbf{x}_s = \mathbf{x}_a + \mathbf{A}(\mathbf{x}_h - \mathbf{x}_a), \qquad \mathbf{4.2}$$

where $\mathbf{x}_\mathrm{h}$ is the *in situ* profile, or a profile from an alternative remote sounding instrument or retrieval method.

The effect of this transformation is to give $\mathbf{x}_\mathrm{h}$ the theoretical properties of the UoE retrieval. The resultant smoothed profile, $\mathbf{x}_\mathrm{s}$, is the profile that would be retrieved by the UoE method in the absence of retrieval error (i.e. noise and forward model error) if $\mathbf{x}_\mathrm{h}$ were the true state. Comparison of $\hat{\mathbf{x}}$ with $\mathbf{x}_\mathrm{s}$ rather than $\mathbf{x}_\mathrm{a}$ eliminates the smoothing effects

4.4. Profile Retrievals

A number of features of the retrieval scheme can be illustrated by looking at some examples of the retrieved profiles, Figure 4.2. The lack of sensitivity of the retrieval scheme to CO near the surface and in the upper troposphere is shown in Figure 4.2a. In this example the *in situ* data contains high and low CO concentrations in the lower and upper troposphere respectively. The extremes of this range are not present in the retrieved profile, as the lack of sensitivity to CO at these levels results in $\hat{\mathbf{x}}$ being dominated by $\mathbf{x}_a$ and the covariances of $\mathbf{S}_a$. This point is further highlighted by the averaging kernels shown in Figure 4.2b, all of which peak at mid-troposphere levels.

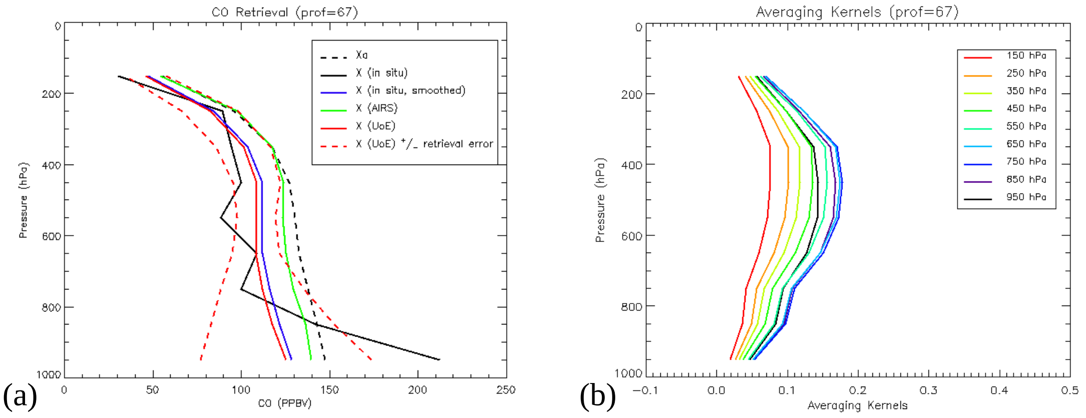

Figure 4.2 (a) An example from the validation data set, of the CO profile retrieved from the UoE scheme compared to *in situ* data and the AIRS v4 CO product. (b) The corresponding averaging kernels from the UoE retrieval.

The smoothing effect of the averaging kernels is also demonstrated in Figure 4.2a. Here the finer scale features of the present in the aircraft profile are replaced by a smoothed curve, resembling the shape of $\mathbf{x}_a$, in the retrieved profile, $\hat{\mathbf{x}}$. The smoothing effect in the retrieval is also clearly visible in $\mathbf{x}_S$, the aircraft profile with the averaging kernel transformation (Eq. 4.2) applied. In this example the UoE retrieval $\hat{\mathbf{x}}$ is in very good agreement with the smoothed aircraft profile $\mathbf{x}_S$, and differs from the prior by more than one sigma in the mid-troposphere, suggesting a degree of success for this particular retrieval.

4.5. CO At Different Altitudes

The CO retrievals were compared to the *in situ* measurements in the validation data set at each profile level. Results of this comparison at the 550 hPa level, where AIRS is expected to be most sensitive to CO (as discussed in §3.2), are presented in Figure 4.3. For this comparison the UoE retrievals have been filtered to exclude data where the percentage *a priori* > 50% at the 550 hPa level.

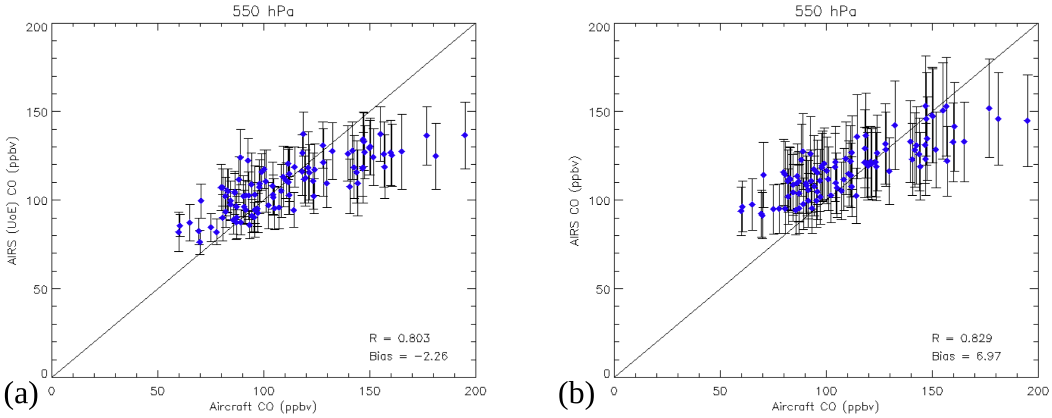

Figure 4.3 Direct comparison of CO concentrations at 550 hPa. (a) *in situ* vs UoE CO . (b) *in situ* vs AIRS v4 CO. Only retrievals with percentage *a priori* < 50% are considered.

There is fairly high correlation (R > 0.8) between both retrieval methods and the *in situ* observations. However, neither retrieval scheme is able to match the dynamic range of the *in situ* data. This is illustrated by positive and negative biases when the *in situ* CO concentration is low and high respectively. In the case of the UoE scheme this may be a result of error contributions to the retrieval scheme forcing $\hat{\mathbf{x}}$ towards $\mathbf{x}_a$, thus applying a constraint on the range of CO values. Another interesting feature in Figure 4.3 is the difference in the error estimates between the two retrievals. At 550 hPa the error estimates from the UoE system are significantly less than those from the AIRS v4 retrieval. The mean UoE retrieval error is ~12% compared to ~21% for the AIRS v4 retrievals. From equivalent analysis at different altitudes, the UoE error estimate is seen to increase away from the mid-troposphere, as might be expected given our knowledge of the instrument's varying sensitivity to CO throughout the troposphere. The same behaviour is not observed in the AIRS v4 error estimate, which returns similar values at all levels in the profile, a somewhat unrealistic result. This more realistic representation of the retrieval errors on altitude levels suggests an advantage in using the optimal estimation technique.

The inability of the retrieval scheme to fully capture the range of CO concentrations observed in the *in situ* data is further emphasised when the averaging kernel transformation is applied (Figure 4.4). Although the degree of correlation is increased the range of $\mathbf{x}_s$ is significantly lower than that of the original *in situ* profiles, $\mathbf{x}_h$.

Correlation between *in situ* observations and the UoE retrieval decreases as the altitude level approaches the lower and upper-troposphere levels. Away from the mid-troposphere levels, it is also observed that fewer cases meet the percentage *a priori* sampling criteria. This is the expected result from knowledge of the averaging kernels and the behaviour of the MAP algorithm. At profile levels where AIRS is less sensitive to CO the UoE retrieval will tend towards $\mathbf{x}_a$, with an accompanying increase in the retrieval error estimate, contained in $\hat{\mathbf{S}}$. This information, intrinsic to the optimal estimation technique, provides an accurate picture of whether the values in $\hat{\mathbf{x}}$ are a measure of the true state, $\mathbf{x}$, or a dependence on $\mathbf{x}_a$.

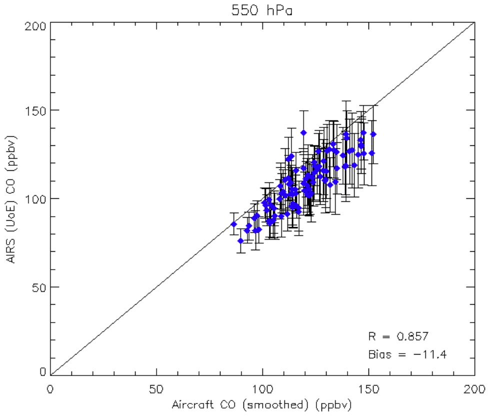

Figure 4.4 Comparison of CO concentrations at 550 hPa for the UoE retrieval, $\hat{\mathbf{x}}$, and the *in situ* measurements smoothed by the averaging kernel transformation of Eq. 4.2, $\mathbf{x}_s$.

4.6. Total Column CO

As the averaging kernels (§3.5.3) indicated that the AIRS radiances may typically only provide one independent piece of information about the CO profile, the total column CO is perhaps the most appropriate value to investigate. The *in situ* profiles cover different altitude ranges so total column CO values were calculated only across the levels, common in both aircraft and AIRS profiles, for each *in situ* profile. Figure 4.5a and Figure 4.5b show comparisons of the Total Common Column (TCC) CO between the *in situ* data and the UoE and AIRS retrievals (TCC_{IS}, TCC_{UoE}, and TCC_{AIRS}). The total column values for the *in situ* and AIRS data are based on the original profiles, without the averaging kernel transformation (Eq. 4.2) applied. Results from the smoothed profiles will be referred to as TCC_{ISS} and TCC_{AIRSS}.

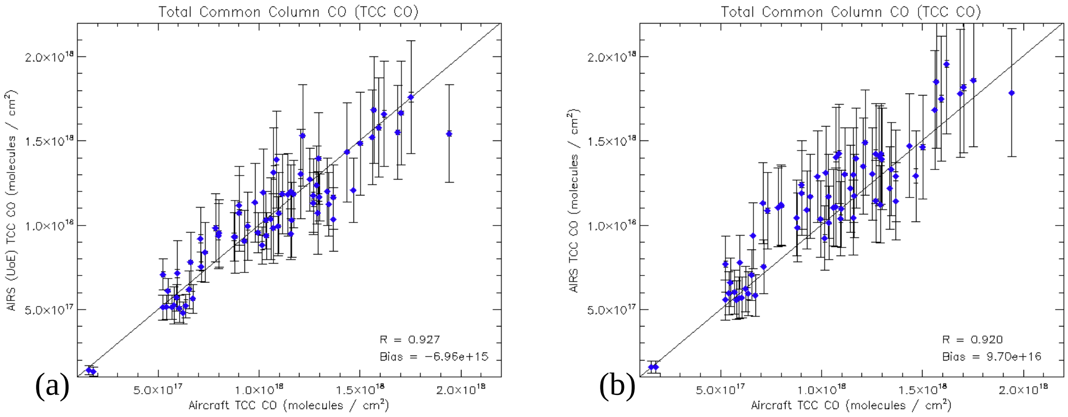

Figure 4.5 Direct comparisons of Total Common Column (TCC) CO retrievals with TCC CO from *in situ* measurements for the validation data set. (a) *in situ* vs UoE CO. (b) *in situ* vs AIRS v4 CO

Figure 4.5 shows that both retrieval schemes show good agreement with the *in situ* measurements for TCC CO, with $R > 0.9$. The error estimates from the retrieval schemes are also similar, with mean errors (relative to the mean *in situ* profile) of ~18% and ~23%, for TCC_{UoE} and TCC_{AIRS} respectively. From the results of §4.5 this similarity in TCC CO error estimates is a result of the AIRS v4 retrieval underestimating the errors in regions of low CO sensitivity and overestimating the error in regions of high CO sensitivity, relative to the UoE retrievals. There is a small negative bias (<1%) relative to the *in situ* profiles in the UoE retrievals. The bias in the AIRS retrievals is positive and considerably larger (~13%). This fairly large bias may be due to the AIRS v4 retrieval returning profiles close to their "first guess" which is higher than the mean of the aircraft profiles. Unlike the UoE retrievals there is no diagnostic available to allow data to be excluded on the basis of contribution from the *a priori* or "first guess".

The results of applying (Eq. 4.2) to the *in situ* profiles are shown in Figure 4.6. Applying the averaging kernel transformation improves the correlation (R=0.97) and significantly reduces the standard deviation of the distribution from ~14% to ~8% of the mean TCC_{ISS} value. Along with these improvements, the averaging kernel transformation also introduces a significant negative bias (~7%), approximately a factor of 10 increase. The negative bias introduced by the averaging kernel transformation is potentially a consequence of the use of truncated profiles in the *in situ* data set, and therefore applying truncated versions of the averaging kernels in the transformation. Using these truncated versions of **A** will result in a somewhat different smoothing being applied to the *in situ* profiles, than the UoE retrieval scheme applies to the true atmospheric state, and may be the cause of the bias observed in Figure 4.6.

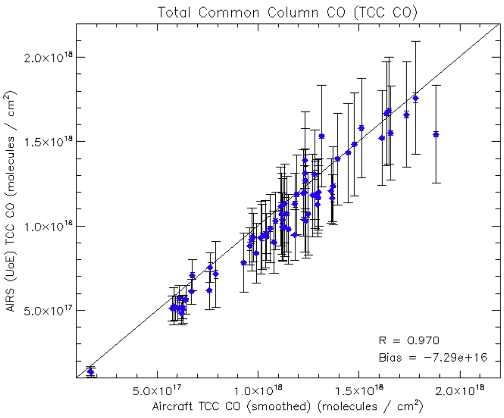

Figure 4.6 Comparison of total column CO from the UoE retrieval (TCC_{UoE}) with that from the *in situ* data with the averaging kernel transformation (Eq. 4.2) applied (TCC_{ISS}).

Direct comparisons between the UoE and AIRS v4 retrievals were also made (Figure 4.7). These total column values are for the full profiles, as the profiles from both retrievals cover the same altitude range. As the two retrieval schemes give comparable results when evaluated against the *in situ* data, it is no surprise that a high degree of correlation is observed when the two methods are compared directly. Although there is very good correlation there is also quite a significant bias, with the UoE retrieval typically about 10% lower than that from the AIRS v4 product. The likely reason for this bias could be that there is a larger dynamic range in the UoE retrievals. As the mean *in situ* profile is lower than the *a priori* (and "first guess"), a less constrained retrieval scheme could result in typically lower TC CO values over this data set.

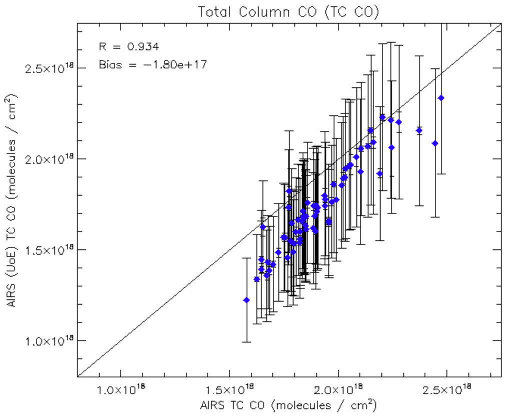

Figure 4.7 Comparison of total column CO retrievals from UoE and AIRS v4 retrieval schemes for the validation data set.

4.7. Summary

In this chapter, the details of a validation study for the UoE retrieval and its results are presented. A set of over 100 *in situ* aircraft measurements of CO profiles was collated and a corresponding set of AIRS data (matched spatially and temporally) was assembled. The UoE retrieval scheme was implemented using the AIRS L2 products as input to the fast forward model RTTOV, and the resulting CO profiles compared to the *in situ* measurements, and the AIRS v4 CO product.

Comparisons of total common column (TCC) CO revealed the UoE CO product to be well correlated with the *in situ* measurements. The AIRS v4 CO product was also shown to be similarly well correlated to the *in situ* data but was significantly more biased than the UoE product. Error estimates for both AIRS TCC CO products were similar, with mean values of ~20%.

CO concentrations on individual profile levels were also compared. High correlations between AIRS retrievals and the *in situ* measurements were observed in the mid-troposphere. At this level, the mean UoE retrieval error was shown to be considerably less than that from the AIRS v4 product (~12% compared to 21%). It was noted that away from the mid-troposphere levels, correlations between the UoE

CO product and *in situ* measurements decreased and the UoE retrieval error increased. This is due to decreasing sensitivity to CO at these levels and a subsequent increase in the influence of the prior on the retrieval. Similar behaviour was also noted in the AIRS v4 CO product but only in terms of correlations with *in situ* observations. Retrieval errors from the AIRS v4 product showed little variation with altitude, an unrealistic result that suggests the optimal estimation retrieval provides better characterisation of the retrieval errors.

Although the UoE CO product was shown to be well correlated with *in situ* measurements, it was also shown to have some limitations. In addition to the lack of sensitivity in the lower and upper troposphere, it was demonstrated that the UoE retrieval was also unable to capture the dynamic range observed in the *in situ* measurements. This is partly due to the fundamental differences between the measurement techniques. While the *in situ* data consists of localised point measurements, AIRS observes the CO over a considerable spatial area. Consequently, even at levels where AIRS is most sensitive to CO, it will not be able to detect the extreme concentrations that can be measured *in situ*.

Chapter 5. Comparison with MOPITT

5.1. MOPITT CO

5.1.1. Instrument details

The Measurements of Pollution in the Troposphere (MOPITT) instrument was launched aboard the EOS Terra satellite in December 1999, and has provided operational CO retrievals since March 2000. It is a nadir sounding instrument with spatial resolution of 22 km at the nadir. CO retrievals are performed using measurements of thermal IR emission in a band centred on 4.62 μm and gas correlation radiometry techniques (outlined below and described in more detail by Deeter *et al.* [2003] and Niu *et al.* [2004]).

Modulation cells in the MOPITT instrument contain CO and act as high spectral resolution optical filters. The filtering characteristics of the cells are varied dynamically, through modulation of the cell pressure or the optical path length, giving rise to Pressure-Modulated Cells (PMC) or Length-Modulated Cells (LMC) respectively. By averaging or differencing the transmitted optical intensity in the modulation cell states of minimum and maximum absorption, information about different spectral regions can be obtained. The average “A” signals are primarily sensitive to the spectral regions between the CO absorption lines, where variability in the radiances is dominated by surface temperature. In contrast, the difference “D” signals are highest close to the CO absorption lines, making the “D” signals relatively much more sensitive to CO concentrations than the “A” signals. As the spectral position of the maximum of the “D” signal response is dependent on the characteristics of the modulation cell, it is possible to look at different parts of the line wings by modulating the cell. Thus, because of atmospheric pressure broadening, MOPITT is able to obtain CO information at different altitudes.

The current MOPITT CO retrieval algorithm, v3 [Emmons *et al.*, 2004], uses “A” and “D” signals from an LMC and the “D” signal from a PMC. These combine to provide sensitivity to CO over a range of altitudes, with the LMC having sensitivity across a broad range from the lower to upper troposphere while the PMC enhances the sensitivity of MOPITT in the upper troposphere. As with the AIRS channels used in the UoE retrieval scheme (Chapter 3) MOPITT is sensitive to both tropospheric CO and other geophysical parameters such as temperature and water vapour.

5.1.2. Retrieval Scheme

The MOPITT retrieval algorithm shares the same basis as the UoE algorithm for AIRS, using the *maximum a posteriori* (MAP) solution [Rodgers, 2000] and employing it in a Newtonian iteration scheme. As for the UoE method the MOPITT retrieval uses a fixed global prior $\mathbf{x_a}$ and associated covariance matrix $\mathbf{S_a}$. Both of these are determined from a set of *in situ* aircraft profiles with monthly climatology values from the CTM "MOZART" [Hauglustaine *et al.*, 1998] used at high altitudes, described in more detail by Deeter *et al.* [2003]. The *a priori* profile, $\mathbf{x_a}$, and its uncertainty are shown in Figure 5.1. This prior information is on a set of 32 fixed pressure levels. Retrievals of CO at such high vertical resolution are not possible and the final retrieved CO product is returned on a set of up to 6 fixed pressure levels (850, 700, 500, 350, 250, and 150 hPa) with a further "floating" surface level [Deeter *et al.*, 2003]. The *a priori* profile used in the MOPITT retrievals is considerably lower than the AFGL US standard profile used in the UoE retrieval scheme for AIRS (Figure 3.6). This has potential to introduce biases between the two retrievals. However, as both retrievals use the same optimal estimation techniques, the degree of contribution from the prior can be determined, allowing any such biases to be better characterised.

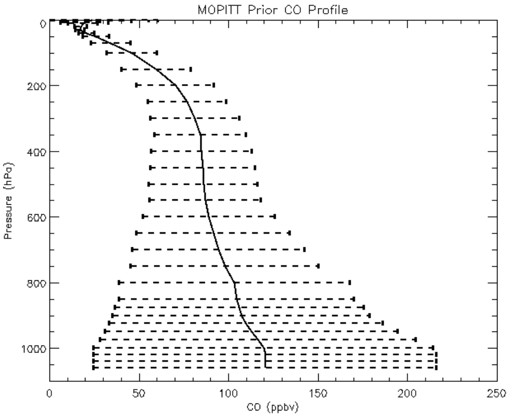

Figure 5.1 MOPITT *a priori* and associated error from MOPITT $\mathbf{S_a}$.

5.1.3. Retrieval Performance

As MOPITT has been operational since 2000 and CO is one of its core products, extensive validation and analysis of its CO product has been carried out (Deeter *et al.* [2004] and Emmons *et al.* [2004]). Deeter *et al.* [2004] investigated the information content of the MOPITT CO profiles, showing the number of degrees of freedom, d_s, to typically lie between ~0.5 and 1.7. They also observed the general trend of decreasing d_s from the tropics to the poles and diurnal variations in d_s over the land.

Analysis of the averaging kernels by Deeter *et al.* [2003] showed MOPITT to have limited sensitivity to CO in the boundary layer, with retrievals at the surface and 850 hPa levels dominated by CO at higher altitudes and by the prior. Figure 5.2 shows an example of MOPITT averaging kernels, taken from Deeter *et al.* [2003]. These are typical MOPITT averaging kernels for night time retrievals over the central Pacific. They illustrate the lack of sensitivity to CO near the surface, with both the surface and 850 hPa averaging kernels peaking at 500 hPa. When compared to the averaging kernels from simulations of the UoE retrieval scheme for the AFGL tropical atmosphere (Figure 3.14), the MOPITT averaging kernels can be seen to offer greater distinction between CO at different altitudes, with clear differences in the shape and peak altitude of the averaging kernels in the lower and upper troposphere. Deeter *et al.* [2003] proposed that MOPITT has the potential to distinguish between CO in the upper (350 to 150 hPa) and lower (surface to 700 hPa) troposphere.

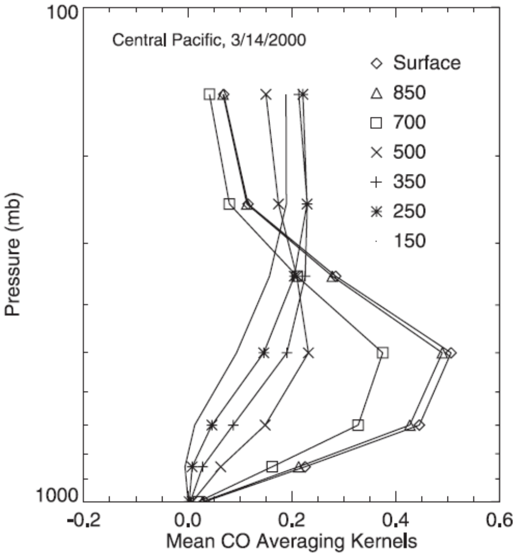

Figure 5.2 Mean MOPITT averaging kernels for night time retrievals over the central Pacific ocean (region defined by 10°S, 10°N, 180°W, and 150°W) on March 14, 200. Taken from Deeter *et al.* [2003].

Deeter *et al.* [2003] also demonstrate diurnal variability in the MOPITT averaging kernels, through the analysis of the mean daytime and night time averaging kernels over western Australia. The mean averaging kernels calculated by Deeter *et al.* [2003] are shown in Figure 5.3. These illustrate the effect of diurnal surface temperature variations on the MOPITT retrievals. Higher daytime surface temperatures result in the peaks of the lower troposphere levels being shifted closer to the surface, indicating that the sensitivity of MOPITT to CO is higher under these conditions. The reverse is true for night time retrievals and the averaging kernels for different altitude levels become less distinguishable.

In addition to the work of Deeter *et al.* [2003], Emmons *et al.* [2004] also conducted an extensive validation study with *in situ* aircraft measurements, and observed a small negative bias (~2-3%) in the MOPITT retrievals at all profile levels. Although the overall bias observed was small, large variations in the bias were observed between different regions, with the largest biases observed in clean CO regions.

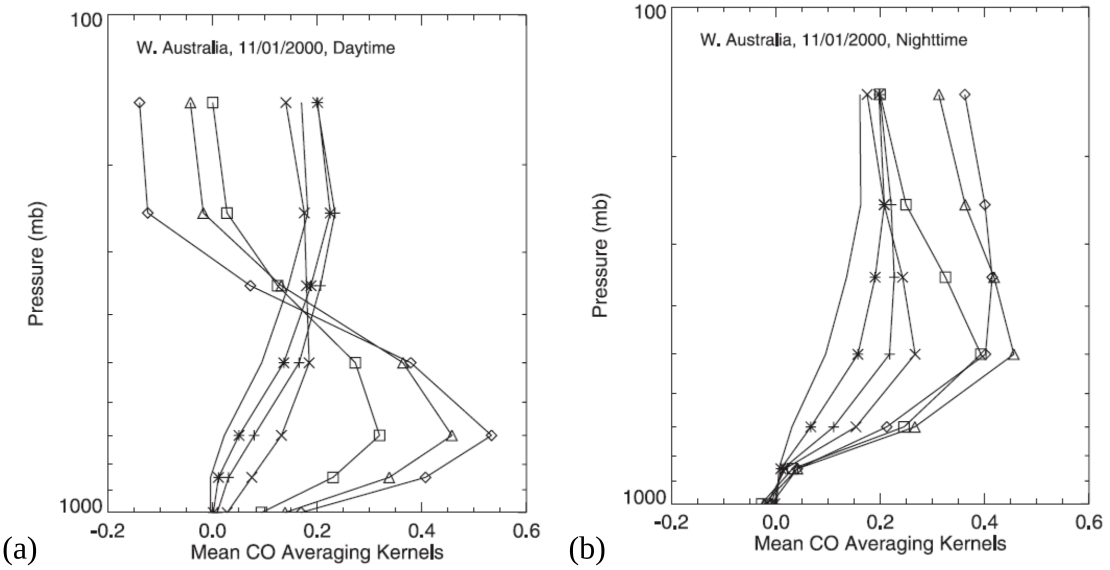

Figure 5.3 Mean MOPITT averaging kernels for (a) daytime and (b) night time retrievals over western Australia (region defined by 30°S, 15°S, 120°E, and 140°E) on November 1, 2000. Taken from Deeter *et al.* [2003].

5.2. MOPITT vs AIRS

5.2.1. Introduction

As MOPITT is an established and well documented satellite instrument for global CO observations, it can be regarded as a useful benchmark for observations from other instruments. As such, an extensive comparison study was carried out, between CO from MOPITT, AIRS (v4) and the UoE retrieval scheme. AIRS data covering a full year (2006) was obtained and processed using the UoE method. Daily averages were then calculated for the same 1° by 1° (longitude by latitude) grid used for the MOPITT level 3 (L3) CO product. In the calculation of the daily averages, the filters used to produce the MOPITT L3 product [Emmons, 2002] were applied to the UoE observations for consistency. These filters are shown in Table 5.1.

Filter	Method
Land/Water	A land/water mask is used to determine the surface type for each grid box. Only pixels for this surface type are included in the average. This prevents inhomogeneous data from being averaged together.
Day/Night	Day and night pixels are averaged and reported separately. Pixels with solar zenith angle greater than 80° are classed as night. This filtering strategy is included because MOPITT exhibits considerably different sensitivity between day and night over land.

Table 5.1 Filters used in MOPITT L3 data and to produce daily averages from UoE retrievals.

5.2.2. Daily Averaged CO

The day and night time averages for CO at 500 hPa, for a sample day (24/10/2006), selected as it includes a region of strongly elevated CO, are shown in Figure 5.4. These plots compare the basic MOPITT L3 CO product with the equivalent UoE product. In this comparison no filtering of the data, based on the percentage prior or any other factor, has been carried out. The most striking feature of Figure 5.4 is the significantly higher coverage of the AIRS instrument. Considering both day and night data, AIRS provides coverage of ~70% of the globe compared to only 30% from MOPITT. This greatly improved coverage gives AIRS an obvious advantage over MOPITT, enabling a clearer picture of the global CO distribution to be obtained on a daily basis.

Figure 5.4 also shows reasonable agreement in the distribution of CO between the UoE and MOPITT products, with the high and low CO values being observed in the same regions. Both products show low CO values over the South Pacific and elevated CO over the Indian Ocean and Southern Africa. The correlation coefficients for these examples are ~0.45, with grid box match ups for approximately 10% of the globe. As the UoE and MOPITT retrievals use different prior profiles, and the daily averages may be dominated by these, a higher degree of correlation could be expected if some form of filtering based on the contribution from the prior is performed. The relatively low number of match ups between AIRS and MOPITT limits the usefulness of such comparisons of daily averages. Although a basic picture of the agreement can be formed, analysis over a longer time period is required to obtain a more meaningful result. Consequently, more in depth analysis was carried out looking at monthly averaged CO (§5.2.3 to §5.2.7).

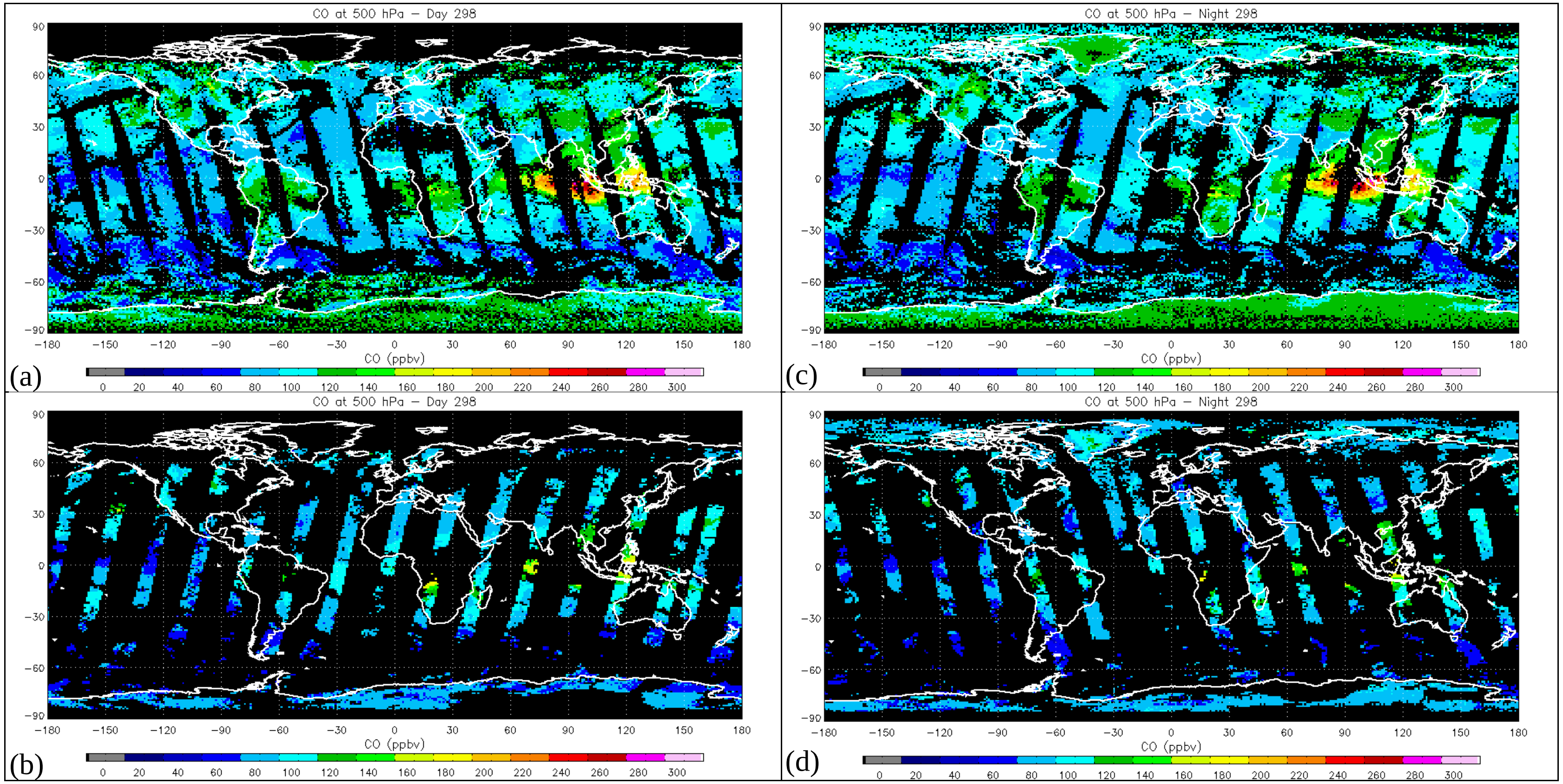

Figure 5.4 Daily average CO at 500 hPa for 24/10/2006, calculated on a 1° latitude by 1° longitude grid. (a) and (c) UoE day and night. (b) and (d) MOPITT day and night.

5.2.3. Monthly Averaged CO - Spatial Coverage and Data Filtering

The monthly average daytime CO was calculated from the daily products for MOPITT, AIRS v4 and UoE. Examples of these monthly averages for October 2006 are shown in Figure 5.5. October 2006 was selected because of the elevated CO observed over Indonesia and surrounding area during this month. When the raw CO product, with no filtering, is considered the AIRS instrument is again seen to provide improved spatial coverage compared to MOPITT. Although both instruments provide good coverage on a monthly timescale, more grid boxes contain no valid data in the MOPITT data. The poorer daily coverage of MOPITT makes it more susceptible to data loss due to cloud cover. This problem is reduced further by AIRS through the use of cloud cleared radiances, allowing retrievals to be performed in the presence of significant cloud cover [Susskind *et al.*, 2003]. It is likely that the gaps in MOPITT coverage are largely due to persistent cloud cover. It is also possible that the MOPITT cloud clearing algorithm may falsely flag smoke from extensive biomass burning as cloud. This may contribute to the relatively poor MOPITT coverage over Indonesia (Figure 5.5b).

Although the spatial coverage of the raw products from AIRS and UoE is somewhat better than for MOPITT, any potential benefit of this is limited by the quality of the CO product. In the UoE and AIRS products, elevated CO values are observed over Antarctica, a region where low concentrations of CO are expected. The same is true for MOPITT, with higher CO observed over Antarctica than the surrounding Southern Ocean. In all cases the values over Antarctica are essentially the prior (MOPITT and UoE) or first guess (AIRS). This is confirmed when the daily CO data is filtered to remove all data with % prior greater than 50% at 500 hPa from the monthly average (Figure 5.6). Excluding the data dominated by the prior, for the most part, results in the removal of the dubiously high values over regions like Antarctica from the monthly average UoE and MOPITT products. The lack of information about the quality of the retrieval in the AIRS product makes equivalent data filtering impossible, and therefore the elevated CO values remain present in the AIRS product.

Another point to note about the effect of filtering the data is the reduction in CO values between the raw and filtered UoE products. This suggests that the daily average for some grid boxes is dominated by the prior for a considerable number of days over the course of a month. The same effect is not observed in the MOPITT product, suggesting that, when conditions allow a MOPITT retrieval to be made, it is usually dominated by the CO signal rather than the prior. One potential explanation for this difference between the instruments is the fact that the UoE retrieval utilises cloud cleared radiances. This allows retrievals to be performed for scenes with high levels of cloud cover that would be flagged as cloudy by MOPITT. Although CO retrievals can be made for such scenes, it is possible that the quality of the UoE retrievals is degraded by increased errors, introduced by clouds, in retrieval parameters derived from the AIRS L2 products.

For the purpose of inter-instrument comparisons and in general, it is desirable to filter the data in some way to limit the degree of contribution from the prior in the CO products. In an ideal retrieval where there is independent information in the measurements about each profile level, a filter based on 50 % prior at each level could be used. As both MOPITT and AIRS are relatively insensitive to CO in the lower and upper troposphere, and rely on prior knowledge of the inter-level correlations at these altitudes, such a filtering method would result in severely limited set of successful retrievals. A number of filtering thresholds, using different numbers of levels were investigated, before the simple rule requiring <50% prior at 500 hPa was selected for use in the remainder of this study. Only the 500 hPa level was used as this is typically the level where both AIRS and MOPITT have their highest sensitivity to CO. It was felt that putting additional constraints on other levels could result in useful upper troposphere retrievals being rejected due to a lack of information in the lower troposphere, and vice versa. It was also observed that using only the 500 hPa threshold test provided monthly products with very good global coverage. The application of this threshold test improves the correlation between the UoE and MOPITT retrievals from ~0.65 to 0.90, as a result of the reduction in the contribution from the different prior CO profile.

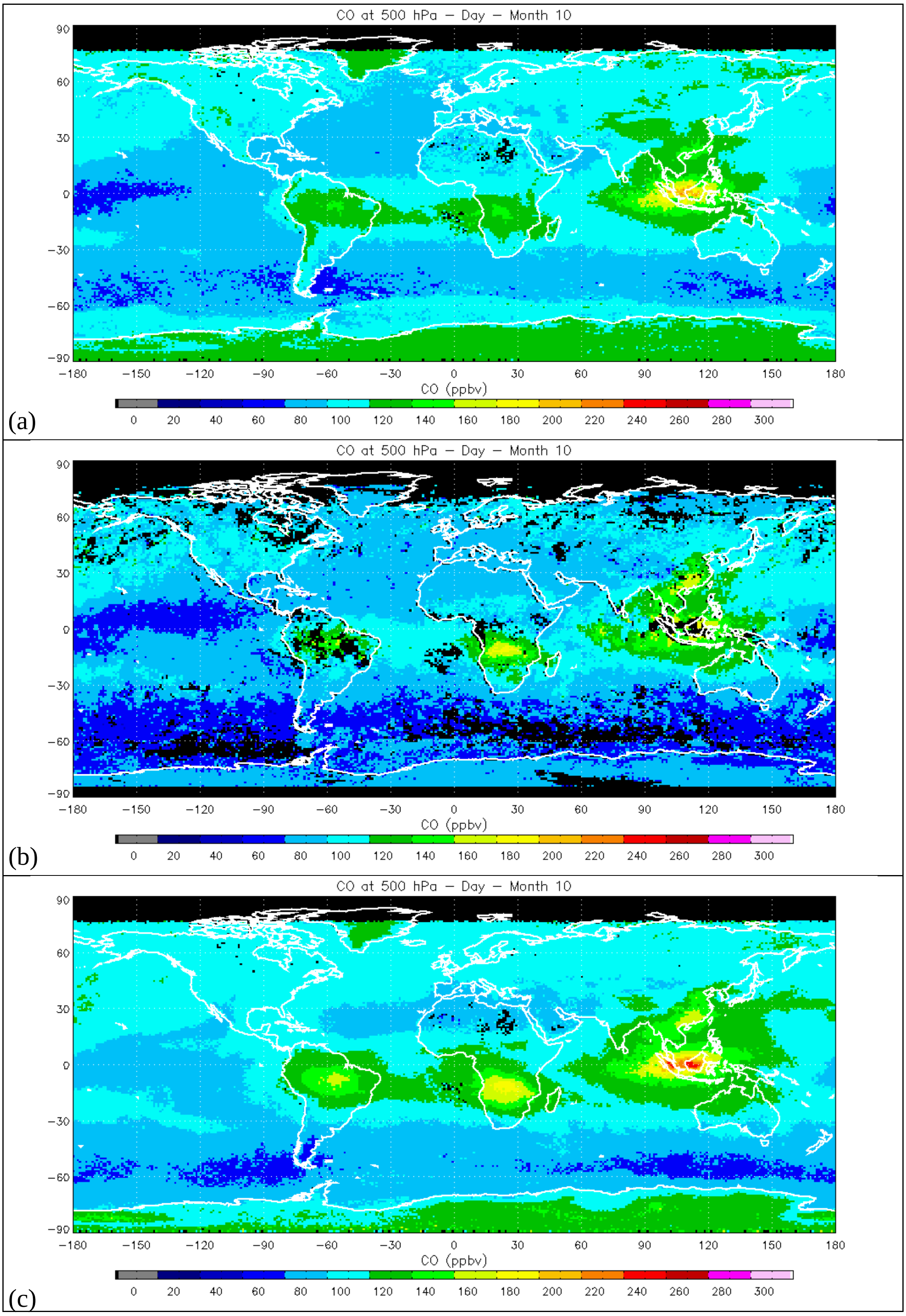

Figure 5.5 Monthly average daytime CO at 500 hPa for October 2006, using all data. (a) UoE, (b) MOPITT, and (c) AIRS v4.

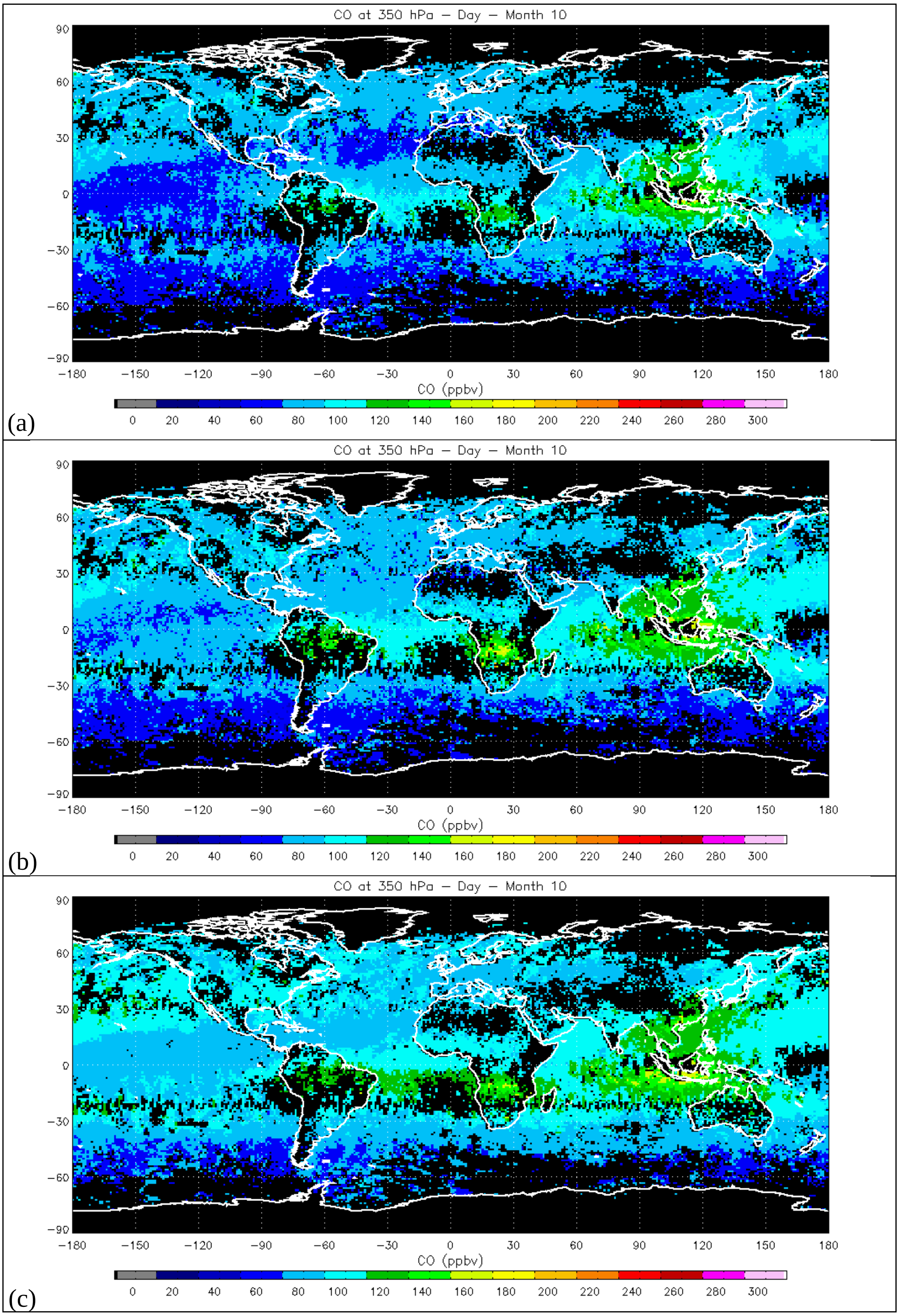

Figure 5.6 Monthly average daytime CO at 500 hPa for October 2006, filtering data with % prior > 50% at 500 hPa. (a) UoE, (b) MOPITT, and (c) AIRS v4.

5.2.4. Monthly Averaged CO - CO Profiles

The CO concentrations from the three methods (UoE, AIRS v4, and MOPITT) were compared at each individual pressure level in UoE and MOPITT profiles. As outlined in §5.2.3 the UoE and MOPITT products were filtered to exclude profiles with a contribution from the prior of more than 50% at 500 hPa. This comparison of the retrieval schemes was carried out for all 12 months and all profile levels for both daytime and night-time data. Global maps of daytime CO for the month of October 2006 and the levels, 700, 500 and 350 hPa, are presented in Figure 5.7, Figure 5.8, and Figure 5.9 respectively. In the calculation of these monthly averages only grid boxes containing valid retrievals from all three systems were included, so the coverage is less than for each data set individually. The coefficients of correlation between the three retrievals are given in Table 5.2, along with the biases relative to MOPITT (and AIRS for the UoE vs AIRS case). Correlation of CO from the two AIRS retrieval algorithms with MOPITT CO is plotted in Figure 5.10. Finally the distribution of inter-instrument CO differences are shown in Figure 5.11.

Comparison of the CO maps by eye suggests good agreement between the three measurement systems, particularly at 500 and 350 hPa. This is supported by the high correlation coefficients between all systems (Table 5.2). At 700 hPa MOPITT sees larger areas of elevated CO and also higher peak values than either of the AIRS-based retrievals (Figure 5.7). This is reflected in the lower correlation coefficients at this level and is a sign that MOPITT is more sensitive than AIRS to CO in the lower troposphere (as suggested by the UoE and MOPITT averaging kernels shown in Figure 3.14 and Figure 5.2 respectively). The lower sensitivity of AIRS at this level is further emphasised in the correlation plots Figure 5.10 (a) and (d). Here the UoE retrieval fails to capture most of the high CO concentrations observed by MOPITT, with the UoE CO tending toward $\mathbf{x_a}$. A similar result is seen in the AIRS v4 data but here the trend is more pronounced and occurs at both high and low CO concentrations, as seen by MOPITT. Again this is an indication that AIRS has a lack of sensitivity at this level and that there is considerable contribution from the “first guess” in the AIRS v4 product.

At 500 hPa, both AIRS and MOPITT are expected to have good sensitivity to CO. The more comparable sensitivity yields a higher degree of correlation between the instruments at this level (Table 5.2), also show by the similarities in the global maps (Figure 5.8). In Figure 5.10b the trend of UoE towards the prior at high MOPITT values is largely removed. The trends at low and high MOPITT CO values for AIRS v4 CO (Figure 5.10d) are also removed, with good agreement now observed between the instruments across the full range of CO values. Similar results are observed at 350 hPa but with slightly lower correlations than at 500 hPa and a less significant form of the trends seen at 700 hPa.

Although the correlation of the two AIRS CO products to MOPITT CO is similar, analysis of the global maps suggest the magnitude of the CO can differ considerably. Looking at 500 hPa (Figure 5.8) the AIRS v4 algorithm CO concentrations are generally higher than those from UoE and MOPITT. This is highlighted in Figure 5.11b where the histogram of the AIRS-MOPITT differences is seen to peak at +10 ppbv, while the UoE-MOPITT distribution is centred on zero. Table 5.2 illustrates this numerically with biases in UoE and AIRS v4 CO relative to MOPITT of 0.8 ppbv and 10.8 ppbv respectively. A reduced but positive bias is also present in the AIRS retrieval at 350 and 700 hPa. At these levels UoE CO exhibits a negative bias relative to MOPITT of similar magnitude to that of AIRS (~4-9 ppbv). Figure 5.10c suggests that this bias is caused by an underestimation of elevated CO by the UoE system relative to MOPITT. This may be a result of increased contribution from the prior at these levels in the UoE product. Filtering the data using a % prior threshold at these levels may reduce or remove this bias.

One final point to note about the histograms of CO differences is the significantly wider distribution at 700 hPa compared to 500 and 350 hPa. This is a combination of two factors; the greater sensitivity of MOPITT in the lower troposphere, and the higher variance of CO at lower altitudes.

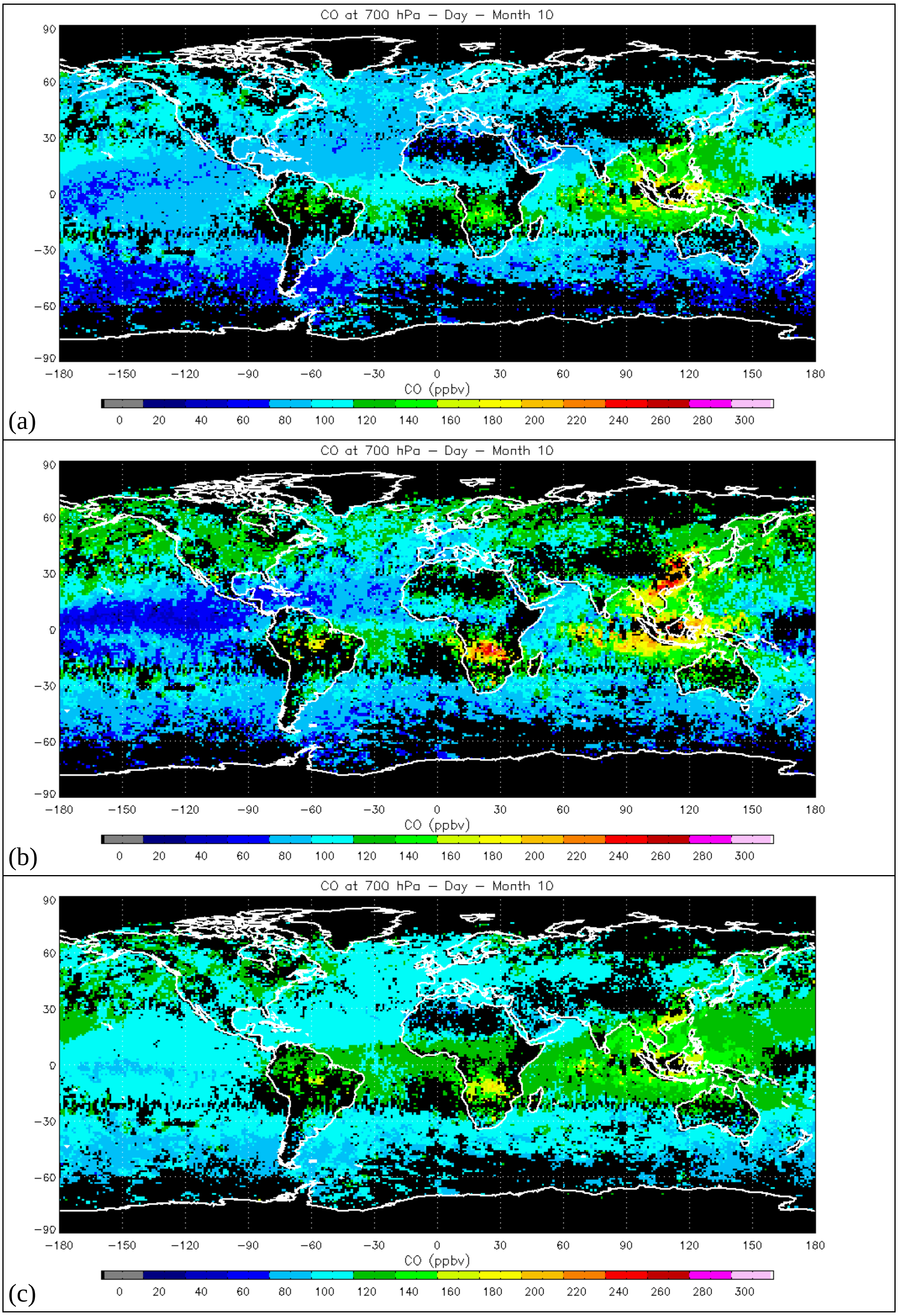

Figure 5.7 Monthly average daytime CO concentration at 700 hPa for October 2006. (a) UoE, (b) MOPITT, and (c) AIRS v4.

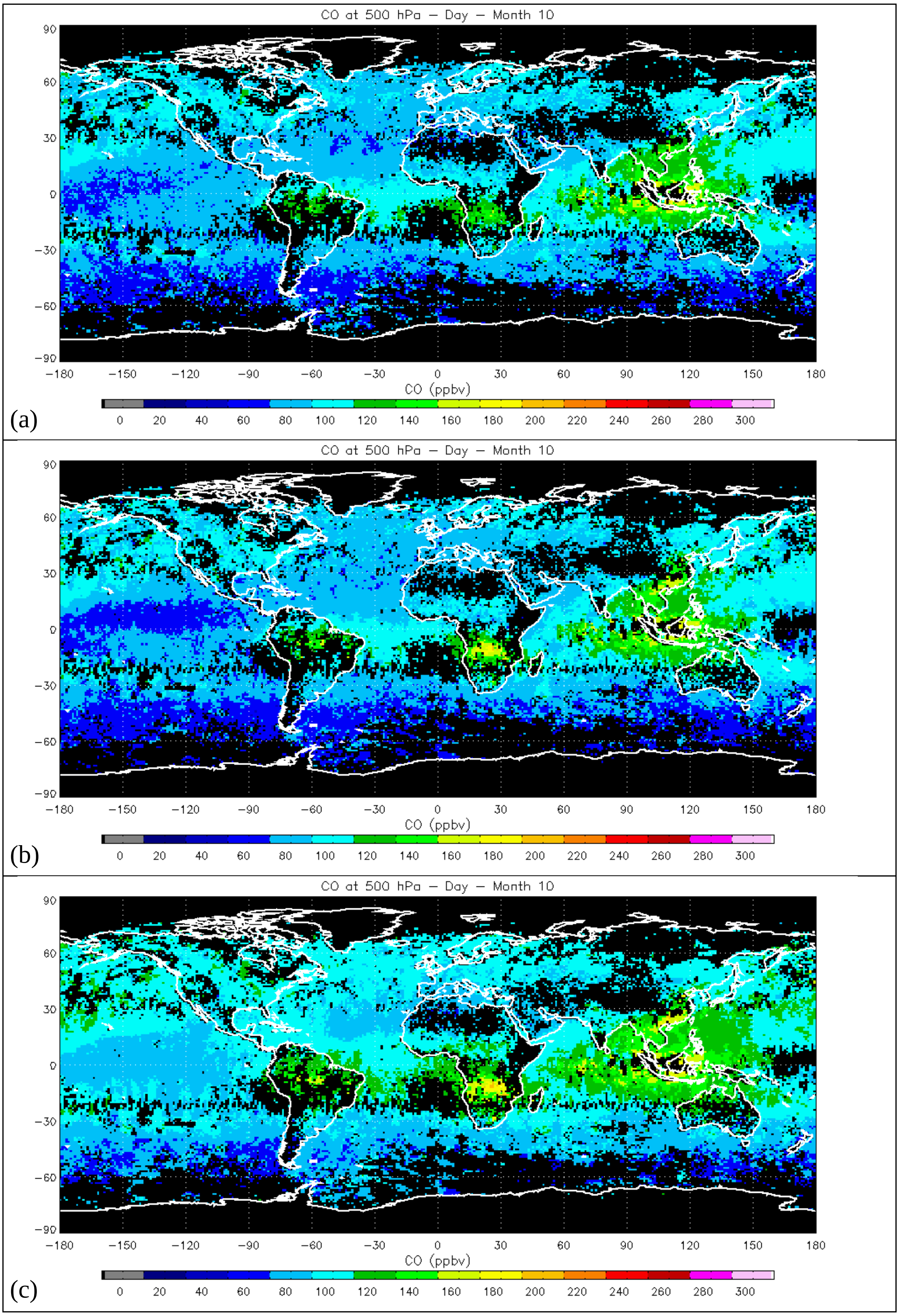

Figure 5.8 Monthly average daytime CO concentration at 500 hPa for October 2006. (a) UoE, (b) MOPITT, and (c) AIRS v4.

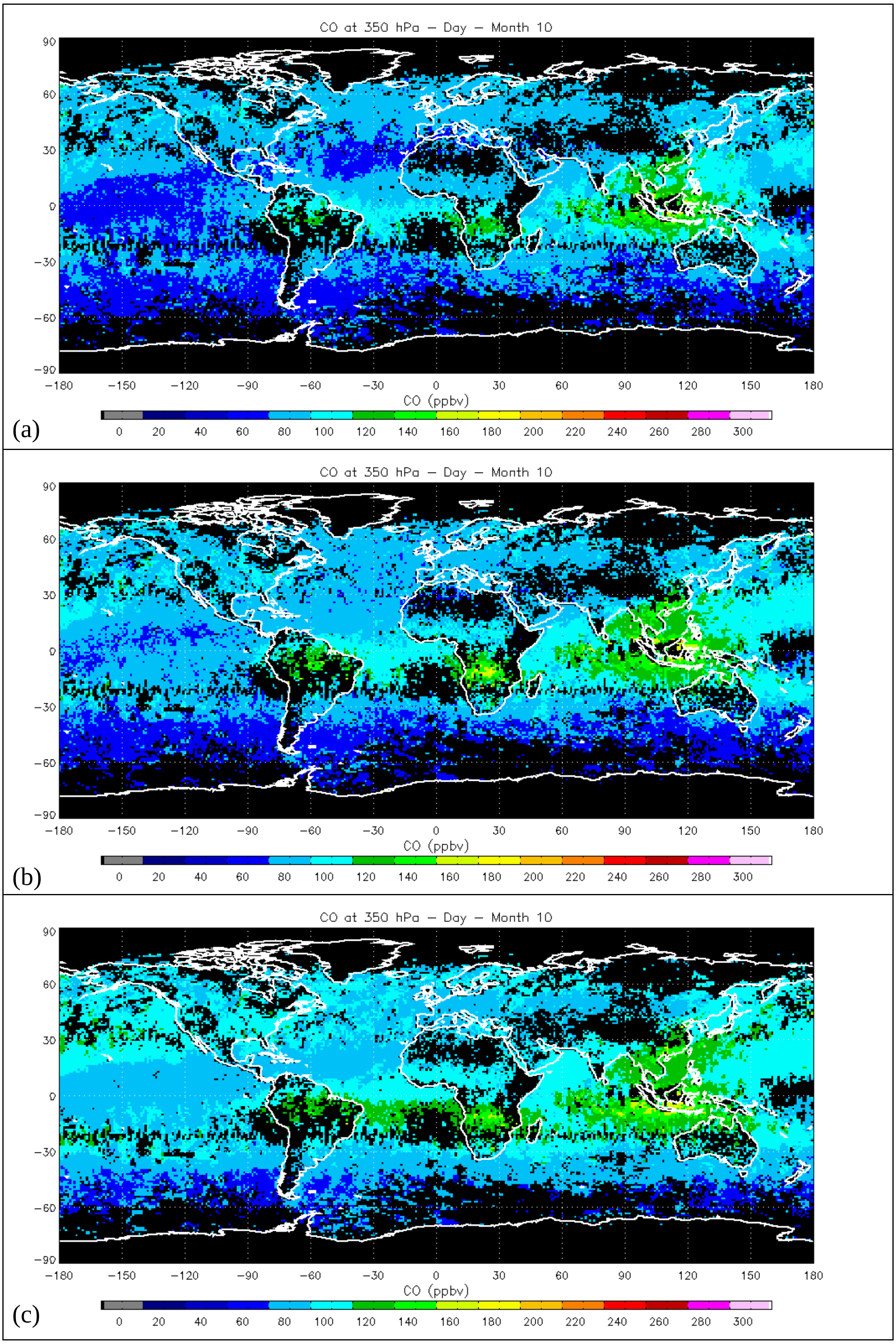

Figure 5.9 Monthly average daytime CO concentration at 350 hPa for October 2006. (a) UoE, (b) MOPITT, and (c) AIRS v4.

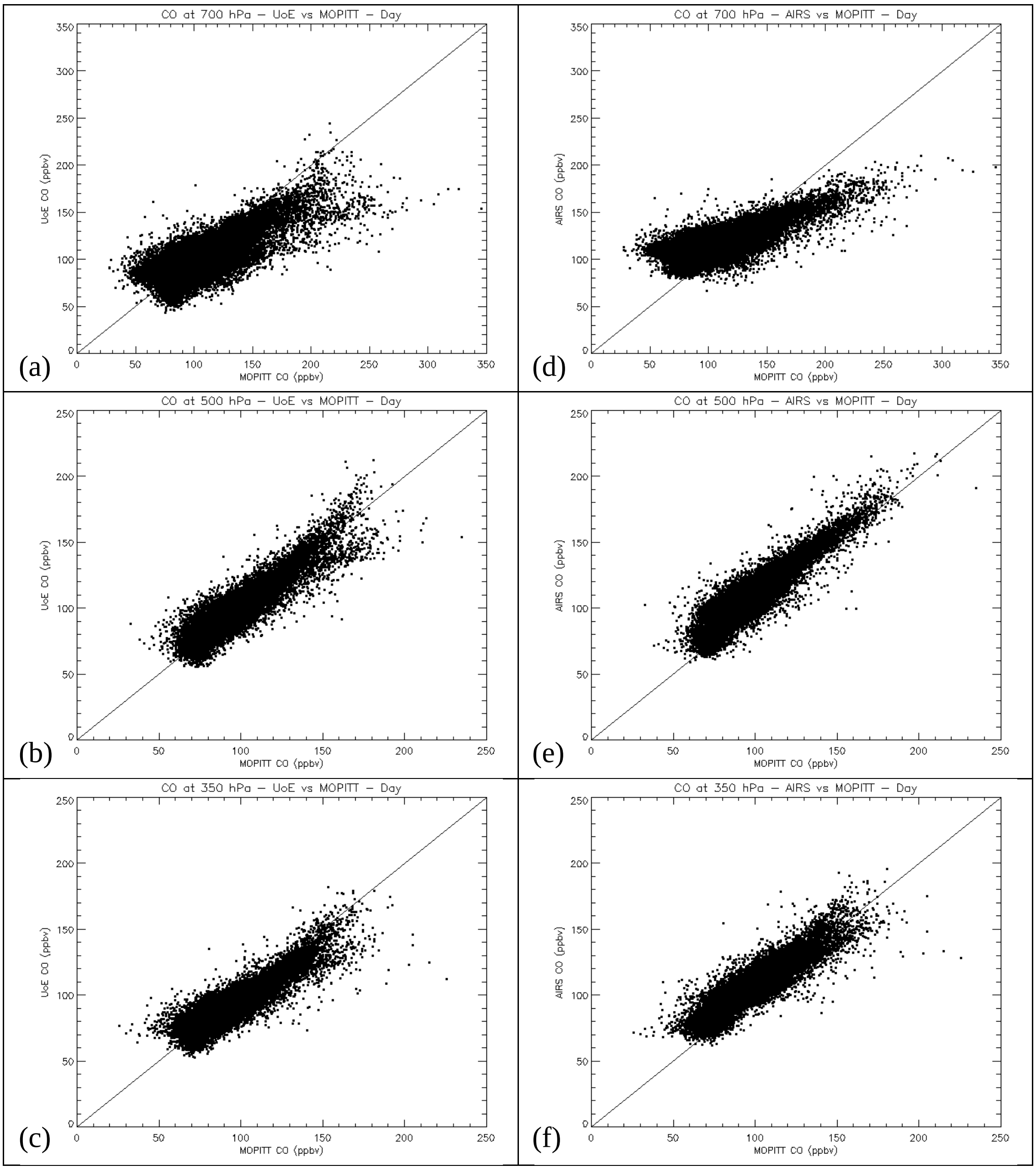

Figure 5.10 Correlation of CO between observing systems for October 2006. (a) to (c) UoE vs MOPITT at 700, 500 and 350 hPa. (d) to (f) AIRS v4 vs MOPITT at 700, 500 and 350 hPa.

Pressure Level (hPa)	**UoE vs MOPITT**		**UoE vs AIRS v4**		**AIRS v4 vs MOPITT**	
	R	**Bias**	**R**	**Bias**	**R**	**Bias**
350	0.89	-3.9	0.89	-11.5	0.90	7.7
500	0.91	0.8	0.93	-10.0	0.91	10.8
700	0.75	-8.5	0.92	-14.7	0.74	6.2

Table 5.2 Correlation coefficients and bias (ppbv) calculated for monthly mean CO for October 2006.

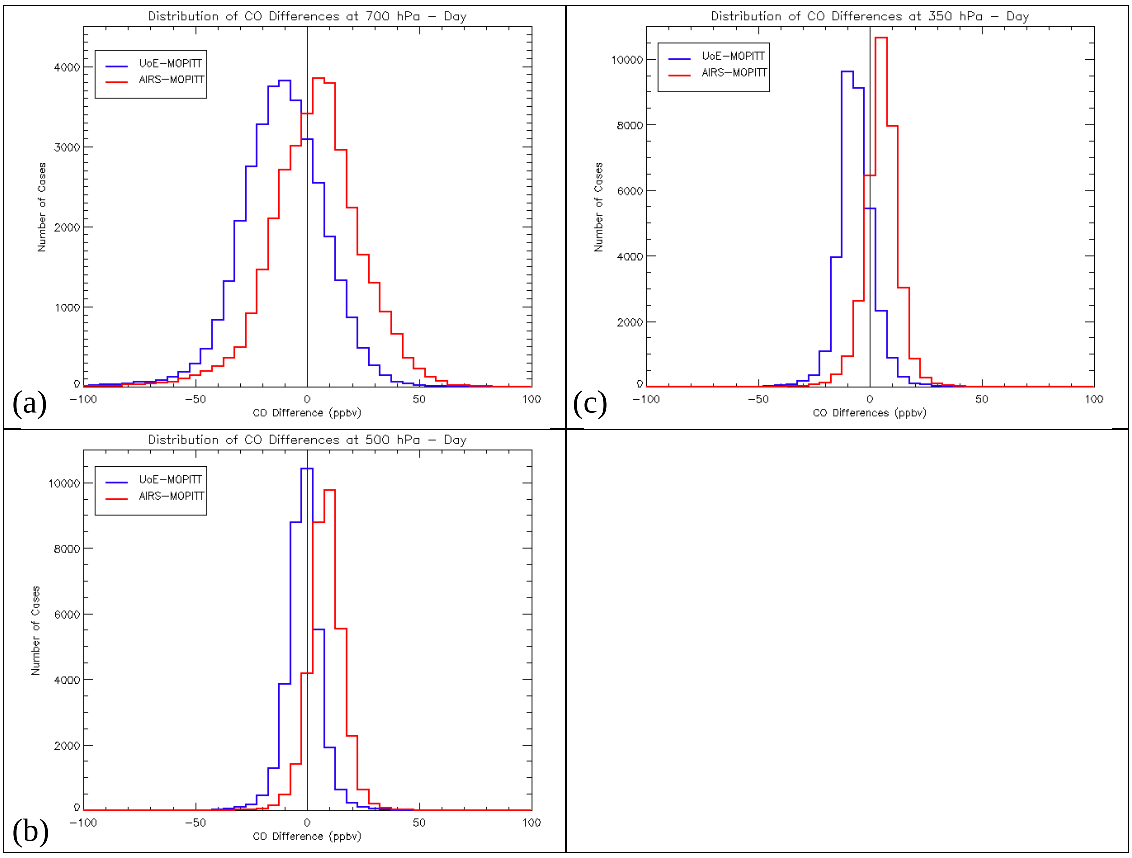

Figure 5.11 Distribution of CO differences between observing systems at (a) 700 hPa, (b) 500 hPa, and (c) 350 hPa. The histograms were calculated using a bin size of 5ppbv for October 2006.

In the comparison of UoE and MOPITT retrievals (Figure 5.10a to Figure 5.10c) some divergence in the distributions is apparent for high CO concentrations. This is most obvious for CO retrievals at 500 hPa (Figure 5.10b), where two tails are observed in the scatter plot for CO above ~140 ppbv. It was thought that this was most likely a result of higher than average errors in the input parameters causing an increase in the influence of the *a priori* in the UoE retrieval. This was investigated further by looking at the equivalent correlation plots for retrievals over ocean and land surfaces separately (Figure 5.12). As retrievals of the AIRS L2 parameters are more challenging over land surfaces, the errors over land are likely to be higher and the UoE retrieval more influenced by the *a priori*. Consequently it is reasonable to expect that the tail of the distribution below the 1:1 equivalence line at high CO concentrations is largely due to higher errors in retrievals over land. Comparison of Figure 5.12b and Figure 5.12d illustrates this point quite clearly, with distinct distributions in the ocean and land surface retrievals. Although divergence in the distributions are not so apparent at the 700 hPa (Figure 5.10a) and 350 hPa (Figure 5.10c), distinct distributions are observed when retrievals over ocean and land surfaces are considered separately (Figure 5.12a, c, d, and f). At all altitudes the correlation between the UoE and MOPITT retrievals is higher for ocean regions than for land areas (given numerically in Table 5.3), with the UoE retrievals tending away from the MOPITT retrievals and towards the *a priori* when MOPITT CO concentrations are high. This departure from the 1:1 equivalence line is most apparent at the 700 hPa level for retrievals over land, where the degree of correlation between the two instruments is only 0.66. At this level the sensitivity of AIRS to CO is lower, resulting in a stronger dependence on the prior and (CO at other levels) than at the 500 and 350 hPa levels. This is further illustrated by the mean UoE and MOPITT averaging kernels for the ocean and land regions (Figure 5.13) where the UoE averaging kernel at 700 hPa has significantly different shape and peaks at a higher altitude than the equivalent MOPITT averaging kernel.

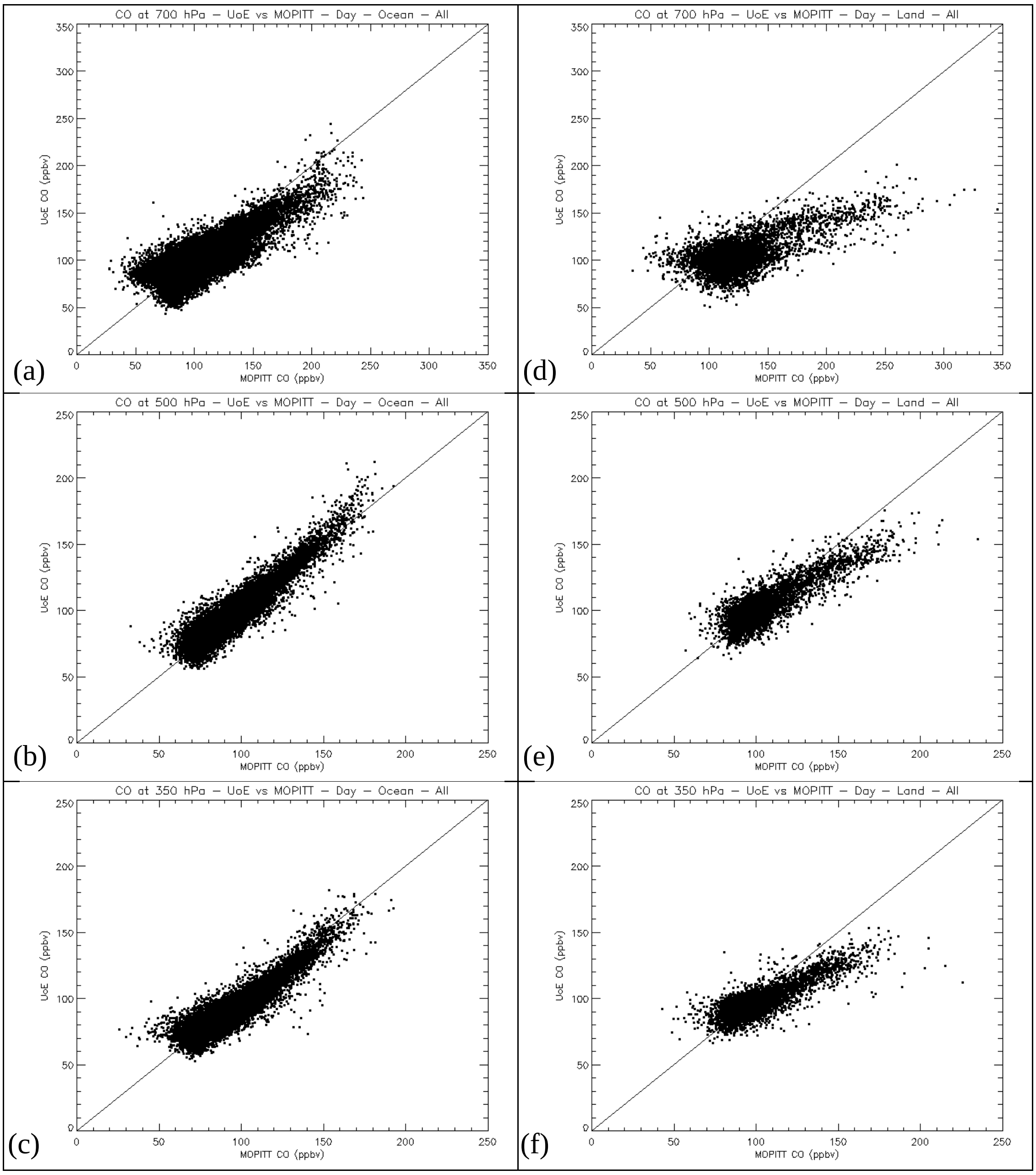

Figure 5.12 Correlation of CO observations between UoE and MOPITT retrievals with ocean (a-c) and land (d-f) regions considered separately. CO retrievals are compared for October 2006 at pressure levels of 700 hPa (a,d), 500 hPa (b,e), and 350 hPa (c,f).

Pressure Level (hPa)	UoE vs MOPITT All Surfaces		UoE vs MOPITT Ocean		UoE vs MOPITT Land	
	R	**Bias**	**R**	**Bias**	**R**	**Bias**
350	0.89	-3.9	0.91	-4.0	0.83	-4.1
500	0.91	0.8	0.93	1.4	0.85	-2.3
700	0.75	-8.5	0.79	-5.1	0.66	-22.1

Table 5.3 Correlation coefficients and biases (ppbv) for comparisons of UoE and MOPITT for retrievals over ocean and land surfaces. Coefficients and biases calculated for monthly mean CO concentrations over the full globe for October 2006.

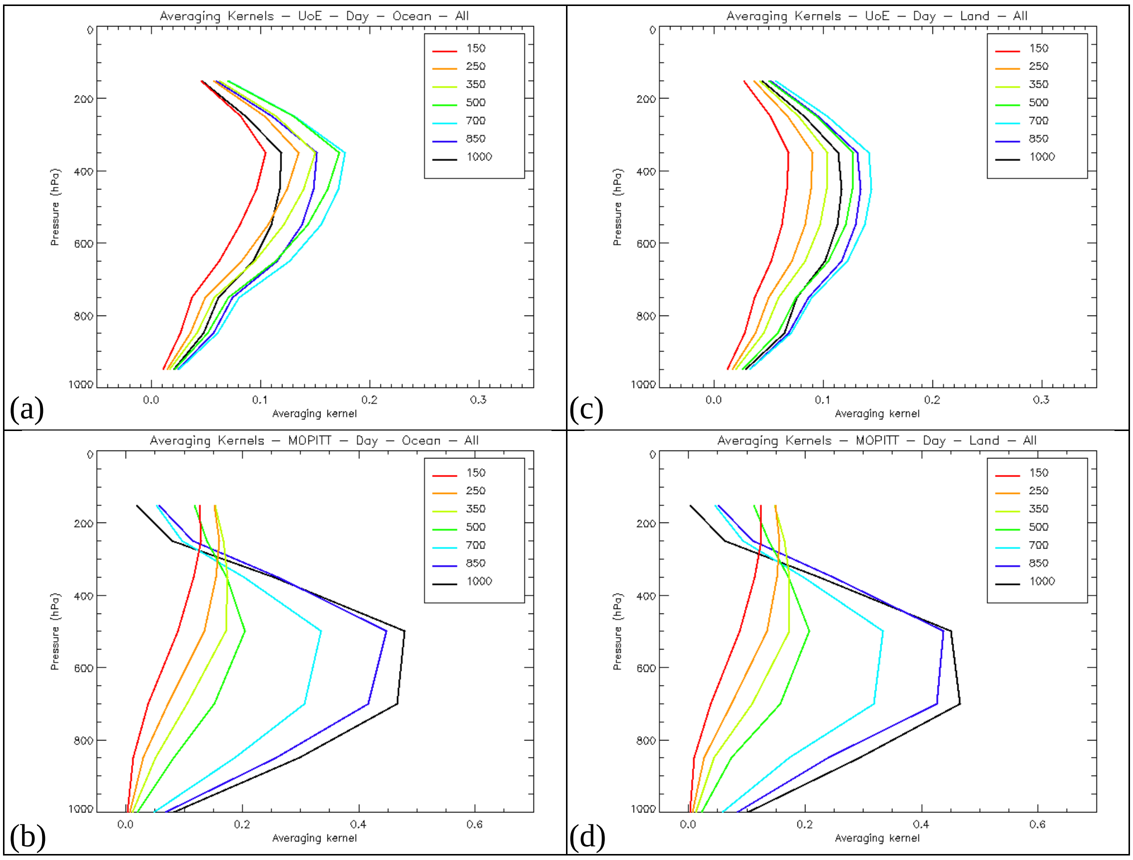

Figure 5.13 Mean averaging kernels from UoE and MOPITT retrievals over ocean and land regions for October 2006. (a) UoE ocean. (b) MOPITT ocean. (c) UoE land. (d) MOPITT land.

Deeter *et al.* [2003] demonstrated the diurnal variability of the MOPITT averaging kernels (Figure 5.3), with the lower troposphere averaging kernels peaking at higher altitudes for (lower surface temperature) night time retrievals. As the lower troposphere averaging kernels from the UoE daytime retrievals are observed to peak at higher altitudes than the equivalent MOPITT averaging kernels (Figure 5.13), it was thought that the MOPITT and UoE averaging kernels (and CO observations) may be more closely related for night time retrievals. The mean UoE and MOPITT averaging kernels from day time and night time retrievals over land are presented in Figure 5.14. These averaging kernels were calculated for October 2006 using only retrievals where the percentage prior contribution (Eq. 4.2) was < 50%. Some diurnal variation is observed in the UoE retrievals, with all the averaging kernels from night time retrievals exhibiting a more distinct peak at higher altitudes and smaller contributions at lower altitudes. A similar effect is also seen in the MOPITT averaging kernel at 700 hPa, which follows the behaviour demonstrated by Deeter *et* *al.* [2003] (Figure 5.3). In terms of the shape of the averaging kernels and the altitude at which they peak, the two instruments are more similar in their sensitivity to CO at 700 hPa for night time retrievals. At 350 and 500 hPa there is little relative difference between the averaging kernels for daytime and night time retrievals.

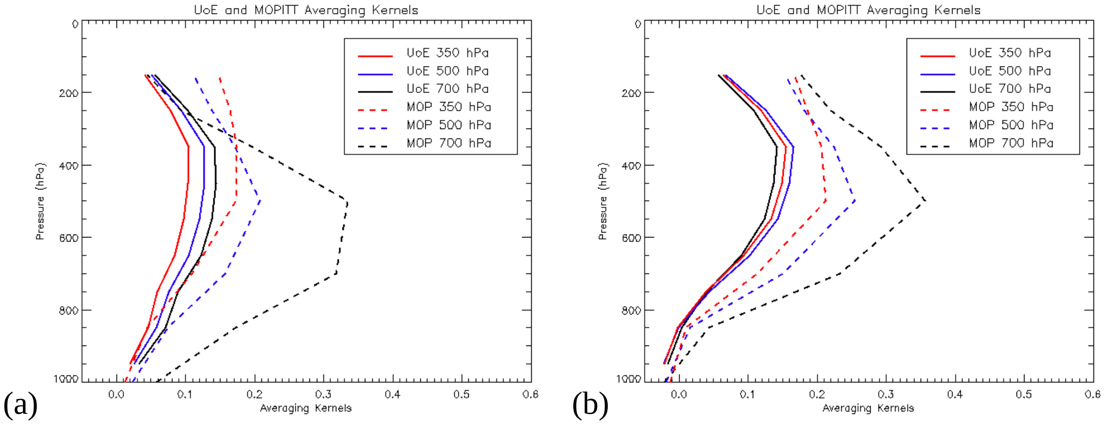

Figure 5.14 Comparison of UoE and MOPITT averaging kernels at 700, 500 and 350 hPa, for (a) daytime and (b) night time retrievals over land.

Direct comparisons of the CO concentrations from the two instruments, for night time retrievals, are shown in Figure 5.15. These are equivalent to the results of Figure 5.12 for day time retrievals. The correlation coefficients corresponding to both day time and night time retrievals are given in Table 5.4, and indicate little difference in the level of agreement between day and night time retrievals at 500 and 350 hPa. However, there is considerable improvement in the correlation (and bias) between the instruments at 700 hPa, for the night time retrievals (Table 5.4). This agrees with the expectations from Figure 5.14, where the 700 hPa averaging kernels are shown to be more similar for night time retrievals. Another point to note is that the relationship between UoE and MOPITT CO observations is closer to a 1:1 agreement at all levels, for the night time retrievals (Figure 5.15). At 700 hPa this is due to the reduction in sensitivity of MOPITT to CO at this level, giving it sensitivity closer to that of AIRS (Figure 5.14). However, at 500 and 350 hPa, where there is less relative difference between the averaging kernels for day and night time retrievals, this improvement in agreement may be due to lower errors in the AIRS L2 products used in the UoE retrieval at night, resulting in less dependence on the prior.

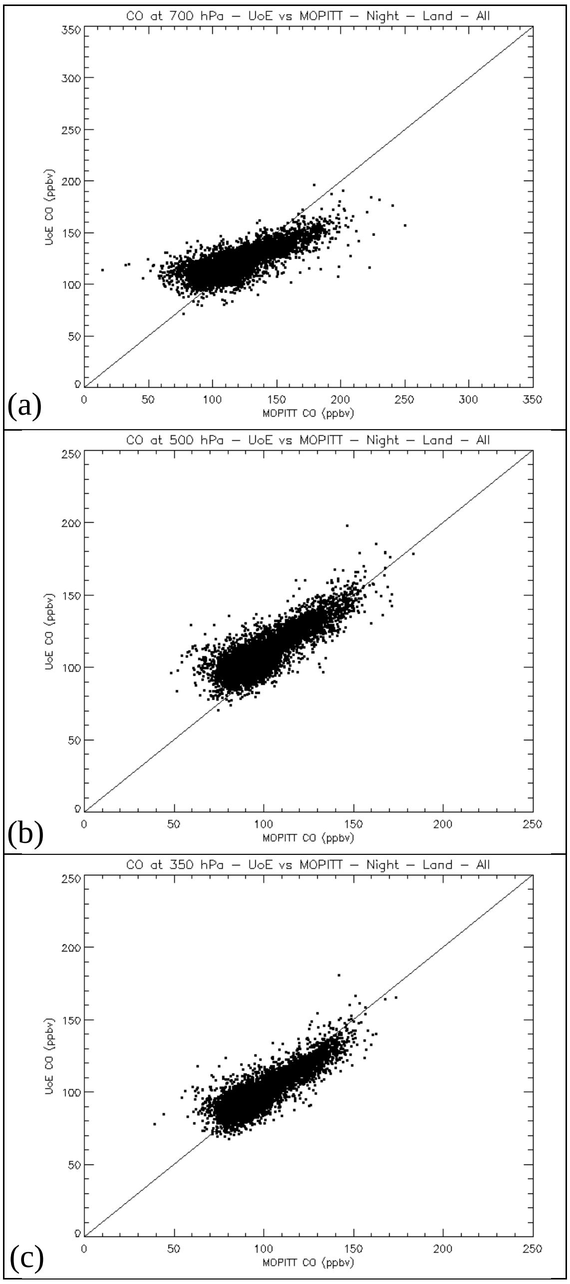

Figure 5.15 Correlation of UoE and MOPITT CO retrievals on profile levels for night time retrievals over land. CO retrievals are compared for October 2006 at pressure levels of (a) 700 hPa (b), 500 hPa, and (c) 350 hPa.

Pressure Level (hPa)	**UoE vs MOPITT Land - Day**		**UoE vs MOPITT Land - Night**	
	R	**Bias**	**R**	**Bias**
350	0.83	-4.3	0.86	0.3
500	0.85	-2.3	0.83	8.9
700	0.66	-22.1	0.76	3.2

Table 5.4 Correlation coefficients and biases (ppbv) for comparisons of UoE and MOPITT CO observations for daytime and night time retrievals over land. CO retrievals are compared for October 2006 at pressure levels. These values correspond to the results presented in Figure 5.12 and Figure 5.15.

5.2.5. Monthly Averaged CO - CO Errors

As discussed in Chapter 2 an important feature of the MAP retrieval scheme is its inherent information about retrieval errors. The UoE retrieval errors, derived from the diagonal elements of the posterior covariance matrix, $\hat{\mathbf{S}}$ (Eq. 2.8), were calculated and averaged for each month as for the CO concentrations (Figure 5.16). These were compared to the retrieval errors from the AIRS v4 product (Figure 5.17).

In the AIRS v4 product, there is little variation in the retrieval error across profile levels, with typical errors of about 20% at all levels. As AIRS is not equally sensitive to CO at all altitudes, with decreasing sensitivity away from the mid-troposphere, the retrieval errors would be expected to reflect this and show more variation through the profile. Such behaviour is observed in the UoE retrieval with error estimates ranging from ~20% at 700 hPa to ~10% at 500 hPa, where the AIRS channels are more sensitive to CO. At 350 hPa, where the sensitivity of AIRS lies somewhere between that at 700 and 500 hPa, the retrieval errors also lie between those at 700 and 500 hPa. From this comparison it can be seen that the optimal estimation techniques used in the UoE retrieval provide a more plausible representation of the errors than the AIRS v4 algorithm.

Looking more closely at the UoE retrievals at 500 hPa Figure 5.16b reveals some trends in the spatial distribution of the errors. Although higher information content is expected in the retrievals over land, larger errors are observed over land regions. The most probable reason for this is larger errors in the AIRS L2 products used in the UoE retrieval. Any increase in these errors will be propagated through the retrieval scheme resulting on an increased contribution from the prior and higher error estimates. The second feature to note is higher retrieval errors over sea regions in the mid-latitudes than in the tropics. As higher information content is expected in the tropics, it is reasonable to expect retrievals errors to be lower in the tropics than in mid-latitude regions.

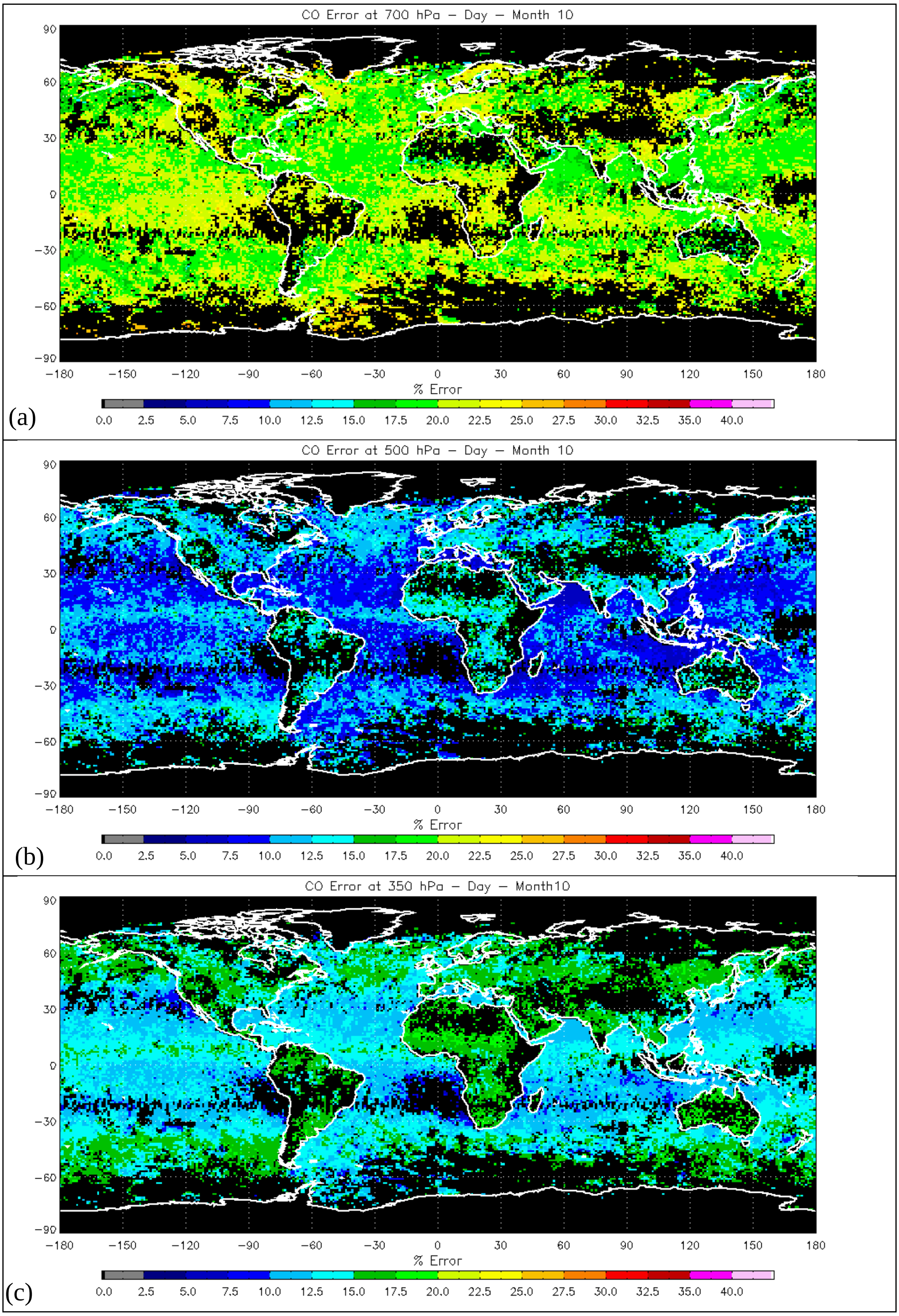

Figure 5.16 UoE retrieval errors for monthly average daytime CO concentration for October 2006. (a) 700 hPa, (b) 500 hPa, and (c) 350 hPa.

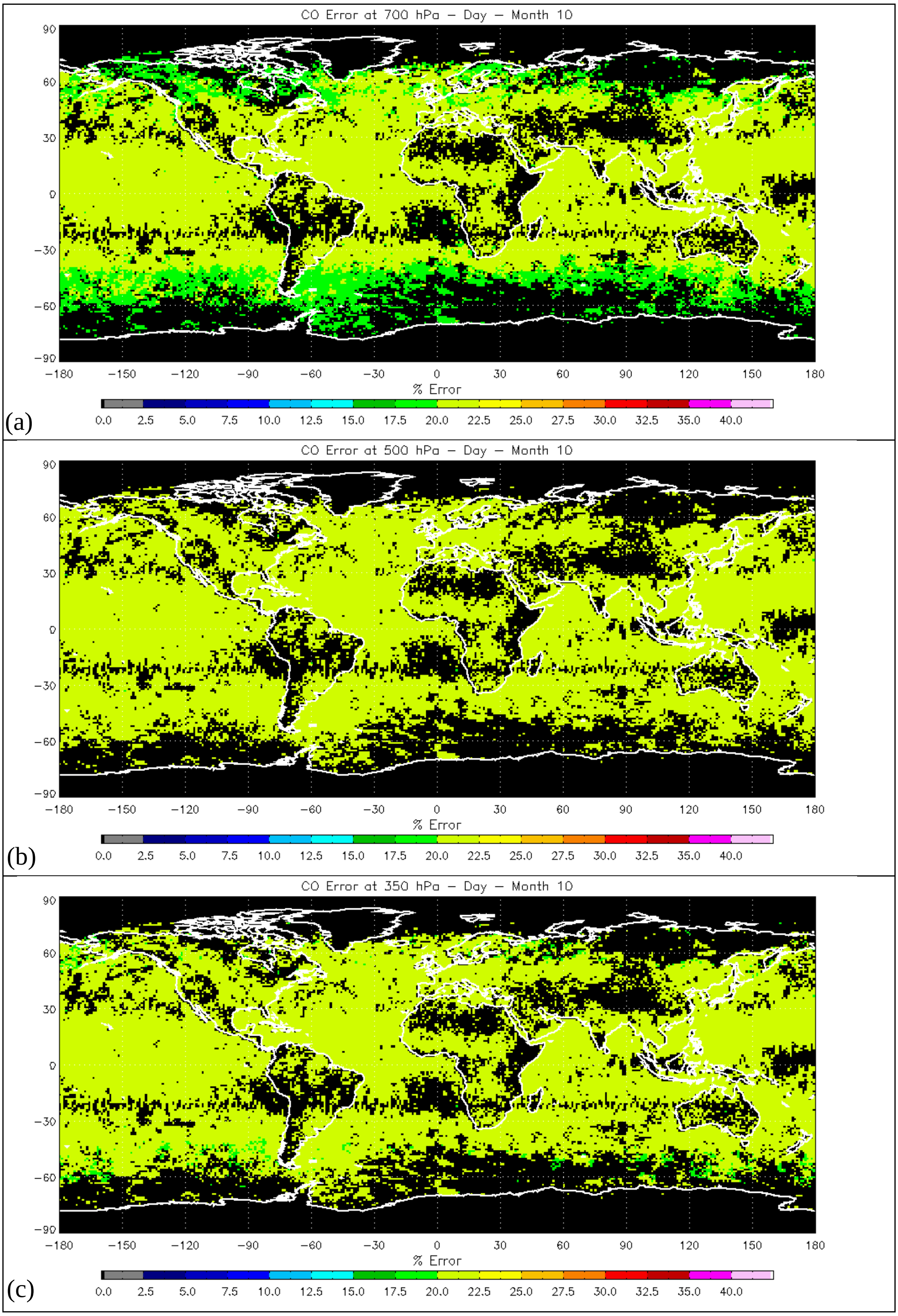

Figure 5.17 AIRS v4 retrieval errors for monthly average daytime CO concentration for October 2006. (a) 700 hPa, (b) 500 hPa, and (c) 350 hPa.

5.2.6. Monthly Averaged CO - Total Column CO

Total column CO (TCCO) values were derived from the retrieved profiles from the UoE and AIRS v4 methods, and were compared to those from MOPITT. Correlation coefficients for both AIRS methods are high (~0.85) but global maps of TCCO (Figure 5.18) show that MOPITT provides significantly higher estimates of the total column than either of the AIRS methods. As suggested in §5.2.4 this is due the greater sensitivity of MOPITT to CO in the lower troposphere, where higher CO concentrations and variability can be expected as a consequence of closer proximity to the CO sources. Figure 5.19a highlights this point, showing that the UoE and MOPITT TCCO retrievals diverge as TCCO increases. As MOPITT is more sensitive at lower levels, increases in the CO concentration in the lower troposphere will be better captured by MOPITT. Also contributing to the divergence is the increased influence from the prior in the UoE retrieval as the altitude drops.

The AIRS v4 product displays similar behaviour for high values of TCCO but also appears to overestimate TCCO relative to MOPITT for low CO concentrations (Figure 5.19b). These two features suggest the AIRS v4 algorithm probably suffers from significant influence from the “first guess” profile. Similar distributions are observed for UoE-MOPITT and AIRS-MOPITT TCCO differences in Figure 5.19c. From the results of §5.2.4 the UoE-MOPITT distribution is as expected. However the distribution for AIRS-MOPITT is the opposite of that observed in §5.2.4. This is because the total column values are dominated by the CO concentrations in the lowest levels of the profiles (<700 hPa) and at these levels the AIRS CO is generally lower than the MOPITT CO.

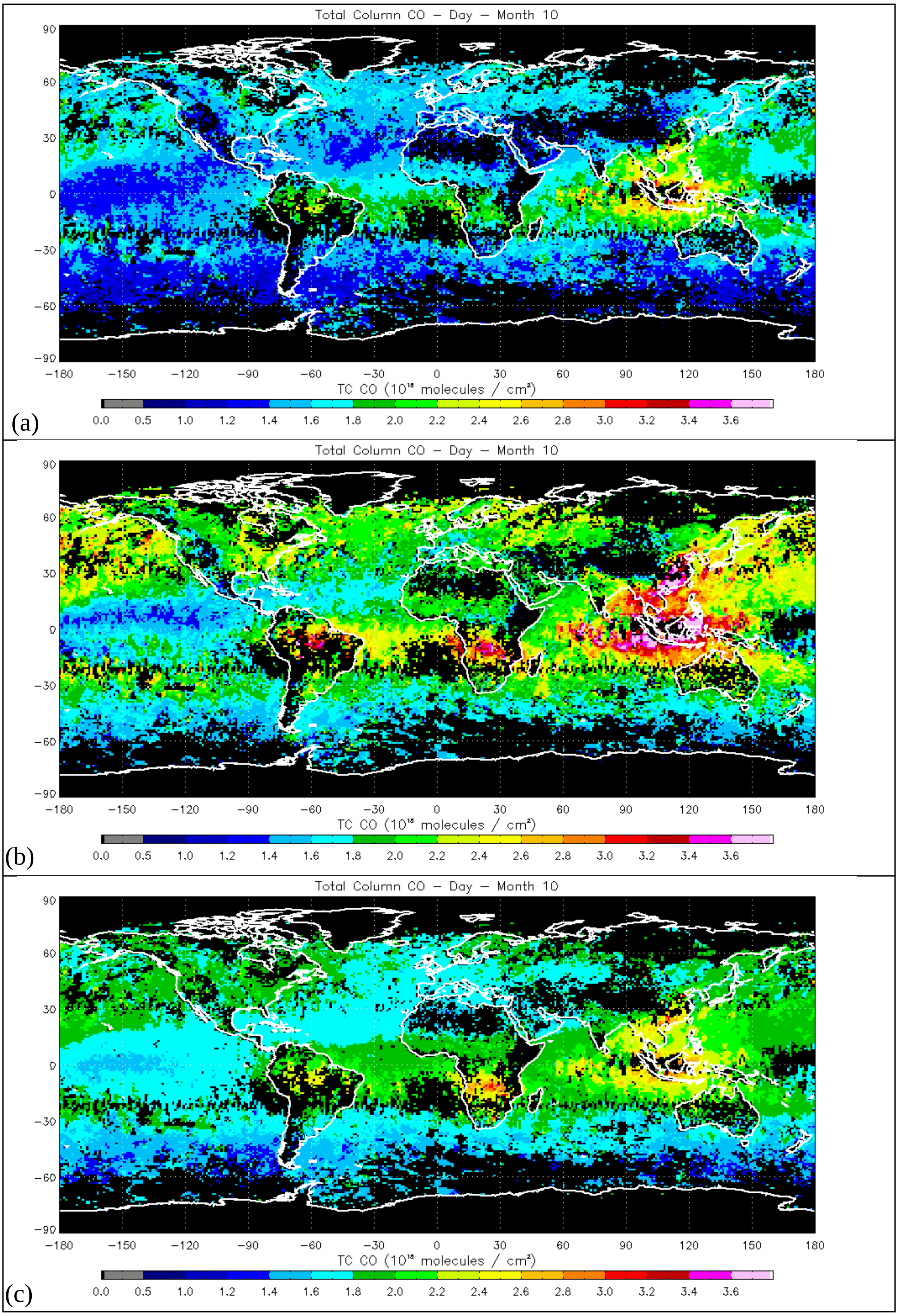

Figure 5.18 Monthly average daytime total column CO concentration for October 2006. (a) UoE, (b) MOPITT, and (c) AIRS v4. UoE and MOPITT data has been filtered to exclude data with % prior > 50 % at 500 hPa

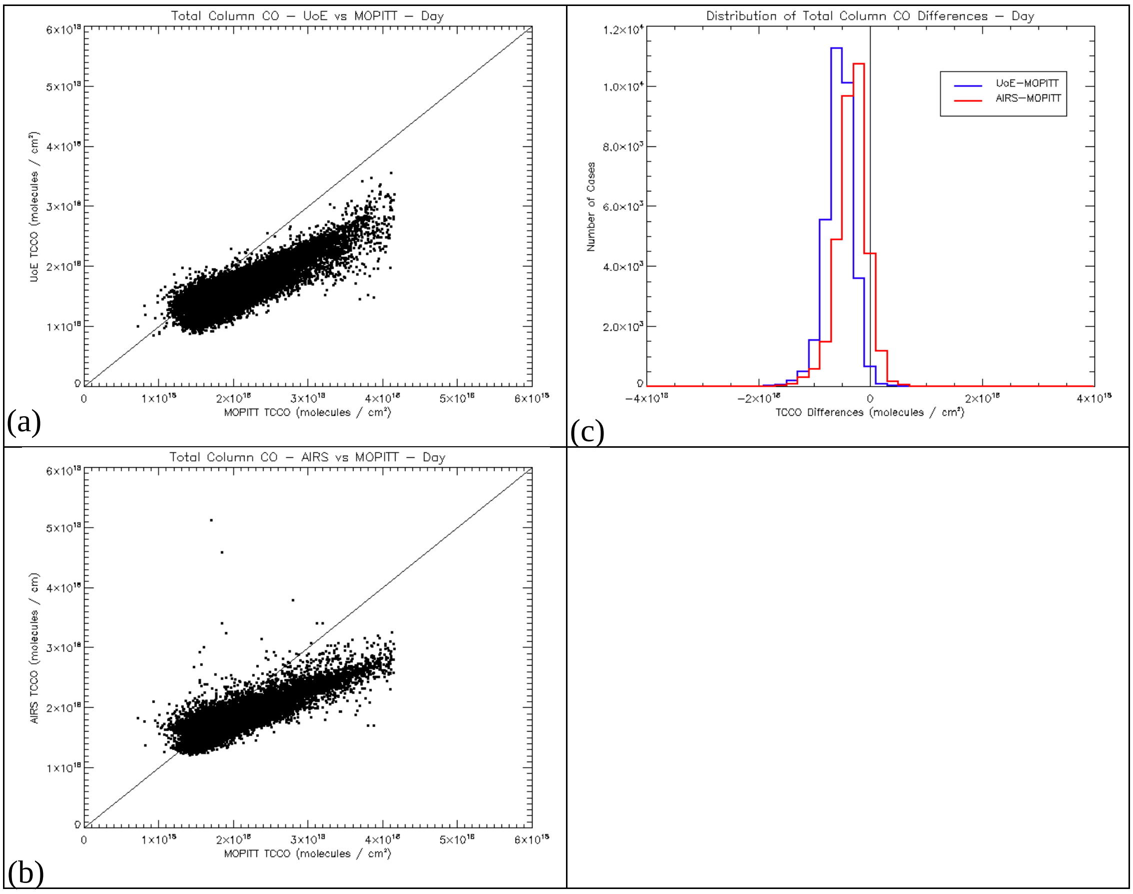

Figure 5.19 Correlation and distribution of total column CO across observing systems. (a) UoE vs MOPITT, (b) AIRS v4 vs MOPITT, and (c) distribution of total column CO differences between observing systems. The histogram in (c) was calculated using a bin size of 5 ppbv.

5.2.7. Monthly Averaged CO - Degrees of Freedom of Signal

The number of degrees of freedom of the signal, d_s, was calculated for the UoE retrievals using Eq. 2.15 and compared to that from the MOPITT product. No equivalent data product or the means to produce such a diagnostic is provided in the AIRS v4 product. Maps of d_s are shown for daytime and night-time retrievals for UoE (Figure 5.20) and MOPITT (Figure 5.21). It is quite clear from these maps that there are generally more pieces of independent information about the CO profile contained in the MOPITT measurements than those from AIRS. The mean values of d_s for each map are given in Table 5.5. This additional information present in the MOPITT observations is probably largely due to its higher sensitivity at lower altitudes, illustrated by the averaging kernels in Figure 5.13.

	UoE	**MOPITT**
Day	0.86	1.28
Night	0.83	1.17

Table 5.5 Monthly mean (for October 2006) number of degrees of freedom of signal calculated for the UoE and MOPITT CO retrievals.

As well as typically providing higher d_s, MOPITT also returns a larger range of d_s values, shown clearly in the histograms of d_s in Figure 5.22. There is also considerably diurnal variation in the MOPITT d_s over land that is not present in the UoE data. Both of these features support the case that MOPITT is more strongly influenced by conditions at lower troposphere and surface levels than AIRS, as the conditions at these levels are more variable than at higher altitudes. The lack of diurnal variation over land in the UoE retrieval, and the lower values of d_s over land than ocean during the daytime, is in disagreement with the expected result (higher values are expected with higher thermal contrast between surface and atmosphere). The reasons for this have not been fully investigated but it is thought that it is due to increased noise in the retrieval, arising from higher errors in the AIRS L2 products used in the retrievals.

The global maps in Figure 5.21 also show quite a clear trend in d_s with latitude, with d_s decreasing towards the poles. Such a trend is not so obvious in d_s from UoE but is present to some degree over the oceans. Again this difference is probably due to AIRS being less sensitive to conditions at lower altitudes.

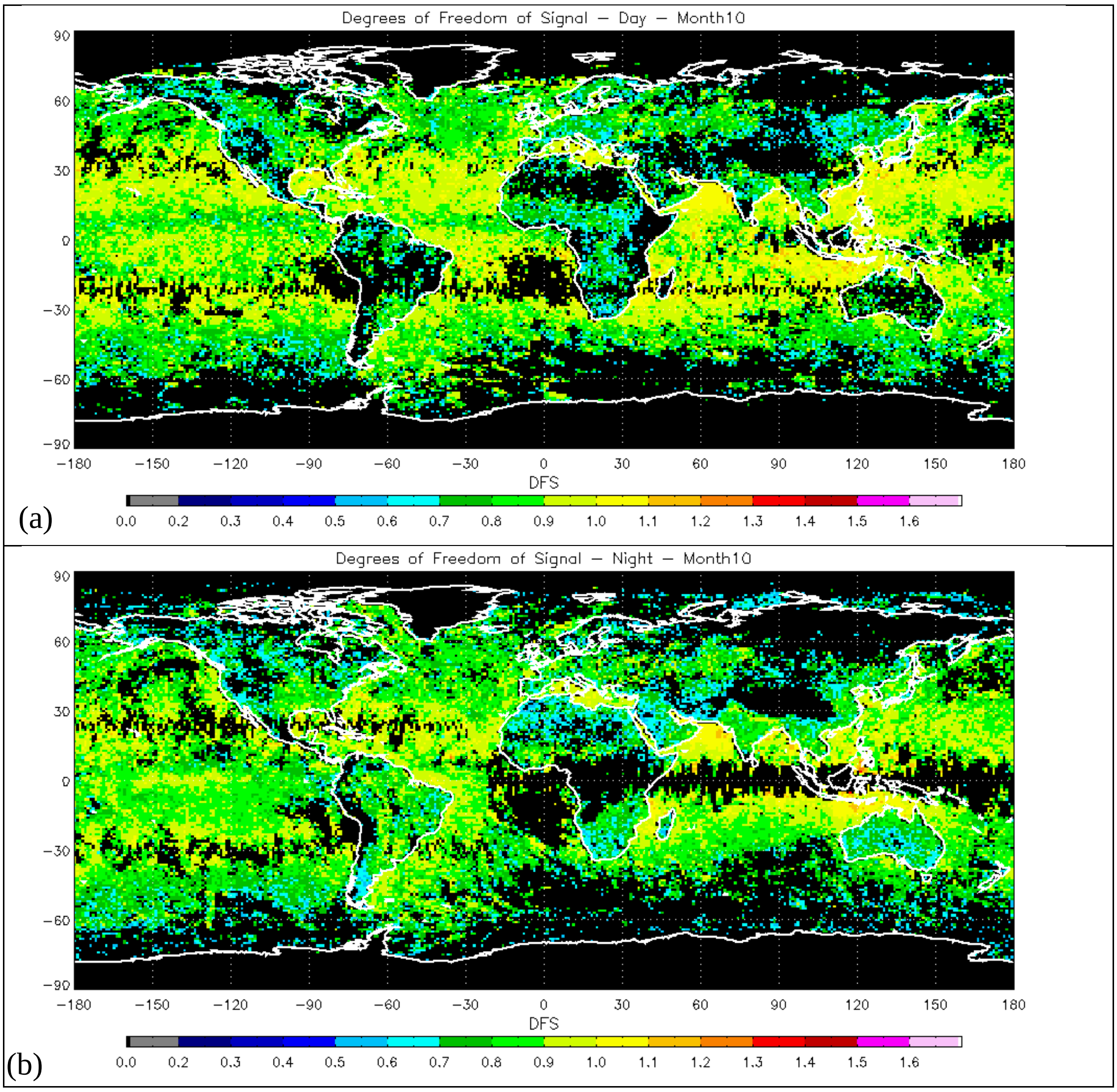

Figure 5.20 Monthly average number of degrees of freedom of signal from UoE retrievals for October 2006, (a) day, (b) night.

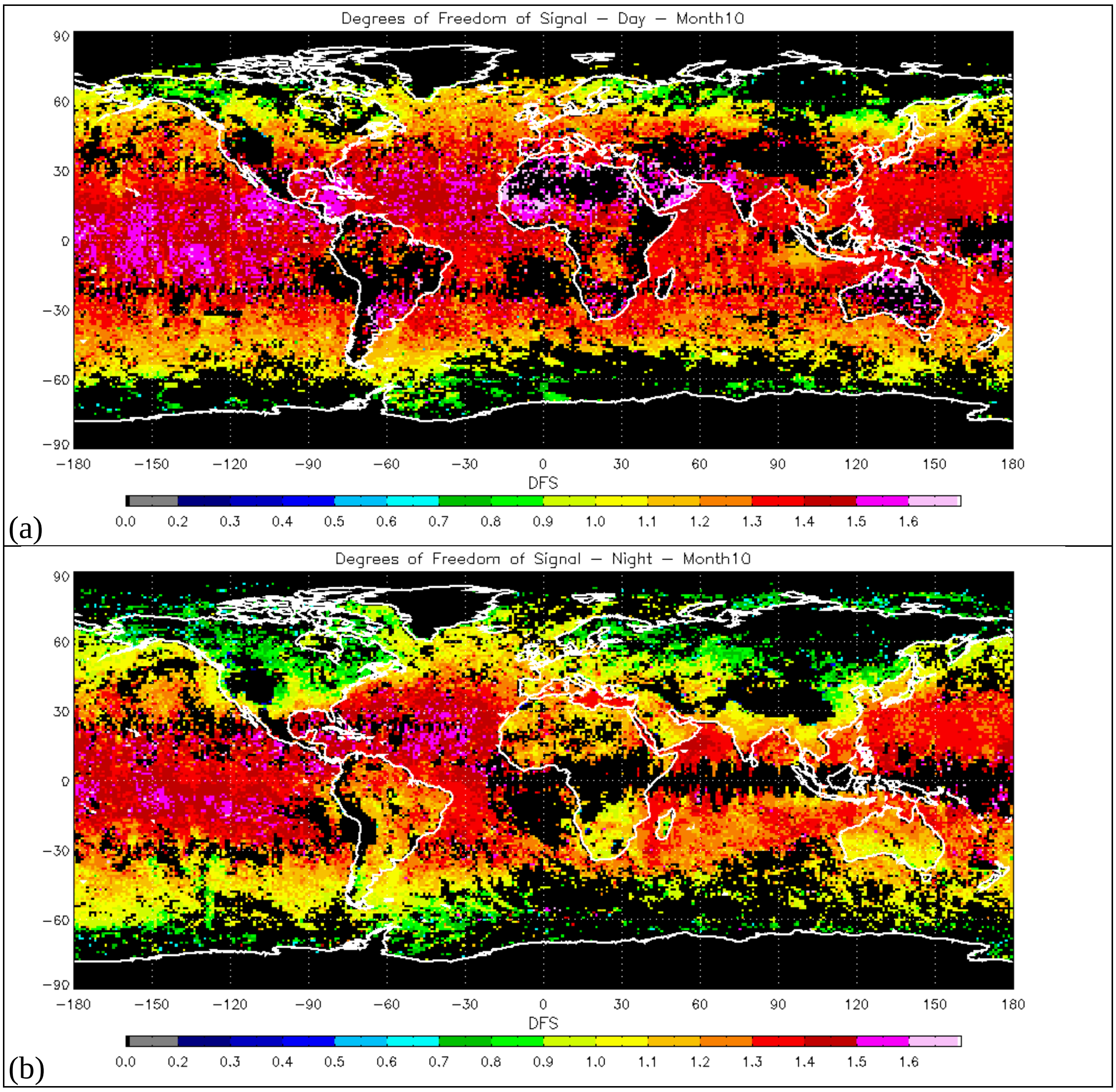

Figure 5.21 Monthly average number of degrees of freedom of signal from MOPITT retrievals for October 2006, (a) day, (b) night.

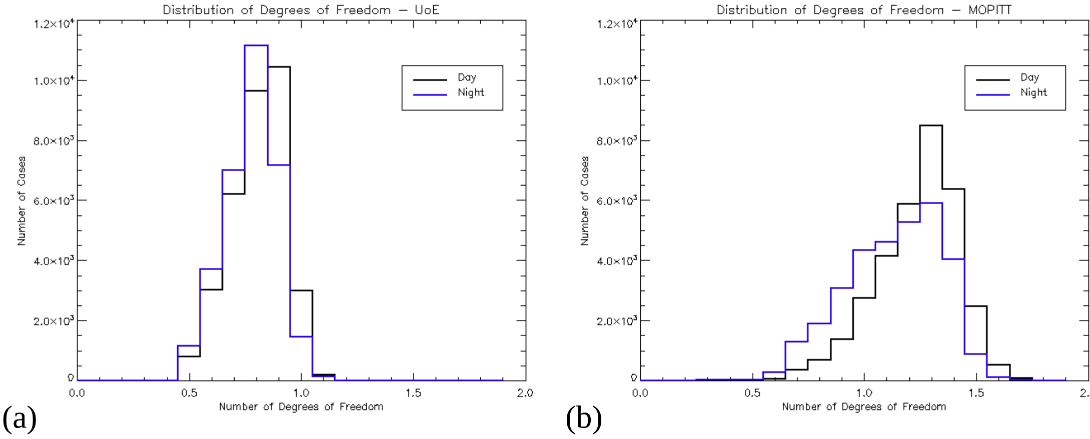

Figure 5.22 Distribution of the number of degrees of freedom of signal for (a) UoE, and (b) MOPITT. Histograms were calculated from the monthly mean data for October 2006, using a bin size of 1.0 degrees of freedom.

5.3. Summary

In this chapter, results from a comprehensive comparison of the UoE, AIRS v4, and MOPITT CO products have been presented. This work has improved our understanding of the UoE CO product and highlighted a number of differences between the UoE product and those of MOPITT and the AIRS v4 algorithm.

An important advantage of the AIRS CO products over that from MOPITT, is superior spatial coverage. AIRS provides near-global coverage on a daily basis, while MOPITT requires about three days for global coverage. AIRS is also able to perform retrievals in the presence of significant amounts of cloud cover, which further contributes to its higher coverage, relative to MOPITT. The superior coverage of the AIRS instrument is a benefit for studies of CO transport and source variability.

Another important contrast between AIRS and MOPITT, highlighted in this chapter, is their differing sensitivity to CO at different altitudes. The two instruments are shown to share similar sensitivity to CO in the mid-troposphere, and are well correlated at this level. However, in the lower troposphere, inter-instrument correlations are lower and MOPITT observes higher CO concentrations. This is due to MOPITT being more sensitive than AIRS at lower levels. The effect of this is particularly marked when total column CO concentrations are considered, with large differences observed between AIRS and MOPITT. As a large proportion of CO sources are at the surface, a lack of sensitivity to CO in the lower troposphere will result in an underestimation of total column CO. Such an underestimation is seen in the AIRS data relative to MOPITT and suggests that AIRS is not well suited to studies of CO in the lower troposphere.

As well as being more sensitive to CO in the lower troposphere, MOPITT is also able to better distinguish between CO at different altitudes. This is illustrated in the analysis of the number of degrees of freedom of signal, d_s. where MOPITT is shown to provide ~1.3 pieces of independent information compared to 0.85 from AIRS. This indicates that MOPITT has greater potential for looking at the vertical structure of CO in the atmosphere. Another point of note from the analysis of d_s, is the fact that AIRS has lower values over land than over ocean regions for daytime retrievals, and that there is no clear diurnal variation over land. This does not agree with expectations and is thought to be due to higher errors in the AIRS L2 products over land resulting in an increased contribution from the prior.

Some differences between the UoE and AIRS v4 products are also shown in this chapter. The first is a positive bias relative to both the MOPITT and UoE retrievals, which is thought to be partially due to the influence of the “first guess” CO profile on the AIRS v4 retrieval. Secondly, the AIRS v4 error estimates are shown to have little variation with altitude, whereas the UoE error estimates vary with altitude according to the sensitivity of CO. This more plausible representation of the retrieval errors is an important advantage offered by the UoE optimal estimation retrieval.

Chapter 6. Time Series Analysis

6.1. Introduction

The work of Chapter 5 demonstrated good agreement between the UoE and MOPITT monthly average CO products at mid-troposphere levels. In order to further understand the behaviour of the retrieval products, analysis of the annual time series was carried out. Time series for 2006 were calculated from daily averages for latitude bands and a number of regions of interest (Table 6.1). Each time series was then smoothed using a 3-day moving average to remove some of the noise from the signal. This smoothing was applied primarily to remove noise from the MOPITT time series, as the better spatial coverage of AIRS results in more consistent inter-day CO retrievals for each region. The results are outlined in the following sections.

6.2. Latitudinal Effects

Time series were generated for six latitude bands, covering the high (±90 to ±66.5), middle (±66.5 to ±23.5), and tropical (±23.5 to 0) latitudes, for each hemisphere. The time series of CO at 500 hPa for each of these latitude regions are shown in Figure 6.1. Very good agreement between UoE and MOPITT is observed for tropical latitudes, in terms of both trends and the magnitude of CO. The AIRS v4 CO product also captures the same CO trends but consistently estimates the CO concentration to be ~10-15 ppbv higher than that observed by MOPITT and UoE. A similar result is seen in the mid-latitudes, with a reduction in the positive bias in the AIRS observations of ~5 ppbv. For the case of the high Northern latitude region, there is broad agreement in terms of the trends in CO but somewhat more variability in the magnitude of differences in CO concentrations. In the equivalent Southern hemisphere region there is less agreement between MOPITT and the two AIRS retrievals, with significantly different trends over the first 100 days of the time series. This poorer agreement in the Southern high latitudes is most likely due to a combination of the low CO concentrations and the low temperatures and lack of thermal contrast reducing the quality of the retrievals. Although the surface and atmospheric conditions may be similar in both hemispheres, the significantly lower CO concentrations in the Southern hemisphere make the retrieval more difficult.

Seasonal trends in CO can be seen in the different latitude bands in Figure 6.1. In the Northern hemisphere mid-latitudes, CO concentrations are observed to peak in the early spring before falling over the summer months. This is due to a combination of increased winter time emissions from industrial/urban emissions followed by an increase in OH concentrations, resulting from higher levels of solar illumination during the summer months. In the Southern hemisphere mid-latitude region, CO concentrations are considerably lower, due to the lower industrial/urban emissions. The peak in CO around September/October is largely due to CO transport from biomass burning in South America, South Africa, Indonesia and Northern Australia.

To further investigate the relative behaviour of the three retrieval schemes with latitude, time series were calculated for 10° latitude bins from 90° N to 90° S. The coefficients of correlation between the time series from the three retrievals were calculated and the results presented in Figure 6.2. As suggested by Figure 6.1 excellent correlation between UoE and MOPITT is observed in tropical and mid-latitude regions, with correlation reducing at high latitudes, particularly in the Southern hemisphere. The correlation between AIRS and MOPITT is also very high for much of the tropical and mid-latitude region, but is somewhat lower in the Southern mid-latitudes. From the work of Chapter 5 this is probably because the AIRS v4 retrieval does not perform so well in regions of low CO concentrations

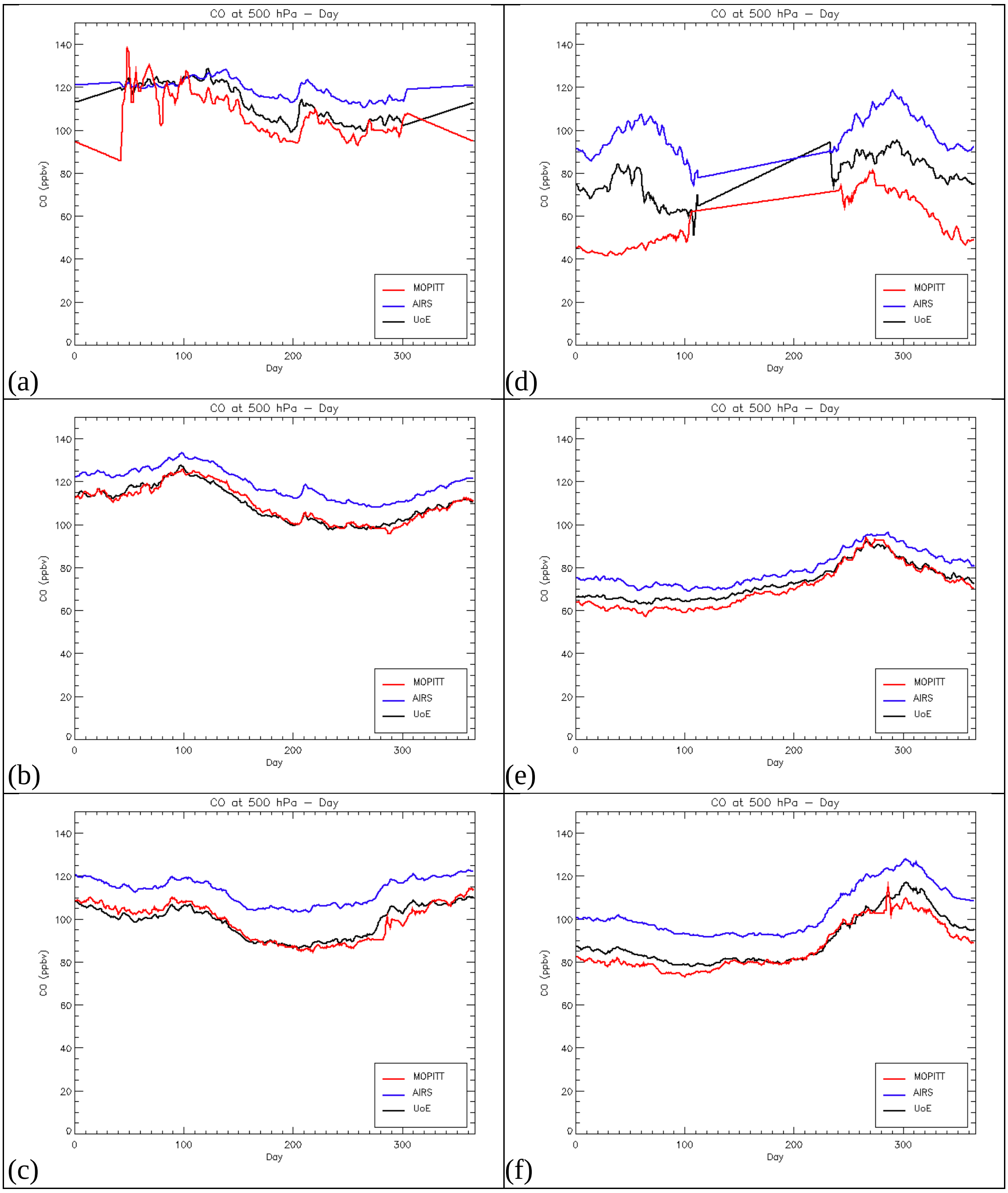

Figure 6.1 Time series of CO at 500 hPa for latitude regions. (a) 90° N to 66.5° N. (b) 66.5° N to 23.5° N. (c) 23.5° N to 0°. (d) 90° S to 66.5° S. (e) 66.5° S to 23.5° S. (f) 23.5° S to 0°.

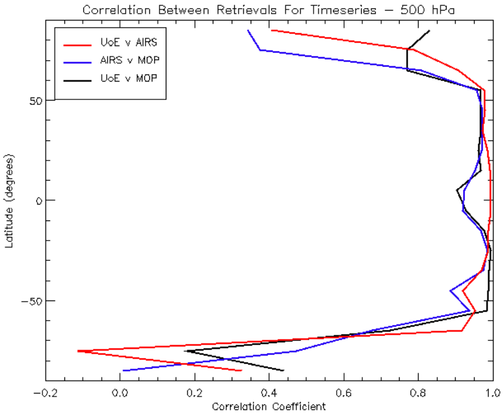

Figure 6.2 Correlation between retrieval methods for different latitudes.

6.3. Time Series on Profile Levels

The Northern hemisphere tropical latitude region was used to investigate the time series of CO at different profile levels, to try to illustrate further the relative behaviour of the three retrieval schemes. These time series are shown in Figure 6.3 along with the correlation between instruments across the profile levels. The best agreement in terms of the magnitude of CO is observed at 500 hPa, where high correlation between the retrievals is also observed. Correlation is high in the mid to upper troposphere but decreases towards the lower troposphere. The cause of this decrease in correlation is clearly illustrated in the time series of CO at 850 hPa (Figure 6.3a). At this level a much larger range of CO concentrations is observed by MOPITT due to its greater sensitivity to CO at lower levels of the atmosphere (§5.2.4). This results in far more pronounced trends in the CO concentration from MOPITT over the course of the year. Comparison of the time series at 850 hPa (Figure 6.3a) and 500 hPa (Figure 6.3c) reveals that the trends in CO concentration from UoE at 850 hPa are weaker versions of those at the 500 hPa level, where the UoE retrieval is more sensitive to CO. As highlighted in §5.2.4**,** AIRS retrievals in the lower troposphere are dominated by CO concentrations at higher altitudes and a contribution from the prior. It is this increased dependence on the mid-troposphere CO concentration in the AIRS instrument that results in the poorer agreement with MOPITT at lower troposphere levels.

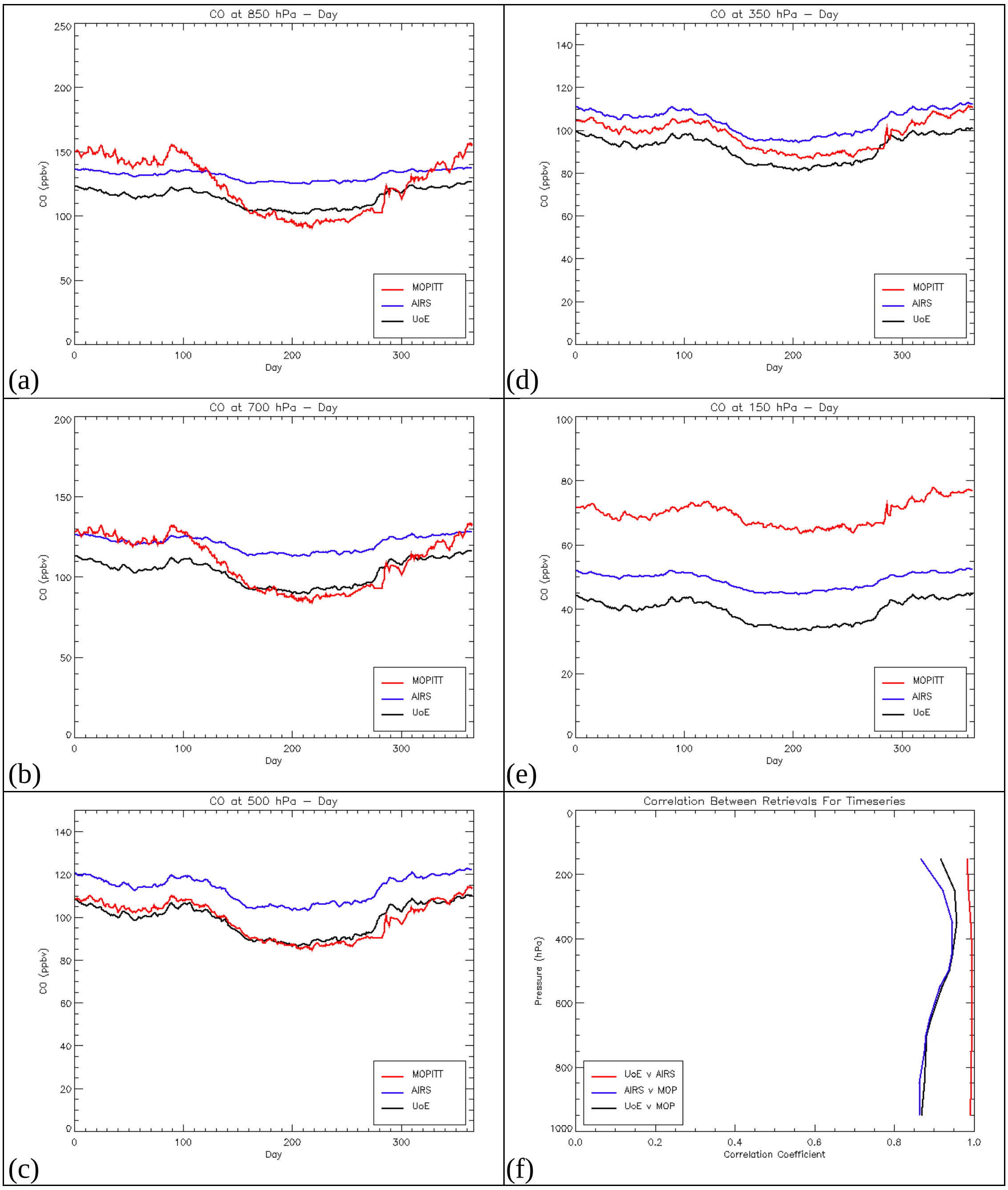

Figure 6.3 Time series of CO at different altitudes for the Northern hemisphere tropics region (23.5° N to 0°). (a) CO at 850 hPa. (b) CO at 700 hPa. (c) CO at 500 hPa. (d) CO at 350 hPa. (e) CO at 150 hPa. (f) Correlation between retrievals across profile levels.

In order to better illustrate the performance of the UoE and MOPITT retrievals at different altitudes the degree of contribution from the *a priori* was investigated. Annual mean values of the percentage contribution from the *a priori* at each level, were calculated at each profile level, for the Northern hemisphere latitude regions of §6.2. Profiles of this percentage *a priori* contribution are shown in Figure 6.4 and highlight a number of things about the retrieval schemes. The first point to note is that the dependence on the *a priori* decreases as latitude moves towards the equator. This is true for both retrieval schemes and is a consequence of higher thermal contrasts in the atmosphere in equatorial regions than at the poles.

Although changes in dependence on the *a priori* with latitude are observed for both instruments, the changes for MOPITT are far more pronounced. While the shape of the *a priori* contribution profile remains fairly constant across latitude for UoE retrievals, there is significant change in the equivalent profile for MOPITT. In the high and mid-latitude regions the lowest percentage contribution from the *a priori* occurs at 350 hPa, while in the tropics the minimum occurs at 700 hPa, with a secondary minimum at 350 hPa. This suggests that MOPITT is more sensitive to the atmospheric state than AIRS, with sensitivity to CO at lower altitudes increasing for more tropical atmospheres. This change in sensitivity with latitude was also shown in the analysis of the number of degrees of freedom of the signal in §5.2.7.

Another observation to make about Figure 6.4 is the relative contribution from the *a priori* between the two retrievals. In all cases UoE has less dependence on the *a priori* than MOPITT at the mid-troposphere levels. This is most apparent at higher latitudes and indicates that AIRS may provide more useful mid-troposphere retrievals in these regions. MOPITT however relies less on the *a priori* at both lower and upper troposphere levels, particularly in tropical regions where MOPITT’s dependence on the *a priori* is consistently low across a large range of altitudes (850 to 250 hPa).

As the UoE and MOPITT retrieval schemes use different prior covariance matrices, the significance of these results, comparing the percentage contribution from the prior, is somewhat less clear. The results in Figure 6.4 imply that AIRS is more sensitive at mid-troposphere levels than MOPITT and that AIRS is less sensitive in the lower troposphere. If this is the case then it is reasonable to expect to see higher variability in the UoE time series (relative to MOPITT) at 500 hPa, and lower variability at lower levels. Higher variability is observed in the MOPITT time series for the lower troposphere (Figure 6.3a) but the time series at 500 hPa are very similar (Figure 6.3c). As higher CO variability is expected in the lower troposphere and the difference in the percentage prior contribution between instruments is larger at these levels, it is reasonable that the inter-instrument differences are larger in the lower troposphere. Although the relative sensitivity of the instruments at 500 hPa is less clear, there is confidence in the varying sensitivity with latitude, of the individual instruments.

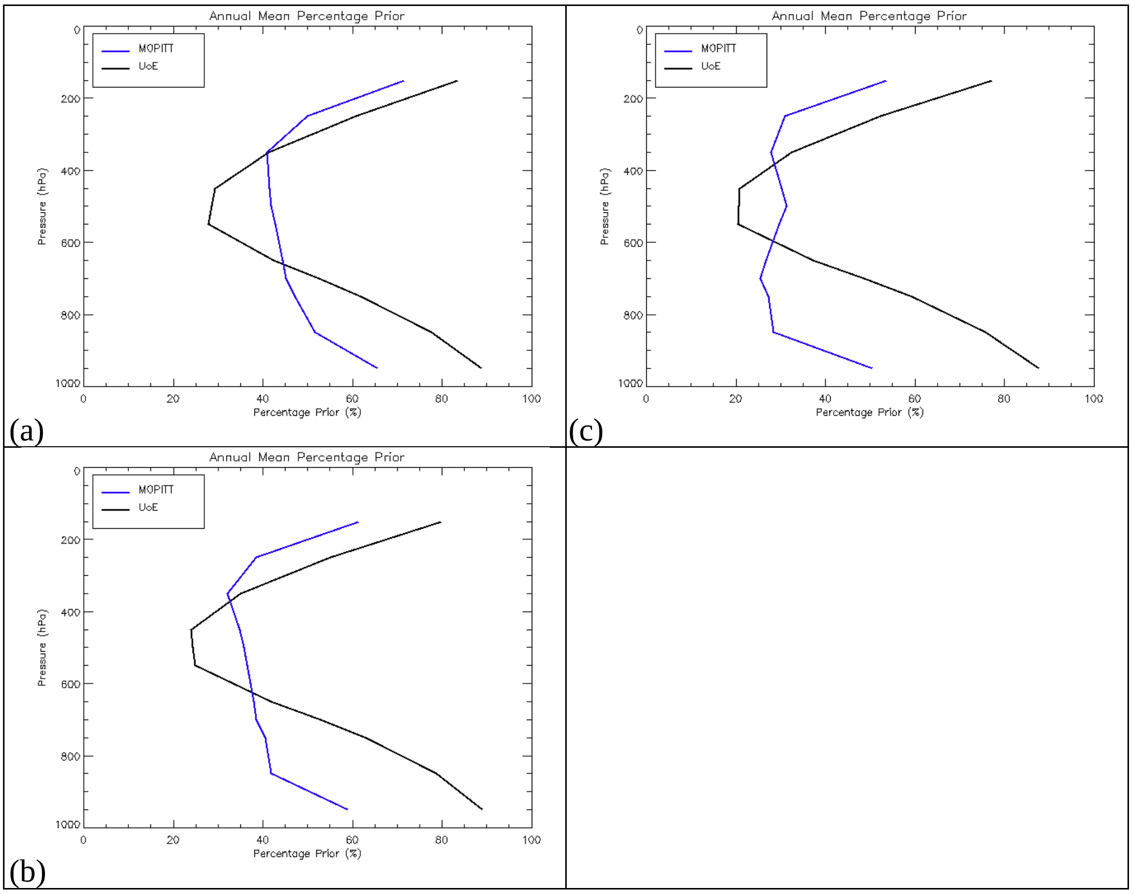

Figure 6.4 Annual mean profiles of percentage contribution from the *a priori* for the latitude regions (a) 90° N to 66.5° N, (b) 66.5° N to 23.5° N, and (c) 23.5° N to 0°.

6.4. Case Study Regions

6.4.1. Selection of Regions

Time series were investigated for a number of regions of interest, selected to demonstrate the ability of the UoE retrieval to detect seasonal trends in CO concentrations. The regions selected are illustrated in Figure 6.5 and their latitude and longitude bounds given in Table 6.1.

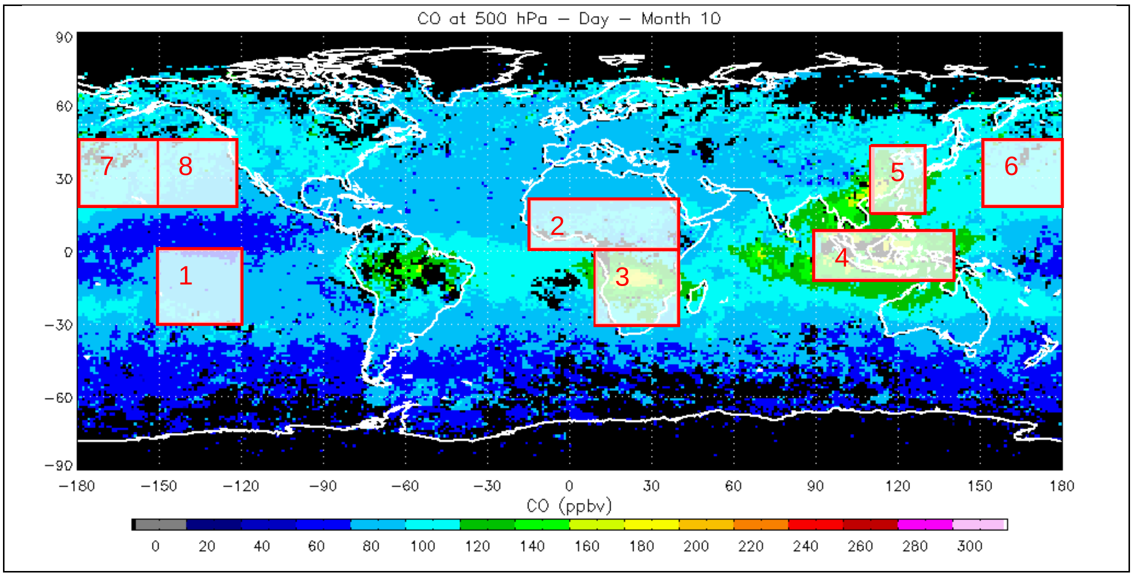

Figure 6.5 Locations of regions of interest for time series analysis. (1) SPC, (2) CAF, (3) SAF, (4) IND, (5) CHI, (6) NPC1, (7) NPC2, (8) NPC3. The latitude and longitude bounds of these regions are given in Table 6.1.

Number	**1**	**2**	**3**	**4**	**5**	**6**	**7**	**8**
Name	SPC	CAF	SAF	IND	CHI	NPC1	NPC2	NPC3
Min. Lon.	-150	-15	10	90	110	150	-180	-150
Max. Lon.	-120	40	40	140	130	180	-150	-120
Min. Lat.	-30	0	-30	-10	20	20	20	20
Max. Lat.	0	20	0	10	45	45	45	45

Table 6.1 Longitude and latitude bounds of the numbered regions of interest shown in Figure 6.5

6.4.2. South Pacific

A region of the South Pacific ocean (SPC) was selected to show the annual CO for an area with no direct CO source from biomass burning or industry, where CO concentrations are expected to be low. The time series for CO at 500 hPa for this region is shown in Figure 6.1. CO is observed to be fairly constant at ~70 ppbv for the first 7 months of the year, before a gradual increase is observed from around August to November, peaking at ~95 ppbv. This increase coincides with the main period of biomass burning in a number of Southern hemisphere regions, such as South Africa, South America and Indonesia [Edwards *et al.*, 2004]. During the southern hemisphere summer, higher levels of solar illumination result in increased concentrations of OH. This allows more CO to be removed from the atmosphere and will contribute to the decrease in CO concentrations after the November maximum.

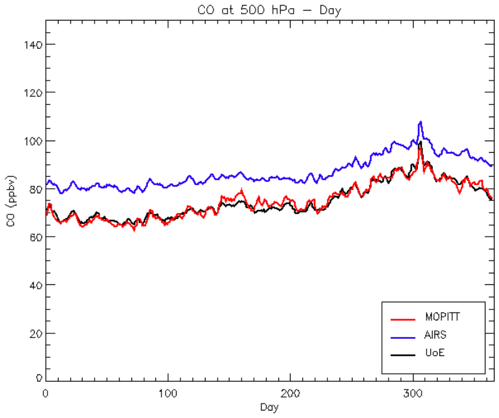

Figure 6.6 Time series of daily mean CO at 500 hPa for the SPC region (with bounds of 30°S, 0°N, 150°W, and 120°W) illustrated in Figure 6.5, for 2006.

6.4.3. Central and Southern Africa

Two regions (CAF and SAF) were selected over Africa to demonstrate the ability of the UoE retrieval to detect seasonal signals in CO from biomass burning. The time series for these regions are shown in Figure 6.7. For the CAF region the peak CO concentrations are observed between December and February, corresponding to the dry season in the region and increased biomass burning [Edwards *et al.*, 2004]. In the SAF region CO peaks during September and October, again coinciding with the dry season in the region and an increase in biomass burning activity.

At 500 hPa all the retrieval schemes capture similar amounts of variability in CO concentration. The same is not true at the 700 hPa level, where the higher sensitivity of MOPITT results in it seeing a considerably larger range of CO than either of the AIRS systems. Although the UoE CO product does not capture such an extensive range of CO concentrations as MOPITT, it does appear to record a somewhat larger range of CO concentrations than the AIRS v4 CO product.

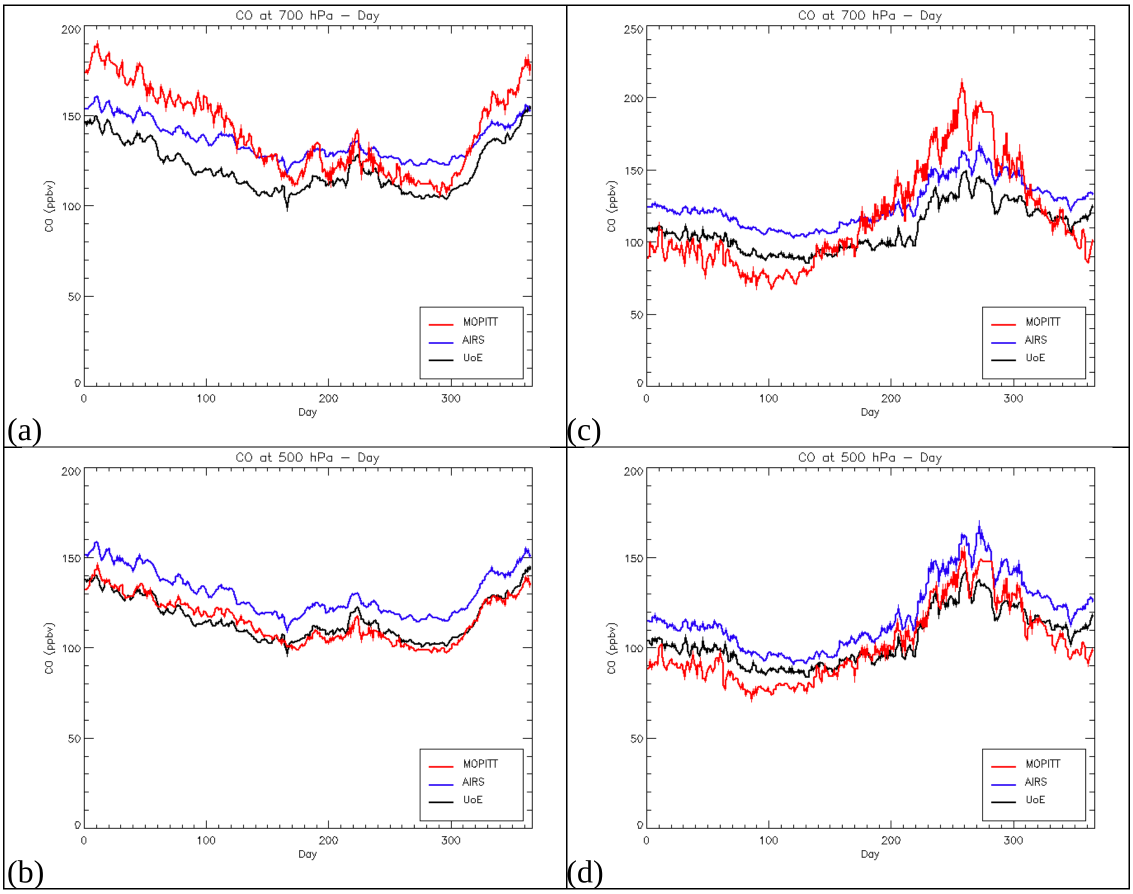

Figure 6.7 Time series of daily mean CO at 700 hPa and 500 hPa CO for the CAF and SAF regions illustrated in Figure 6.5, for 2006. The CAF region is bounded by the box, 0°N, 20°N, 15°W, and 40°E. The SAF region is bounded by the box, 30°S, 0°N, 10°E, and 40°E. (a) CO at 700 hPa for CAF, (b) CO at 500 hPa for CAF, (c) CO at 700 hPa for SAF, and (d) CO at 500 hPa for SAF.

6.4.4. Indonesia

Observation of the maps of monthly mean CO revealed a large CO emission event over Indonesia during October and November. The time series for a region covering this event (IND) is shown in Figure 6.8. This illustrates quite clearly the significance of this event, relative to typical concentrations of CO for the other months of the year. At 500 hPa the CO concentration is observed to increase sharply by ~60 ppbv, a very significant increase when compared to the relatively small CO fluctuations seen in the preceding months.

Another point to note is that the range of CO fluctuations in the UoE CO at 700 hPa is noticeably closer to that of MOPITT, compared to earlier observations for the two

African regions Figure 6.7. This is probably due to two factors. The first is the tendency for the UoE retrieval to perform better over ocean areas than over land, with higher correlations observed between UoE and MOPITT retrievals for ocean regions (Figure 5.12). As the IND region contains a far greater proportion of ocean pixels than the CAF or SAF region, it is likely that this factor contributes to the better agreement between the two retrievals observed in Figure 6.8. The second potential factor is the influence of CO concentrations at higher altitudes on the UoE retrieval at 700 hPa. The peak CO concentration observed by the UoE system in the IND region at 500 hPa is considerably higher than that from MOPITT. As UoE retrieval at 700 hPa is heavily influenced by CO at 500 hPa and above (while the equivalent MOPITT retrievals are dominated by CO between 700 and 500 hPa) it is possible that the similar range observed at 700 hPa is partly a consequence of the differing altitude sensitivities of the two instruments.

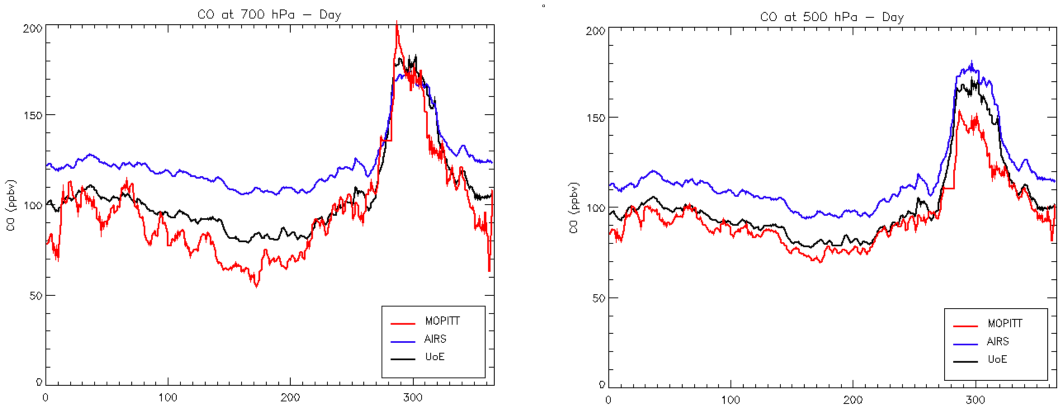

(a) (b)

Figure 6.8 Time series of daily mean CO for the IND region (with bounds of 10°S, 10°N, 90°E, and 140°E) illustrated in Figure 6.5, for 2006. (a) CO at 700 hPa. (b) CO at 500 hPa.

6.4.5. China, and the North Pacific

A region covering Eastern China, and three regions over the North Pacific were selected to try to demonstrate the potential of the UoE CO retrieval scheme for monitoring the global transport of CO. The time series for these regions are shown in Figure 6.9. In the CO time series for the CHI region there is some increase in CO during the first few months for the year. This is followed by a decrease with a minimum around July, before CO concentrations rise again. These trends are most apparent in the MOPITT time series at 700 hPa but can also be seen in the 500 hPa time series. Similar trends are also observed in the time series over the regions in the North Pacific. Emissions from the CHI region have relatively small seasonal variation [Edwards *et al.*, 2004], so any trend observed is likely to be dominated by seasonal variations in OH concentration. It is this seasonal variation in OH that dominates the trends in CO over the North Pacific regions, with the trends being more marked in these regions as there is no direct contribution to CO from industrial sources or biomass burning.

As there are no direct CO sources in these regions and seasonal variations in OH affect all the regions, it was thought that it may be possible to demonstrate that CO concentrations in North Pacific regions are affected by CO transported from Eastern Asia. In order to try to establish if any correlation exists between the CHI and North Pacific regions, the cross correlations between the UoE time series at 500 hPa were calculated (Figure 6.9c). The lag time to peak correlation is observed to increase for each NPC region, moving eastward, with lag times of approximately 5, 10 and 15 days. Although much more rigorous analysis using meteorological data would be required to fully characterise CO transport events, this simple correlation analysis suggests that the UoE CO product has the potential to be used in such an application.

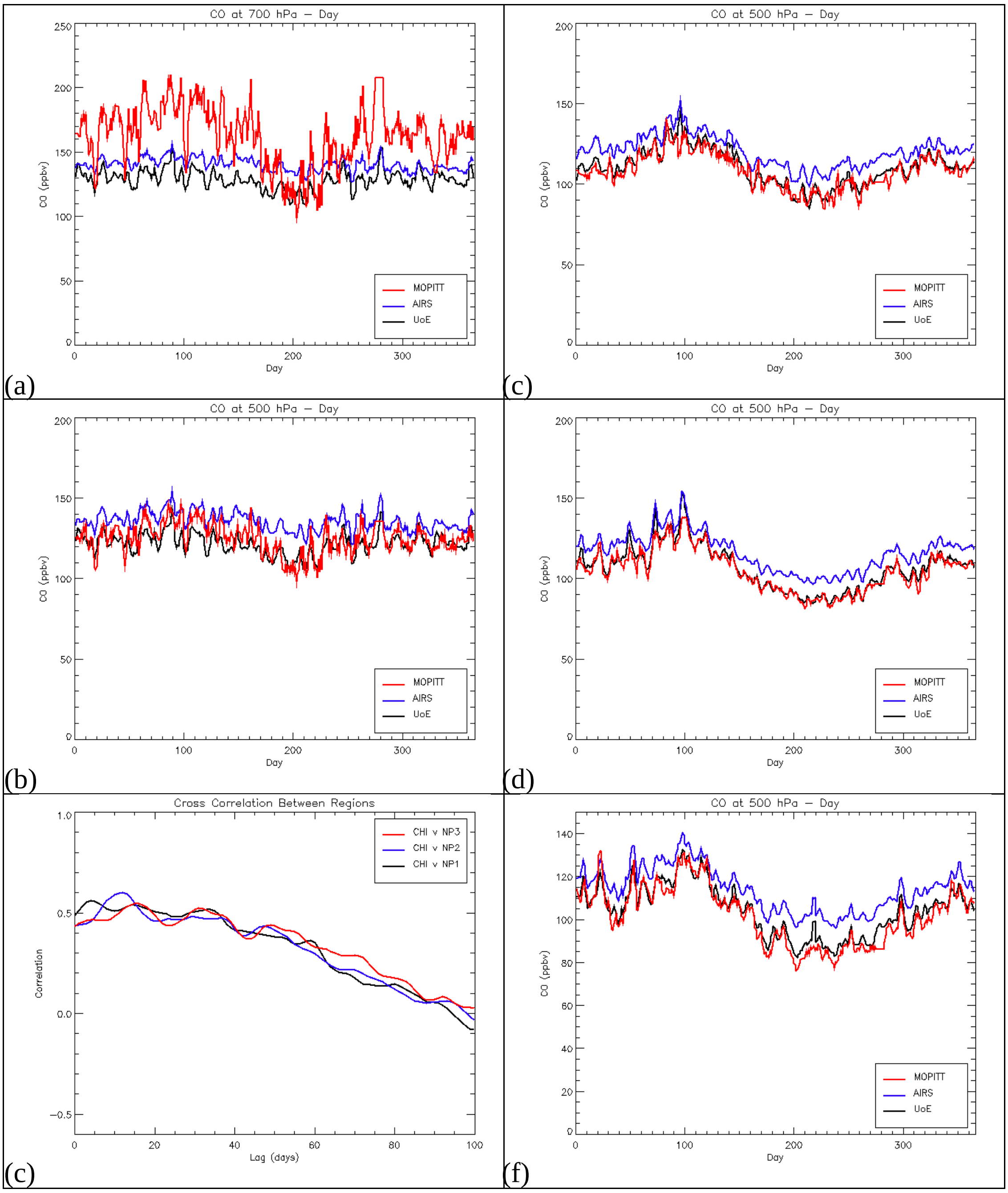

Figure 6.9 (a,b) Time series of daily mean CO at 700 and 500 hPa for CHI region (with bounds of 20°N, 45°N, 110°E, and 130°E), for 2006. (c) Cross correlation of CO at 500 hPa between CHI and NPC regions. (d-f) Time series of daily mean CO at 500 hPa for NPC1, NPC2 and NPC3 regions. The bounds of these regions are as follows: NPC1 (20°S, 45°N, 150°E, and 180°E), NPC2 (20°S, 45°N, 180°W, and 150°W), and NPC3 (20°S, 45°N, 150°W, and 120°W). All regions are illustrated in Figure 6.5.

6.5. Vertical Transport

As the UoE retrieval scheme performs well in the mid-troposphere there is clearly potential (as shown in §6.4.5) for it to be used in studies of global CO transport. However, the strong dependence on mid-tropospheric CO in the retrievals in the lower and upper troposphere suggests that the UoE product is not suitable for investigating vertical transport of CO on its own. In an effort to support this proposal, the cross correlations between the time series of CO at 700 and 250 hPa were calculated for two of the regions of interest (SAF and IND). The cross correlations for all three retrieval schemes are shown in Figure 6.10. For the case of UoE and AIRS the peak correlations occur at a lag period of zero days, confirming that the CO retrievals at 700 and 250 hPa are share a strong common dependency (on CO at ~500 hPa). The results for MOPITT are somewhat different, with the peak correlation occurring for a time lag of ~10-20 days, between CO at 700 hPa and CO at 250 hPa. This indicates that the lower and upper troposphere CO retrievals from MOPITT are more independent than they are for UoE. This is supported by the typically higher number of degrees of freedom of signal observed in the MOPITT data (§5.2.7).

It is clear from this analysis that the strong dependency of the UoE retrieval on CO at 500 hPa makes it unsuitable to investigate the vertical transport of CO. However, there is still potential for AIRS to be used in vertical transport studies, by combining its robust observations in the mid-troposphere with lower or upper troposphere observations from other satellite sensors. This possibility is explored further in Chapter 7.

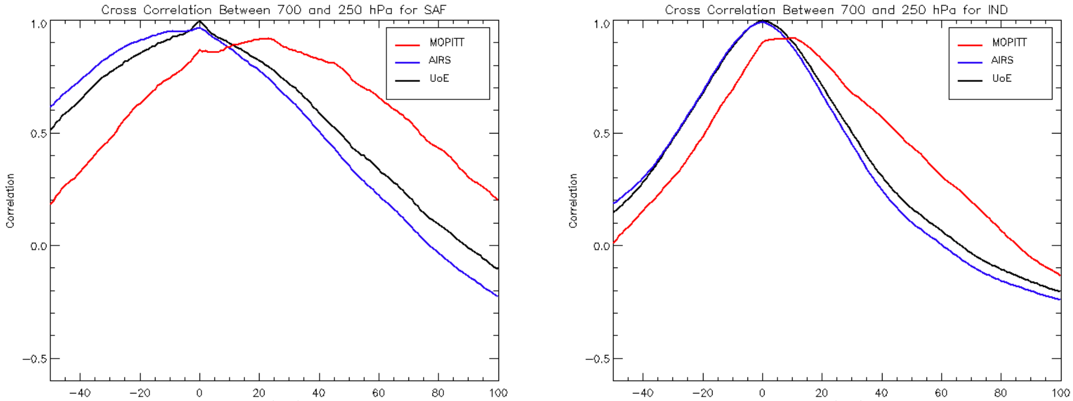

(a) (b)

Figure 6.10 Cross correlations of daily mean CO time series between CO at 700 and 250 hPa for (a) SAF and (b) IND regions. The bounds of these regions are as follows: SAF (30°S, 0°N, 10°E, and 40°E), and IND (10°S, 10°N, 90°E, and 140°E).

6.6. Summary

Through the analysis of time series of CO concentrations over different regions, the work of this chapter has demonstrated the potential of the AIRS instrument for observing seasonal CO cycles. As AIRS has now been operational for over 5 years, there is clearly potential to use AIRS CO observations to investigate inter-annual CO variability, and in the future (with longer time series), look at long term trends.

Some further insight into the relative performance of the UoE and MOPITT CO retrievals has also been gained from this work. The higher sensitivity of MOPITT to CO in the lower troposphere has been demonstrated, through the increased range in CO concentrations in the time series at these levels, and through analysis of the percentage contribution from the prior.

Finally, the results of some preliminary work into using AIRS in CO transport studies were presented. These revealed that AIRS is unsuitable (on its own) for tracking vertical transport of CO but does have potential for tracking horizontal transport. The potential of AIRS for studying horizontal CO transport and the possibility of combining AIRS with another satellite instrument to detect the vertical transport of CO are investigated further in Chapter 7.

Chapter 7. CO Case Study

7.1. Introduction

In Chapter 6 the potential of the UoE CO product for tracking the horizontal transport of CO was briefly demonstrated. This potential application is further explored in this chapter, through closer analysis of a case study. Although Chapter 6 revealed that the AIRS was unsuitable for tracking the vertical transport of CO, there is still potential for AIRS to be used in conjunction with another satellite instrument for this purpose. This potential is investigated in this chapter through comparison of the UoE CO product with upper tropospheric CO measurements from the Microwave Limb Sounder (MLS).

Observation of the UoE CO data set for 2006 revealed a significant CO event for a region over (and to the west of) Indonesia during October and November. This area was selected as a case study to further investigate CO transport (both horizontally and vertically).

Biomass burning is used as a method of land clearing for agriculture in Indonesia. This biomass burning follows a seasonal cycle governed by the prevailing weather conditions, namely the seasonal variations in rainfall. From May to September, the southeast monsoon dominates the weather conditions and Indonesia experiences a dry season. October and November form a transition period between dry and wet seasons, before the northwest monsoon brings about the wet season, from December to March. Biomass burning practices follow this seasonal variation in rainfall, with the number of fires peaking in the later part of the dry season. The “slash and burn” clearing methods used in cultivation can often result in uncontrolled wildfires developing. The land clearing methods employed result in the build up of peat deposits [Bettwy, 2007] which are vulnerable to wildfires. As discussed by Andreae and Merlet [2001] these smouldering fires can release large quantities of smoke and CO into the atmosphere.

These emissions frequently result in significant problems of haze affecting surrounding areas. In 2006 there was a moderate El Ninõ event, where positive sea surface temperature anomalies in the eastern tropical Pacific affected weather conditions over Indonesia. This resulted in Indonesia seeing lower than normal levels of rainfall during the last three months of 2006 and also reduced convection over the region [Logan *et al.*, 2008]. Consequently the land in this region became exceptionally dry, enabling wildfires to spread more easily and extending the period of biomass burning (normally brought to an end during the transitional period between the southeast and northwest monsoons). The combination of the increase in the number of fires and the reduced convection in the region resulted in an intense haze that had a considerable impact on the region for a number of weeks (Aglionby [2006] and Reuters [2006]).

7.2. Fire Counts

Fire count data were obtained from the ATSR World Fire Atlas, from the Data User Element of the European Space Agency [Arino and Plummer, 2001]. The ATSR active fire algorithm uses the instrument's 3.7 μm channel brightness temperature ($BT_{3.7}$) to determine the locations of fires. Pixels (at 1 km resolution) with $BT_{3.7}$ > 308 K at night time are flagged as containing an active fire. The ATSR active fire algorithm only considers night time observation in order to avoid problems with solar reflection. As only night time data are used, this product provides an underestimate of the fire counts. Like any IR sounding satellite instrument, ATSR also suffers data loss through cloud cover (and potentially as a result of the haze associated with the biomass burning event in Indonesia). A further limitation of this data is the lack of information about the intensity of the fires detected. In order to fully understand the evolution of CO from biomass burning events, information about the radiative power of the fire would be required. Although fire count data have some limitations it is a useful starting point for investigating the transport of CO from biomass burning events.

Daily ATSR fire count data were totalled over a region centred on Indonesia (lon. [90,140] and lat. [-10, 10]) and the time series calculated for 2006 (Figure 7.1a). Aside from two small peaks around February and March, the number of fire counts is very low for the first half of the year. Around late July, ATSR begins to consistently detect more fires in the region, until a sharp peak in the number of fire counts is observed around the beginning of October. High fire counts then persist into November, coinciding with the arrival of the North monsoon rains to the region.

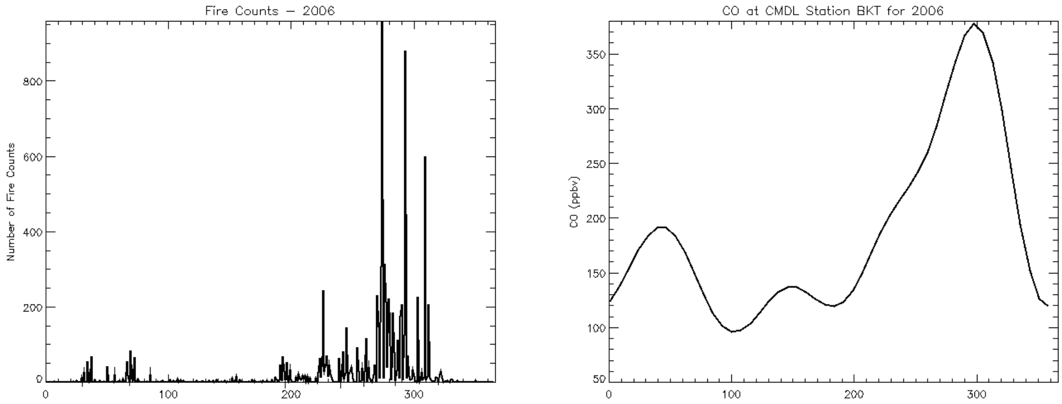

(a) (b)

Figure 7.1 (a) ATSR fire counts for the IND2 region (longitude [90,140], latitude [-10,10]). (b) CO at the CMDL ground station, Bukit Kototabang, Indonesia (BKT). BKT is located at the coordinates [100.32, -0.20], and 864 m above sea level.

In addition to the fire count data, CO observations from the CMDL monitoring station at Bukit Kototabang (BKT), Indonesia were obtained. This ground level station is located 864m above sea level at the coordinates, lon. 100.32°, lat. -0.20°. The time series of the weekly observations are shown in Figure 7.1b and shows good agreement with the fire count time series (Figure 7.1b), with a large peak in CO around October.

7.3. Horizontal Transport

The monthly mean UoE CO product at 500 hPa is shown for October and November 2006, in Figure 7.2. Strongly elevated CO concentrations are observed directly over Indonesia in October, with high levels of CO also seen over an extensive surrounding region. In November the peak CO concentration is lower and the elevated region of CO has shifted westward, across the Indian Ocean. This apparent long-range transport of CO from the Indonesian biomass burning is in agreement with the prevailing wind-direction for the region and time (Figure 7.3). In an effort to confirm that the elevated CO over the Indian Ocean is a consequence of the biomass burning in Indonesia, further analysis of the UoE CO and fire count time series is carried out.

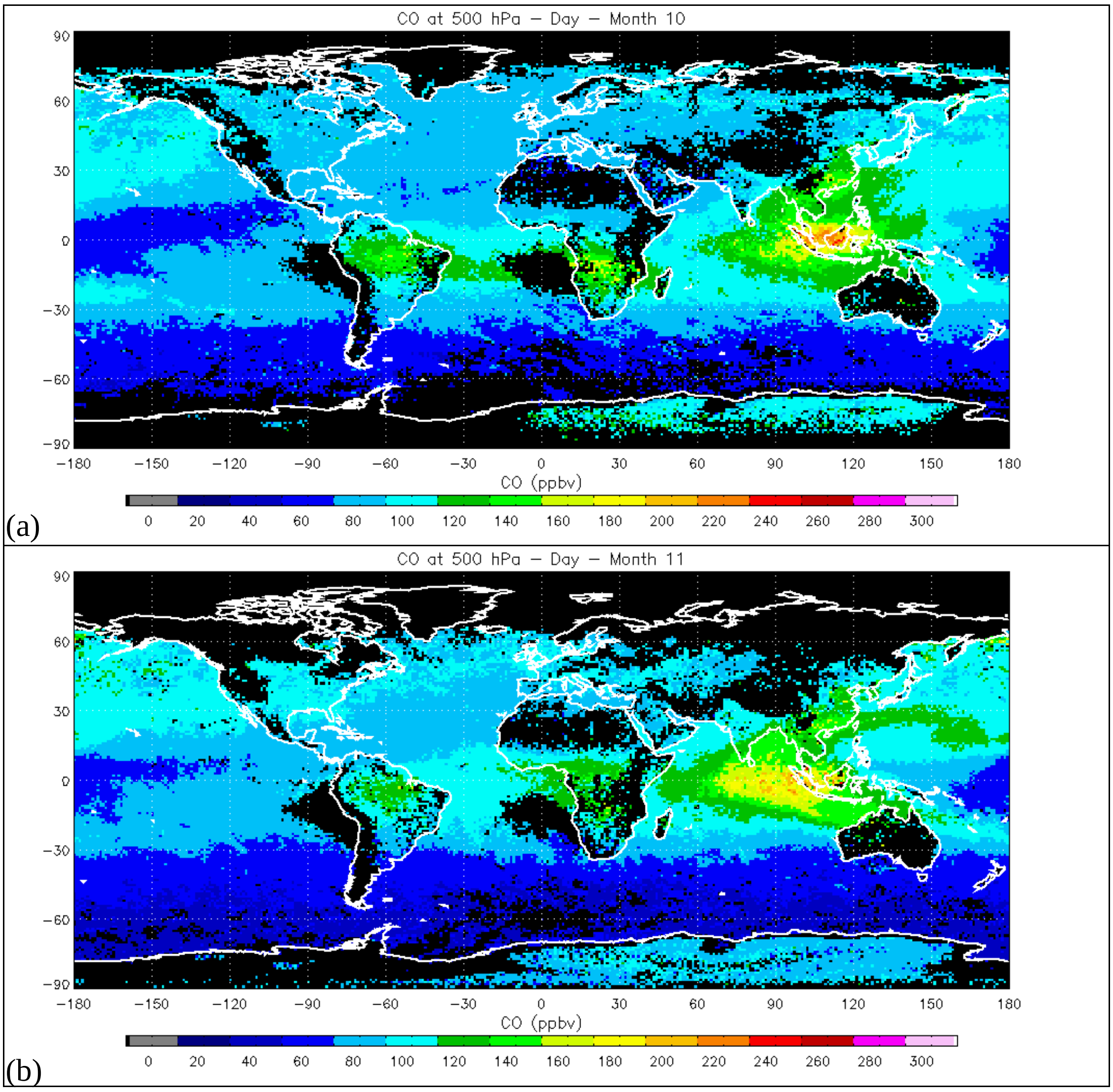

Figure 7.2 Monthly mean UoE CO at 500 hPa for (a) October and (b) November 2006.

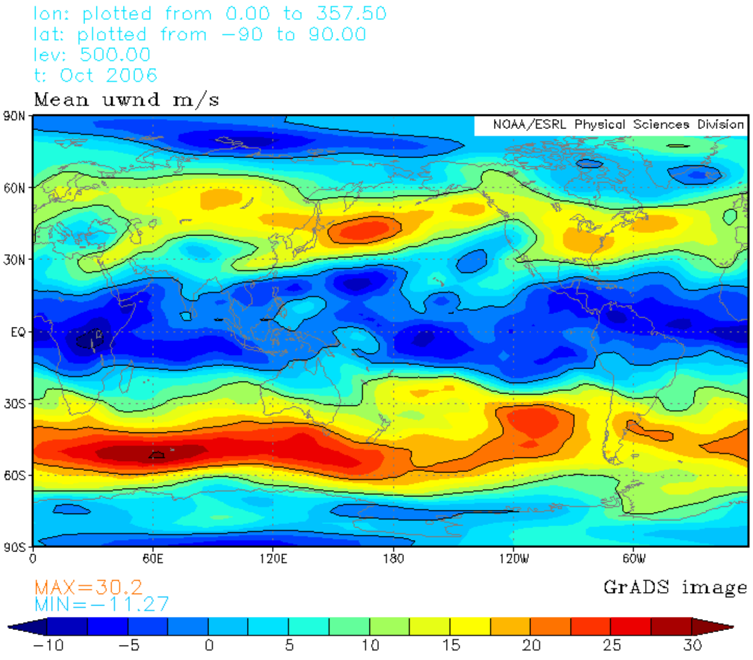

Figure 7.3 Mean u-wind speed at 500 hPa for October 2006 from NOAA NCEP reanalysis data. Image obtained from **http://www.cdc.noaa.gov/**.

CO time series were calculated from the UoE daily product, over the Indonesian (IND) source region ([90,140] and lat. [-10, 10]) and for 5° latitude by 10°longitude grid boxes across the globe. As commented on in Chapter 6, the excellent coverage of the AIRS instrument removes any requirement to smooth the time series for such regions, in order to extract the signal from synoptic variability. However, when performing cross correlation analysis on a global scale it is necessary to remove the effect of naturally occurring background correlations between regions. Such correlations are primarily due to the seasonal variations in OH concentration (discussed in Chapter 1), and are removed by performing the correlation analysis on differenced time series. A 60 day moving average was applied to the time series and then subtracted from the daily time series, before the correlation analysis was carried out. Cross correlations between time series for the IND source region and each grid box were calculated, and maps of the peak correlations and corresponding lag times were generated (Figure 7.4 b and e). Equivalent maps are also shown for the correlations and lag times to the first and last instances of correlations passing a 0.1% significance test (Figure 7.4 a, c, d and f). An example of the cross correlation time series is shown in Figure 7.5.

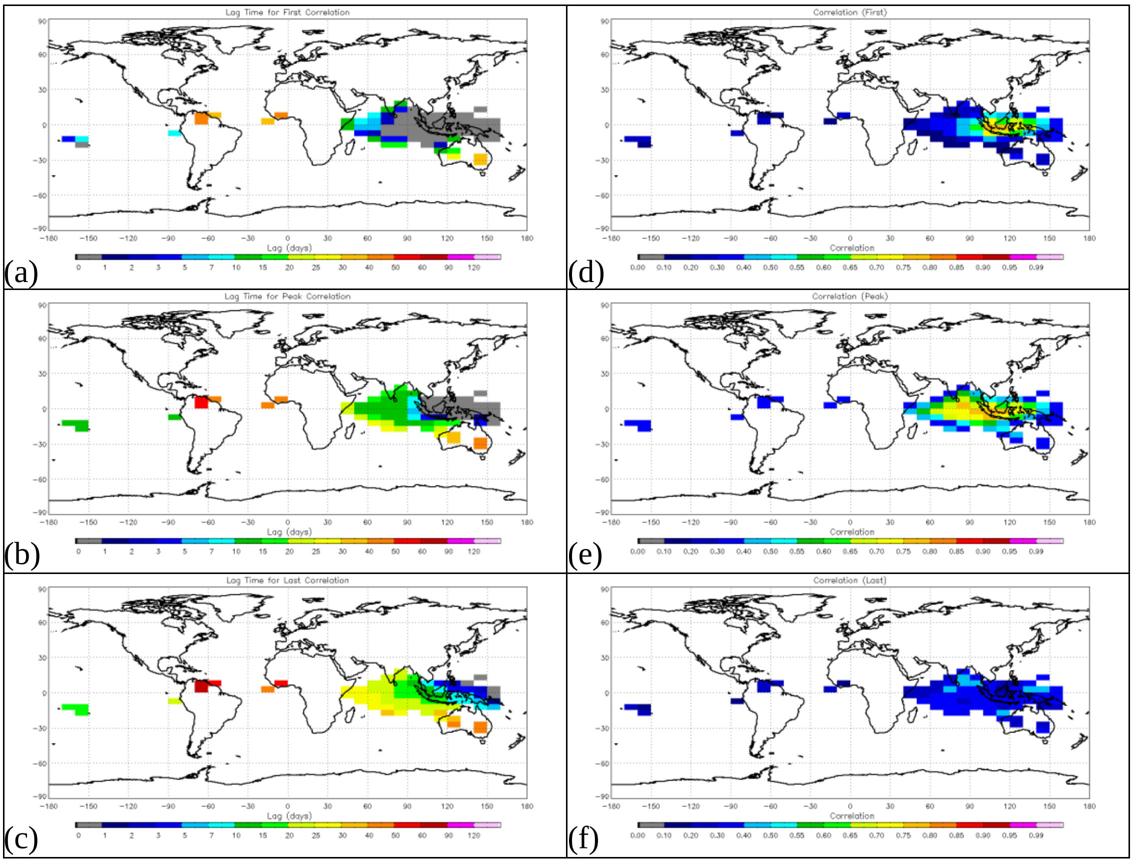

Figure 7.4 Maps of lag times for correlations between IND region and 10° longitude by 5° latitude, for UoE CO at 500 hPa. . (a, d) Lag time and correlation for first significant correlation. (b, e) Lag time and correlation for peak correlation. (c, f) Lag time and correlation to last significant correlation.

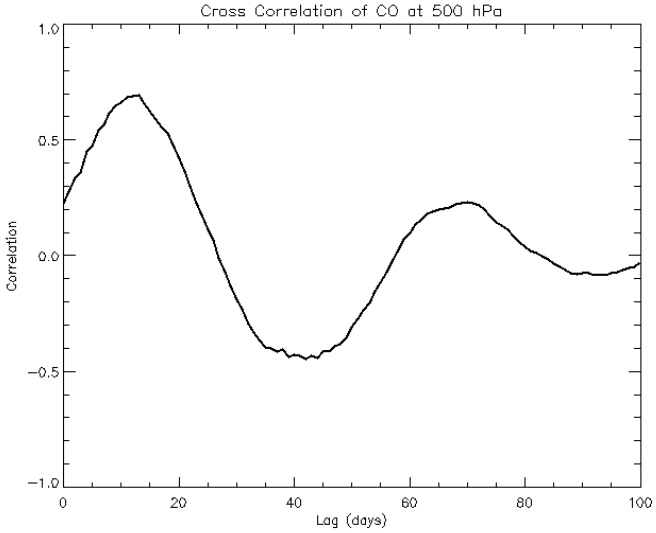

Figure 7.5 Example of cross correlation time series showing correlation with lag time between CO in the grid box with longitude and latitude bounds of [70,80] and [0,5], and CO in the IND region.

In Figure 7.4b the lag time (to peak correlation) is seen to increase directly westward of the source region (IND), with lag times ranging from 0 days over the source region to 20-25 days near the east coast of Africa. This corresponds to wind speeds of approximately 2 to 6 ms^{-1}, consistent with monthly mean wind speed data for October shown in Figure 7.3. The degree of correlation is also observed to decrease away from the source region, an expected result as the CO disperses away from the source. This result is further supported by the maps of lag time (and corresponding correlation) to the earliest and latest occurrences of significant correlation between grid boxes and source. Some correlation is typically observed up to ten days prior to and ten days after the peak correlation. Considering the meteorology and the generality of this correlation study this is a reasonable result.

Similar analysis was carried out looking at the correlations between the ATSR fire count time series and the UoE CO product at 500 hPa. Maps of correlations and lag times, equivalent to those in Figure 7.4, are shown in Figure 7.6. For this analysis, cross correlations were calculated between the ATSR fire count data, with a 3-day moving average applied, and the unsmoothed UoE CO time series. Differenced time series were not used as there is no seasonal background trend in the fire count data. Unlike the analysis of correlations of CO between regions, the analysis of fire count to CO correlations did not yield robust results globally. Consequently, this analysis was limited to a localised region around the source.

The lag time to the peak correlation (Figure 7.6b) is typically in the range of 10 to 15 days. As the CO emissions are likely to be heavily influenced by smouldering peat land fires (rather than more intense fires in the flaming stage [Edwards *et al.*, 2004]) it is reasonable to expect such a delay in the transport of CO from the surface to 500 hPa. Comparison of Figure 7.6b with the equivalent plot for CO correlations Figure 7.4b shows additional time lags of this length to be present at the western edge of the transport region. This illustrates that CO emissions from large biomass burning events can affect an extensive region for considerable periods of time.

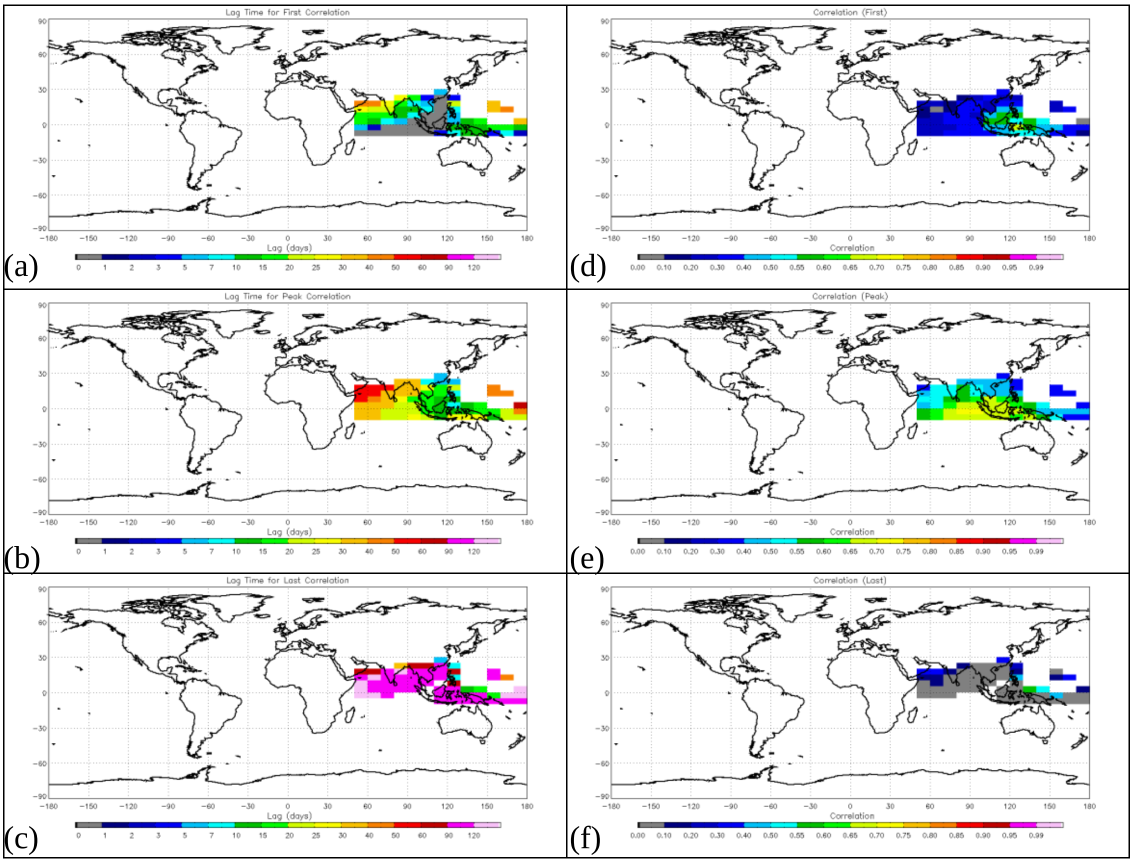

Figure 7.6 Maps of lag times for correlations between ATSR fire counts in IND region and UoE CO at 500 hPa in grid boxes of 10° longitude by 5° latitude. (a, d) Lag time and correlation for first significant correlation. (b, e) Lag time and correlation for peak correlation. (c, f) Lag time and correlation to last significant correlation.

7.4. Vertical Transport

In Chapter 6 AIRS was shown to be unsuitable for making observations of the vertical transport of CO. Although this is the case, there is still potential for AIRS to be used in conjunction with another instrument, to track the vertical transport of CO. The MLS instrument, onboard the Aura satellite, is one such instrument. MLS measures CO, predominantly in the stratosphere, but also in the upper troposphere, down to 215 hPa [Filipiak *et al.*, 2005]. Typical averaging kernels for MLS CO retrievals are shown in Figure 7.7 (taken from Livesey *et al.* [2008]). These averaging kernels are for CO retrievals in the tropics but are representative of all atmospheric conditions, as orbital and seasonal variations in the averaging kernels are small [Livesey *et al.*, 2008]. MLS averaging kernels are more sharply peaked and contain more distinction between levels than either the UoE or MOPITT averaging kernels (Figure 5.13). The MLS averaging kernels also peak at the profile levels which they represent, except for the case of 316 hPa averaging kernel which peaks around 215 hPa. As a result, the MLS retrievals at each pressure level (down to 215 hPa) are actually dominated by CO concentrations at these levels, unlike AIRS and MOPITT in many cases.

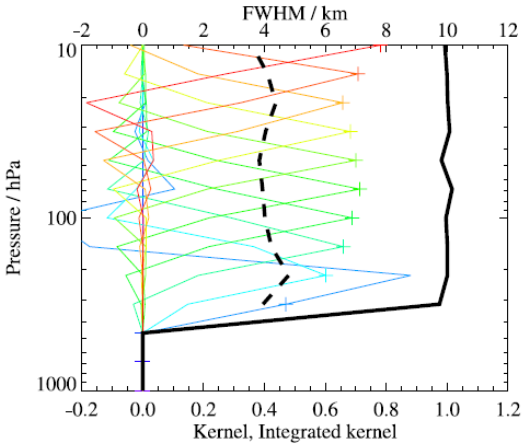

Figure 7.7 Typical vertical MLS averaging kernels for CO retrievals in the tropics. Coloured lines represent the averaging kernels for each retrieval level (denoted by the plus signs). The dashed black line indicates the vertical resolution, derived from the full width at half maximum (FWHM) of the averaging kernels. The solid black line represented the total integrated area under each kernel. Taken from Livesey *et al.* [2008].

As both AIRS and MLS are housed onboard NASA's A-train satellites, the time difference between AIRS and MLS observations is small. This combination of similar measurement times and very different altitude sensitivity to CO makes the MLS instrument a suitable candidate for use with AIRS to investigate vertical CO transport.

Monthly mean maps of the MLS CO product at 147 hPa for October and November are shown in Figure 7.8. Comparison with the equivalent UoE 500 hPa CO product (Figure 7.2) shows broad agreement in the CO distributions, with elevated values over the Indonesian region, Southern Africa, and South America. One important point to note about the MLS CO product is its sparse coverage relative to AIRS, and indeed MOPITT. This is because MLS is a limb-viewing instrument, while both AIRS and MOPITT are nadir-viewing instruments that also employ cross-track scanning. Coverage is sparser towards the poles, as the MLS CO product degrades at high latitudes. In the tropics, MLS CO retrievals in the upper troposphere are accurate to ~30 ppbv.

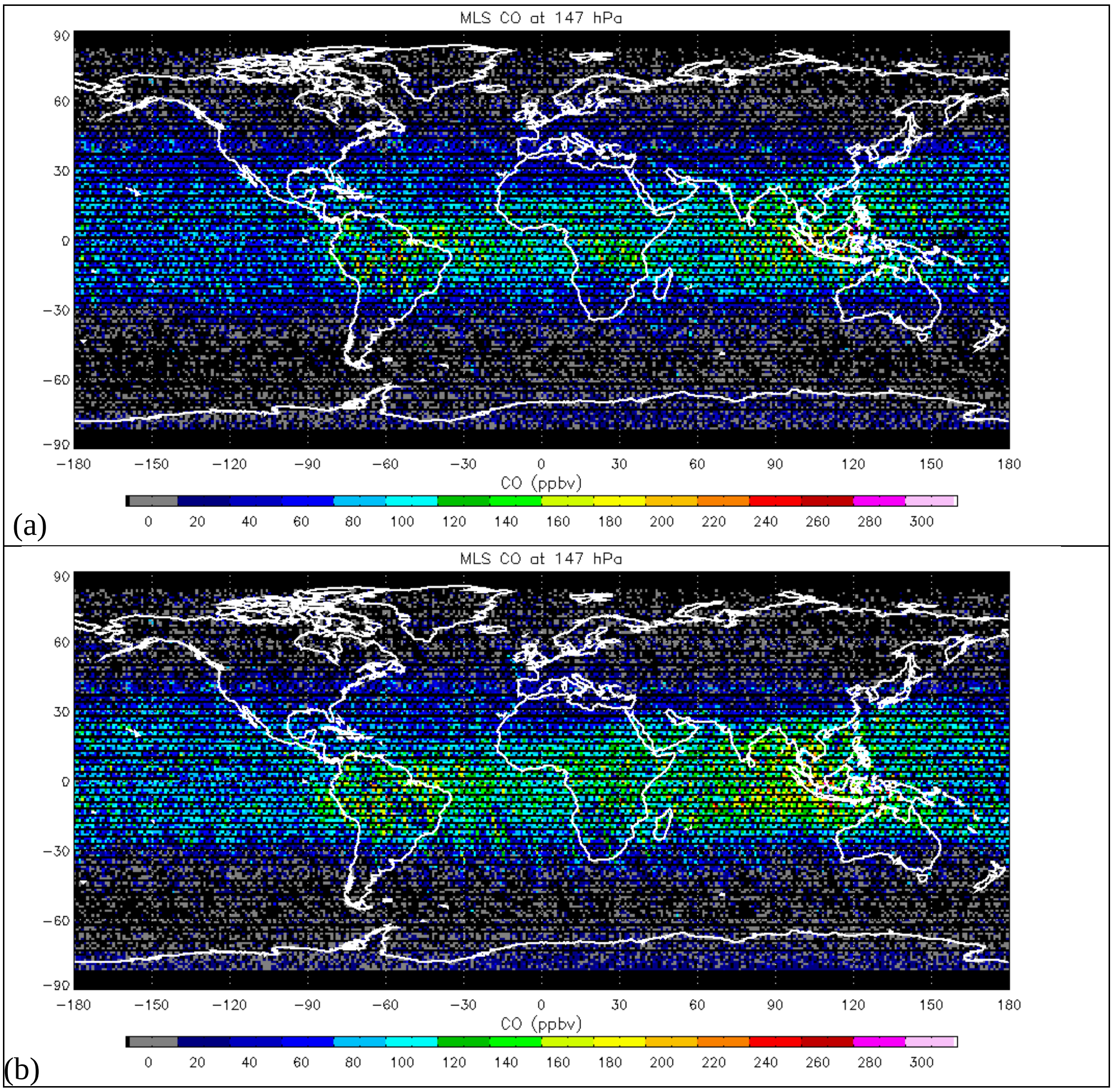

Figure 7.8 Monthly mean MLS CO at 147 hPa for (a) October and (b) November 2006.

In order to try and show the vertical transport of CO from the Indonesian biomass burning event, time series of the mean CO retrievals for the region (bounded by 10°S, 10°N, 90°E, and 140°E) were analysed. The time series of the MLS 147 hPa CO product was compared to time series of lower, middle and upper tropospheric CO from both the UoE and MOPITT retrievals. A 3-day moving average was applied to all time series before analysis. This was done in order to reduce the effects inter-day variations in the regions viewed by the satellite instruments, and also the effects of variations in atmospheric conditions on the retrievals. The time series and plots of cross correlation between UoE (and MOPITT) and MLS are shown in Figure 7.9.

In Figure 7.9c MLS CO at 147 hPa is compared directly to UoE and MOPITT retrievals at 150 hPa. At this level MLS sees significantly higher concentrations of CO than UoE. This large bias is primarily due to the lack of sensitivity of the UoE retrieval in the upper troposphere (and subsequent dependence on the prior and CO concentrations at lower altitude). This can be illustrated further by comparison of the UoE averaging kernels for the Indonesia region (Figure 7.10a) and the typical MLS averaging kernels (Figure 7.7). The UoE retrieval at 150 hPa is observed to have its peak contribution from CO at 350 hPa, while the MLS retrieval at 147 hPa has very little contribution from CO below 200 hPa. As the retrievals from the two instruments at this level are dominated by CO at different altitudes, it is not surprising that there is a significant bias between the two.

MOPITT retrievals at 150 hPa are seen to provide better agreement with MLS (Figure 7.9), with a considerable reduction in the bias observed between MLS and UoE retrievals. This is due to MOPITT being more sensitive to CO at this altitude than AIRS, illustrated by the MOPITT averaging kernels shown in Figure 7.10b. Although MOPITT retrievals at 150 hPa are influenced by CO at lower altitudes, the peak contribution does come from CO at 150 hPa, as is the case for MLS retrievals. Another potential contribution to the bias between MLS and the other two instruments is the possibility of MLS overestimating CO at this altitude [Filipiak *et al.*, 2005].

As well as the bias, a considerable difference in the variability is also observed, with MLS exhibiting a higher degree of variance. This may be partly due to MLS being more sensitive than AIRS to CO at this altitude, but is likely to be a result of the sparse coverage of the MLS instrument. Although there are significant differences in the CO products, all three instruments capture a peak in CO through October and November. Inspection of this time series cross correlation between instruments at this level (Figure 7.9f) indicates that MLS and MOPITT see CO at this altitude at the same time, while retrievals from AIRS see elevated CO levels around 10 days earlier. This difference between AIRS and the other two instruments is a result of their differing sensitivity to CO with altitude, illustrated in the averaging kernels of Figure 7.7 and Figure 7.10. AIRS CO retrievals at 150 hPa are dominated by CO at lower altitudes, compared to MLS and MOPITT, the retrievals at 150 hPa from both of which are dominated by CO at this level.

Further comparisons of the MLS 147 hPa CO time series with those of 500 and 700 hPa CO from UoE and MOPITT are show in Figure 7.9 (a, b, d and e). Again, good agreement is seen between the different CO measurements. As for the 150 hPa case, the UoE 500 and 700 hPa CO time series lead that of MLS 147 hPa CO by about 10 days. A similar lag between MLS and MOPITT is also observed at these levels. These results are a good indication that there is significant vertical transport of CO into the upper troposphere from the biomass burning in Indonesia.

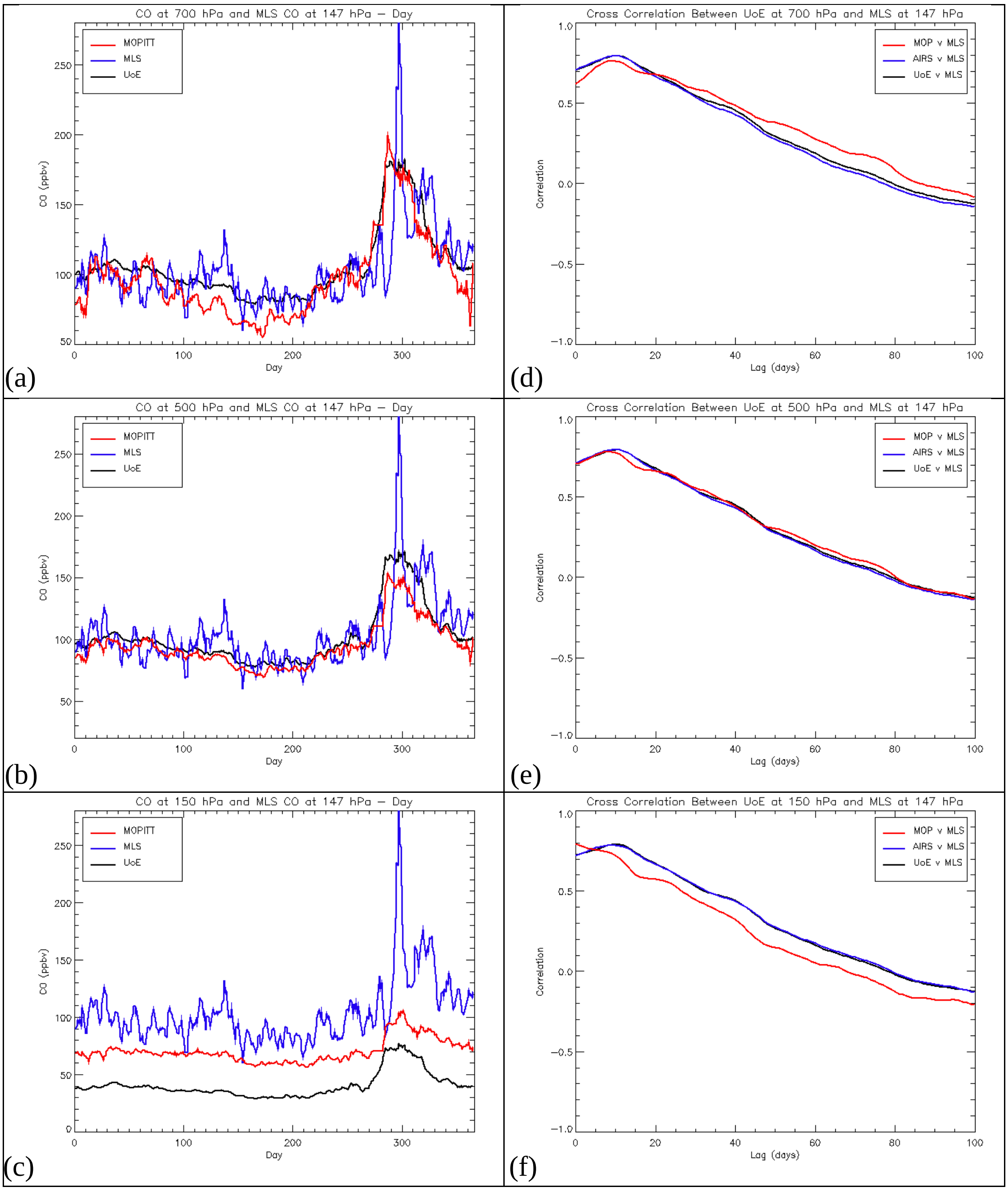

Figure 7.9 (a to c) CO time series at 700, 500, and 150 hPa (from UoE and MOPITT) compared to MLS CO at 147 hPa. (d-f) Inter-instrument cross correlation for the time series presented in (a to c). Resulted presented are based on daily mean CO concentrations for the Indonesian region, bounded by 10°S, 10°N, 90°E, and 140°E.

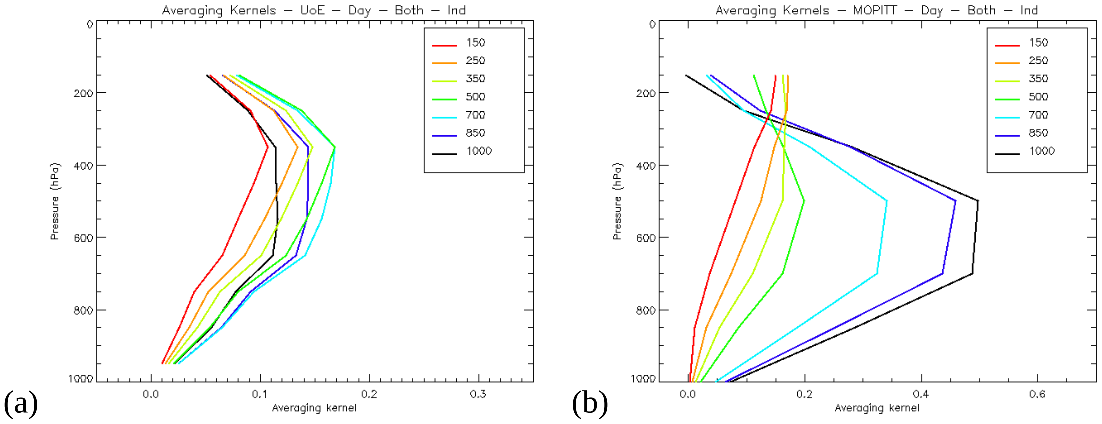

Figure 7.10 Mean averaging kernels for the Indonesia region (bounded by 10°S, 10°N, 90°E, and 140°E) for October 2006. (a) UoE averaging kernels. (b) MOPITT averaging kernels.

7.5. Summary

Large biomass burning events have the potential to spread pollution across large geographic regions, affecting local air quality in regions far from the emission source. The biomass burning in Indonesia in late-2006 is a good example of such an event, with the resultant pollution severely affecting air quality over a large area.

Using a combination of the UoE CO product and ATSR fire count data, the potential of the AIRS instrument for tracking the global transport of CO (and by proxy, pollution) has been demonstrated. Correlation analysis of regional CO time series have shown transport of CO from Indonesian fires, on timescales consistent with the prevailing meteorology and fire type.

Comparison of the UoE and MOPITT observations with MLS measurements revealed significant vertical transport of CO, from the Indonesian fires into the upper-troposphere. A lag time of about 10 days was observed between CO at 500 hPa and CO at 150 hPa. Although it has been possible to demonstrate vertical transport into the upper troposphere using a combination of AIRS and MLS, an improved CO retrieval through the synthesis of these instruments does not look promising. This is due to a combination of the limited coverage of MLS and the small degree of overlap in the vertical sensitivity of the two instruments.

Chapter 8. Summary and Future Work

As the principal sink of the hydroxyl radical (OH) in the troposphere, carbon monoxide plays an important role in atmospheric chemistry. Although CO itself is not a greenhouse gas, its strong influence on the oxidising capacity of the atmosphere affects the concentrations of greenhouse gases such as CH_4 and O_3. As well as this indirect influence on the climate, CO also indirectly affects air quality through its role as a precursor to O_3 in the presence of NO_x. The potential impacts on human health and agricultural economy through increased O_3 are exacerbated by the fact that enhanced CO and NO_x concentrations are associated with human activity (industrial and biomass burning).

The influence of CO concentrations on climate and air quality makes CO an extremely important constituent of the atmosphere. As such there is a need for good understanding of its behaviour, from accurate estimates of emissions through to its chemical interactions in the atmosphere. Satellite observations of CO on a global scale offer one potential means by which our understanding of atmospheric CO can be improved. Since the beginning of the 21st century a number of different satellite instruments capable of measuring tropospheric CO have become operational. Each of these offer somewhat different information about CO. Combined, they have tremendous potential to enhance our understanding of CO in the troposphere.

One satellite instrument that has the potential to add to our knowledge of CO is the Atmospheric Infra-Red Sounder (AIRS), onboard NASA’s Aqua satellite. This high spectral resolution IR sounder is mainly sensitive to CO in the mid-troposphere and offers one distinct advantage over other CO sensitive satellite instruments. That is greatly improved spatial coverage. This comes through the application of cloud clearing techniques which enable AIRS to provide near-global coverage on a daily basis. As CO has a lifetime of 1-3 months it can be transported over large distances by favourable meteorological conditions. The excellent daily coverage of AIRS makes it potentially the most suitable instrument for observations of CO transport.

The capability of AIRS for making CO observations was demonstrated by McMillan *et al.* [2005], showing CO retrievals from the AIRS v4 algorithm to be accurate to ~10% in the northern hemisphere. Although the AIRS v4 algorithm was shown to provide retrievals of a reasonable quality, it was thought that these measurements could be improved upon through the use of more optimal retrieval techniques. This study set out to develop an alternative retrieval scheme based on the optimal estimation of Rodgers [2000] in an effort to provide improved CO retrievals from AIRS and as a means of independently assessing the quality of the AIRS v4 product. Optimal estimation methods were expected to offer improvements to the AIRS CO retrieval, particularly in terms of error estimation and characterisation. These are key features if any quantitative analysis is to be carried out using the CO observations.

In this study an alternative retrieval scheme, based on the *maximum a posteriori* (MAP) solution of Rodgers [2000], was successfully developed for AIRS CO retrievals. This was achieved through simulation work using the Reference Forward Model (RFM), which yielded valuable information about the sensitivity of AIRS to CO. It was observed through the influence functions, **K**, and the averaging kernels, **A**, that only ~50 from over 2000 AIRS channels exhibited sensitivity to CO, above instrument noise levels. This sensitivity was shown to peak in the mid-troposphere for all channels, with very little sensitivity at near-surface and upper-troposphere altitudes. Consequently, the developed retrieval scheme was expected to perform best in the mid-troposphere, with degradation in performance towards the surface and upper-troposphere.

In the development stage the importance of the prior information incorporated into the retrieval scheme was also illustrated. As the sensitivity of AIRS to CO decreases away from the mid-troposphere, the prior information becomes increasingly important. It is therefore necessary that the prior provides a realistic representation of the true state of the atmosphere. In this case, a realistic representation of a typical CO profile and the covariances between levels. This study used a prior covariance matrix based on the output of the chemical transport model (CTM), STOCHEM, with some damping applied to covariances between widely separated levels. As the covariance matrix is based on monthly mean model output, it potentially underestimates the variances, leading to a retrieval that may be overly constrained by the prior. It may be possible to improve upon this representation by generating the covariance matrix from an extensive set of globally representative *in situ* data or from a larger set of CTM data on a short time-step. However, the prior covariance matrix employed does have its basis in our knowledge of the chemical and physical dynamics of the atmosphere, and a measure of its influence on the retrieval is an inherent property of the optimal estimation technique.

The performance of the optimal estimation retrieval scheme, developed in this study was assessed through comparison with an extensive set of *in situ* aircraft measurements of CO. In terms of total common column CO the UoE retrievals were observed to be well correlated with both the *in situ* measurements and the AIRS v4 retrievals. The UoE CO product was also observed to be considerably less biased, relative to the *in situ* measurements, than the AIRS v4 product. Although good agreement was shown for total column CO, the degree of correlation was shown to be lower when CO concentrations on individual profile levels where considered. This is due to the varying sensitivity of AIRS to CO with altitude and subsequent variation in the contribution of the prior to the retrieval. Another feature of the AIRS CO products highlighted in the *in situ* validation study is the lower dynamic range of CO concentrations observed, relative to the range of CO concentrations present in the *in situ* data. This is likely to be a result of a combination of the influence of the prior on the retrievals and the fact that the AIRS observations are made at a much lower spatial resolution than the *in situ* data. In most cases the AIRS CO data, for each match-up with *in situ* data, is also the average of a number of retrievals and will reduce the range of CO concentrations.

Comparison with *in situ* observations is an important step in validating and understanding the performance of the retrieval. However, the sparsity of such *in situ* observations prevents us from obtaining a true understanding of the performance of the retrieval scheme on a global scale. Having demonstrated the accuracy of the UoE CO product through validation with *in situ* data, the performance of the UoE retrieval was further investigated through comparisons with the MOPITT CO product. MOPITT is the longest running CO observing satellite instrument and has undergone extensive validation [Emmons *et al.*, 2004]. Consequently its CO product is well understood and is often used as a benchmark for other CO observations [Buchwitz *et al.*, 2007] and [Luo *et al.*,2007], making it an ideal candidate to be used to investigate the UoE CO product.

Through comprehensive comparisons of the UoE and AIRS v4 CO products with MOPITT CO, considerable insight into the performance of all three retrievals was obtained. A great deal of work focussed on retrievals at 500 hPa, where AIRS was demonstrated to exhibit peak sensitivity to CO. At this level, excellent agreement between the UoE and MOPITT products was observed, both in terms of magnitude and variability. The AIRS v4 CO product was also shown to match the variability of MOPITT and UoE, but a significant positive bias in the magnitude of the CO concentrations was observed. This positive bias is due in part to the AIRS v4 CO product containing extremely limited information about the quality of the retrieval. As shown in Chapter 5 the AIRS v4 algorithm returns what is essentially the “first guess” profile in some cases where significantly lower CO concentrations are expected (e.g. over Antarctica and Greenland). In these cases the surface and atmospheric conditions make CO retrievals more difficult, and the UoE and MOPITT retrievals are also dominated by the prior. However, the additional information about the source of the retrieved values, inherent in the optimal estimation algorithms, allows the UoE and MOPITT products to be filtered to exclude such cases. This improved characterisation of the CO product enables flexibility in filtering methods, allowing the user to filter the data by means most suitable for their applications (e.g. a low % prior threshold could be used where accuracy is paramount, while a high % prior threshold could be used where maximum coverage is required).

As well as improving the bias, relative to MOPITT, and allowing the CO product to be filtered in terms of the contribution from the prior, the UoE retrieval also offers improvements in the estimates of retrieval error, over those from the AIRS v4 product. The advantage of the optimal estimation algorithm is illustrated in Chapter 5 through comparison of the retrieval errors at different levels in the profile. Unrealistic minimal variation in the AIRS v4 retrieval error is observed across the profile levels, with error estimates of ~20% at all levels. Much more realistic error estimates are given by the UoE retrieval, with errors ranging from ~10% in the mid-troposphere (where the sensitivity of AIRS to CO is highest) to values approaching the prior error estimate towards the surface and upper troposphere (where sensitivity to CO is low). As highlighted by Luo *et al.* [2007], CO retrievals must be accompanied by accurate error estimates if they are to be used in any quantitative analysis. Therefore, considering retrieval errors alone, the UoE CO product offers a significant improvement over the AIRS v4 product.

In addition to demonstrating the advantages of the UoE retrieval over the AIRS v4 algorithm, the work of Chapter 5 and Chapter 6 also provided an insight into the performance of AIRS CO retrievals relative to those from MOPITT. Although excellent agreement was shown between UoE and MOPITT at 500 hPa, significant differences were observed at other altitudes, and consequently in the total column CO. Deeter *et al.* [2003] proposed that MOPITT has the potential to distinguish between CO in the upper (350 to 150 hPa) and the lower (surface to 700 hPa) troposphere. This is supported by the analysis of the percentage contribution of the prior to the retrieved CO, in Chapter 6, particularly for the case of tropical latitudes. In this analysis AIRS was shown to essentially return information about CO in the mid-troposphere, with retrievals in the upper and lower troposphere heavily influenced by the prior. Consequently AIRS does not capture the range and variability of CO that is seen by MOPITT at these levels. This is particularly true in the lower troposphere, in regions with strong CO sources from biomass burning. In these regions significantly enhanced and highly variable CO concentrations are expected, and are observed in the MOPITT CO product. The UoE retrieval does not return such elevated values of CO and sees considerably lower levels of variability in lower tropospheric CO. Although the UoE CO product performs relatively poorly when compared to MOPITT in the lower troposphere, it does succeed in capturing more of the variability than the AIRS v4 product.

The lack of sensitivity of AIRS to CO in the lower and upper troposphere makes it unsuitable for looking at the vertical transport of CO (as outlined in Chapter 7). MOPITT has some potential to be used in this form of application, but is also limited by a lack of information content about the vertical structure of the CO profile. Although it is not possible to analyse vertical transport of CO using only the AIRS instrument, there is potential for making such observations using a combination of AIRS and other satellite instruments. This was demonstrated in Chapter 7, where the UoE and MLS CO products were used to show CO transport from the mid to upper troposphere. As AIRS lacks significant sensitivity to CO in the lower troposphere, there is also potential to combine AIRS with an instrument with higher sensitivity at these levels (e.g. SCIAMACHY) to investigate CO transport from the lower to mid-troposphere. In addition, the lack of sensitivity in the lower troposphere coupled with the knowledge about this, inherent to the optimal estimation retrieval, offers potential information about the intensity of biomass burning events. As AIRS CO retrievals are dominated by mid-tropospheric CO when elevated concentrations are observed there is high confidence that they are due to real CO enhancements at this level. Therefore sharp peaks in mid-tropospheric CO with time could be seen as a proxy for intense biomass burning events, with high CO injection altitudes.

Although MOPITT has been shown to provide superior information about the vertical structure of CO, AIRS offers the benefit of increased spatial coverage. AIRS provides near-global coverage on a daily basis, while MOPITT requires 3 days. This improved coverage makes AIRS more suitable for looking at the horizontal transport of CO in the mid-troposphere. It also offers an advantage for analysis of inter-day and long term variations in regional CO concentrations (as shown in Chapter 6). AIRS is also able to make CO retrievals in the presence of significant cloud cover. As well as improving the coverage in general, this also has potential advantages specific to CO retrievals. CO emissions, particularly from biomass burning, are associated with emissions of aerosols and smoke [Edwards *et al.*, 2004]. In some cases, this smoke may be flagged as cloud by cloud detection algorithms, resulting in loss of information close to the CO source. The cloud clearing method used by AIRS minimises this data loss.

As demonstrated by Crawford *et al.* [2003], CO concentrations over marine regions downstream of continental emissions can be affected by clouds. This is due to the changes in photochemical oxidation rates as a result of the radiative impact of clouds. Crawford *et al.* [2003] propose that satellite observations using only clear-sky data may result in an underestimate of CO concentrations by as much as 15-30 %. Therefore the ability of AIRS to perform CO retrievals in the presence of significant cloud cover may result in improved estimates of CO in such regions.

In this study the potential of AIRS for monitoring CO globally was demonstrated. Despite its relative insensitivity to CO in the lower troposphere, seasonal trends in CO associated with biomass burning were observed. With AIRS observations now spanning a period of over five years, there is great capacity for AIRS data to be used in the analysis of seasonal and inter-annual trends in CO. The Infrared Atmospheric Sounding Interferometer (IASI), launched on board the Metop-A in October 2006, offers high spectral resolution measurements of the outgoing thermal infra-red radiation, similar to those of AIRS. This sensor is the natural successor to AIRS and is to be carried on a series of European Metop satellites over a period of 15 years [Turquety *et al.*, 2004]. As such, IASI is expected to provide a coherent long-term data record, enabling analysis of longer term trends in trace gases such as CO.

The excellent spatial coverage of AIRS also gives it tremendous potential to be used to investigate the horizontal transport of CO in the mid-troposphere. This was demonstrated in Chapter 7, where elevated CO concentrations observed across the Indian Ocean were attributed to extensive biomass burning in Indonesia. In order to further characterise both the horizontal and vertical transport of CO and more accurately attribute it to CO sources, additional work is required. The analysis of Chapter 7, attributes the elevated CO observed over Indonesia to be from biomass burning, based on fire count data and on knowledge of events in the region at the time. Fire counts alone do not provide information about fire intensity, the amount and type of fuel burned, or the emission species. Therefore, further analysis looking at other biomass burning tracers is required to better characterise the source of the elevated CO concentrations.

A great deal of research has been focussed on characterising emissions from biomass burning, a summary of the literature is given by Andreae and Merlet [2001]. As emissions are dependent on the combustion temperature and the fuel composition, analysis of the relative concentrations of multiple emission species can yield information about source of emissions. There are a number of potential emission species that could be used in conjunction with CO that would allow the source of elevated CO concentrations to be confirmed. Some of these, such as CH_4, HCN, and aerosols are routinely observed by satellite instruments and are therefore suitable candidates for use in such work. Edwards *et al.* [2006] demonstrate that satellite observations of CO from MOPITT combined with aerosol optical depth (AOD) and fire count measurements from the Moderate-Resolution Imaging Spectroradiometer (MODIS), can be used to characterise CO sources. In their study Edwards *et al.* [2006] see good correspondence between the timing of peaks in fire counts, CO concentrations and AOD over source regions. High levels of correlation are also observed between enhancements of CO and AOD for distinct biomass burning plumes, a result of direct emissions of CO and carbonaceous aerosol from common sources. Edwards *et al.* [2006] also demonstrate that a combination of measurements (such as CO, AOD, and fire counts) can be used in conjunction with chemical transport models to examine the transport and seasonal variability of pollution from biomass burning. The AIRS CO retrievals are well suited to work of this nature as, like the Terra satellite that houses MOPITT and MODIS, the Aqua payload includes a MODIS sensor alongside AIRS, thus providing a set of coincident and complementary observations.

There is also the potential to use AIRS CO observations in conjunction with retrievals of other emission species to characterise CO sources, by analysis of emission ratios [Andreae and Merlet, 2001]. As the AIRS science team provide a CH_4 (total column) data product, this is one potential emission species that could be used. Although it is not yet an operational product, the AIRS instrument has also been shown to be capable of making observations of tropospheric CO_2 concentrations [Crevoisier *et al.*, 2004]. This gives AIRS the potential to use correlations between CO_2 and CO in the characterisation of emissions. As well as this potential for characterising emissions, the combination of CO_2 and CO observations may also have potential to improve CO_2 surface flux estimates through CO_2:CO correlations, as shown by Palmer *et al.* [2006] using aircraft observations.

The emergence of AIRS and other satellite instruments (e.g. MOPITT, SCIAMACHY, and MLS) since 2000 has generated a wealth of new information about CO in the atmosphere. As the instruments have distinct characteristics and employ different retrieval schemes, they each have something different to add to the knowledge of CO, and are best suited to different applications. In order to maximise the information from these different sources it is necessary to understand well their relative behaviour. This will allow measurements to be combined, or may even allow instruments to be used in synthesis, to improve our knowledge of CO in the atmosphere.

Appendix A – The AIRS v5 CO Product

On 25th July 2007 a new AIRS CO product (v5) was launched by the AIRS science team. Although officially launched in July 2007, the reprocessing of data from earlier years was not completed until December 2007. As the v5 data were not available until such a late stage in the project, all analysis was carried out using the v4 data. Due to the limited time available, the performance of the v5 retrieval was not investigated. Warner *et al.* [2007] compare an intermediate version of the AIRS retrieval scheme with MOPITT retrievals, but do not provide any comparisons with the v4 retrieval. Warner *et al.* [2007] do not offer any insight into any potential improvements in the error estimates from the (intermediate) v5 algorithm. However, they do suggest the magnitude of the CO retrievals is broadly similar to those from v4 and that the new algorithm does not enhance CO retrievals in the lower troposphere. This is shown by the positive bias (10-20 ppbv) in the AIRS 500 hPa CO relative to MOPITT and by the negative bias in total column retrievals over Northern hemisphere land.

Full details of the differences between the v4 and v5 CO retrieval algorithms are given by Olsen *et al.* [2007]. The fundamental methods of the algorithm remain the same but there are significant changes to its implementation. The main changes are in the representation functions and the “first guess” profile. In the v5 algorithm, the CO profile is now represented by nine trapezoids (instead of four), chosen to match the MOPITT vertical levels. The AFGL US standard CO profile used as the “first guess” in v4 has also been replaced, with v5 using the MOPITT *a priori* profile. As well as updating the CO retrieval, changes have also been made to retrievals of other parameters, such as water vapour and surface emissivity. As the UoE CO retrieval uses these level-2 products, any potential improvements in these products may benefit the UoE retrieval.

References

Aglionby, J. (2006), Forest fire haze brings misery to Indonesia and beyond, The Guardian, 06/10/06.

Anderson, G. P., et al. (1986), AFGL atmospheric constituent profiles (0-120 km), Tech. Rep. AFGL-TR-86-0110, Air Force Geophysics Laboratory, Hanscom Air Force Base, Mass.

Andreae, M. O., and P. Merlet (2001), Emission of trace gases and aerosols from biomass burning, *Global Biogeochem Cy*, *15*(4), 955-966.

Arino, O., and S. Plummer (2001), Along Track Scanning Radiometer World Fire Atlas - Validation of the 1997-98 Active Fire Product, European Space Agency, ESRIN, Frascati, Italy.

Aumann, H. H., and L. Strow (2001), AIRS, the First Hyper-Spectral InfraRed Sounder for Operational Weather Forecasting, paper presented at Aerospace Conference, 2001, IEEE, Big Sky, MT, USA, 2001.

Aumann, H. H., et al. (2003), AIRS/AMSU/HSB on the aqua mission: Design, science objectives, data products, and processing systems, *Ieee T Geosci Remote*, *41*(2), 253-264.

Aumann, H. H., et al. (2006), Three years of Atmospheric Infrared Sounder radiometric calibration validation using sea surface temperatures, *J Geophys Res-Atmos*, *111*(D16).

Auvray, M., et al. (2007), A model investigation of tropospheric ozone chemical tendencies in long-range transported pollution plumes, *J Geophys Res-Atmos*, *112*(D5).

Barnet, C. (2005), Overview of the AIRS Science Team Algorithm, NOAA/NESDIS/ORA.

Beer, R. (2006), TES on the Aura mission: Scientific objectives, measurements, and analysis overview, *Ieee T Geosci Remote*, *44*(5), 1102-1105.

Belotti, C., et al. (2006), Retrieval of Tropospheric Carbon Monoxide from MIPAS Measurements, paper presented at ESA - Atmospheric Science Conference, ESA ESRIN, Frascati.

Bettwy, M. (2007), NASA Data Links Indonesian Wildfire Flare-Up to Recent El Nino, NASA, Goddard Space Flight Center.

Bowman, K. W., et al. (2006), Tropospheric emission spectrometer: Retrieval method and error analysis, *Ieee T Geosci Remote*, *44*(5), 1297-1307.

Buchwitz, M., et al. (2005), Carbon monoxide, methane and carbon dioxide columns retrieved from SCIAMACHY by WFM-DOAS: year 2003 initial data set, *Atmos Chem Phys*, *5*, 3313-3329.

Buchwitz, M., et al. (2007), Three years of global carbon monoxide from SCIAMACHY: comparison with MOPITT and first results related to the detection of enhanced CO over cities, *Atmos Chem Phys*.

Chahine, M. T. (1974), Remote Sounding of Cloudy Atmospheres .1. Single Cloud Layer, *J Atmos Sci*, *31*(1), 233-243.

Chan, L. Y., et al. (2000), A case study on the biomass burning in southeast Asia and enhancement of tropospheric ozone over Hong Kong, *Geophys Res Lett*, *27*(10), 1479-1482.

Clerbaux, C., et al. (1999), Retrieval of CO columns from IMG ADEOS spectra, *Ieee T Geosci Remote*, *37*(3), 1657-1661.

Clerbaux, C., et al. (2003), Trace gas measurements from infrared satellite for chemistry and climate applications, *Atmos Chem Phys*, *3*, 1495-1508.

Collins, W. J., et al. (1997), Tropospheric ozone in a global-scale three-dimensional Lagrangian model and its response to NOX emission controls, *J Atmos Chem*, *26*(3), 223-274.

Connors, V. S., et al. (1999), Spaceborne observations of the global distribution of carbon monoxide in the middle troposphere during April and October 1994, *J Geophys Res-Atmos*, *104*(D17), 21455-21470.

Crawford, J., et al. (2003), Clouds and trace gas distributions during TRACE-P, *J Geophys Res-Atmos*, *108*(D21), 8818-8130.

Crevoisier, C., et al. (2004), Midtropospheric CO2 concentration retrieval from AIRS observations in the tropics, *Geophys Res Lett*, *31*(17).

Deeter, M. N., et al. (2003), Operational carbon monoxide retrieval algorithm and selected results for the MOPITT instrument, *J Geophys Res-Atmos*, *108*(D14), 4399-4409.

Deeter, M. N., et al. (2004), Vertical resolution and information content of CO profiles retrieved by MOPITT, *Geophys Res Lett*, *31*(15).

Dudhia, A. (2005), Reference Forward Model (RFM), http://www-atm.physics.ox.ac.uk/RFM/.

Edwards, D. P., et al. (1992), GENLN2: A General Line-by-line Atmospheric Transmittance and Radiance Model. Version 3.0 Description and User's Guide., Report, NCAR, Boulder, CO, USA.

Edwards, D. P., et al. (2004), Observations of carbon monoxide and aerosols from the Terra satellite: Northern Hemisphere variability, *J Geophys Res-Atmos*, *109*(D24).

Edwards, D. P., et al. (2006), Satellite-observed pollution from Southern Hemisphere biomass burning, *J Geophys Res-Atmos*, *111*(D14).

Emmons, L. (2002), MOPITT Data Website, http://web.eos.ucar.edu/mopitt/data/index.html.

Emmons, L., et al. (2004a), Validation of Four Years of MOPITT CO Retrievals with Independent Measurements, in *AGU SO4*, edited.

Emmons, L. K., et al. (2004b), Validation of Measurements of Pollution in the Troposphere (MOPITT) CO retrievals with aircraft in situ profiles, *J Geophys Res-Atmos*, *109*(D3).

ERSL (2007), Earth System Research Laboratory - Global Monitoring Division, http://www.esrl.noaa.gov/gmd/.

Filipiak, M. J., et al. (2005), Carbon monoxide measured by the EOS Microwave Limb Sounder on Aura: First results, *Geophys Res Lett*, *32*(14).

Gaunce, M. (2007), Aura Validation Experiment, http://www.espo.nasa.gov/ave-houston/.

Gerbig, C., et al. (1999), An improved fast-response vacuum-UV resonance fluorescence CO instrument, *J Geophys Res-Atmos*, *104*(D1), 1699-1704.

Gettelman, A., et al. (2004), Validation of Aqua satellite data in the upper troposphere and lower stratosphere with in situ aircraft instruments, *Geophys Res Lett*, *31*(22).

Goody, R. M., and Y. L. Yung (1995), *Atmospheric radiation : theoretical basis*, 2nd ed., xiii,519p pp., Oxford University Press, New York ; Oxford.

Granier, C., et al. (2000), The impact of natural and anthropogenic hydrocarbons on the tropospheric budget of carbon monoxide, *Atmos Environ*, *34*, 5255-5270.

Hannon, S. E., et al. (2006), AIRS SRF File Format, http://asl.umbc.edu/pub/airs/srf/srfhdf.html.

Hauglustaine, D. A., et al. (1998), MOZART, a global chemical transport model for ozone and related chemical tracers 2. Model results and evaluation, *J Geophys Res-Atmos*, *103*(D21), 28291-28335.

Heald, C. L., et al. (2003), Asian outflow and trans-Pacific transport of carbon monoxide and ozone pollution: An integrated satellite, aircraft, and model perspective, *J Geophys Res-Atmos*, *108*(D24).

Heald, C. L., et al. (2004), Comparative inverse analysis of satellite (MOPITT) and aircraft (TRACE-P) observations to estimate Asian sources of carbon monoxide, *J Geophys Res-Atmos*, *109*(D23).

Intergovernmental Panel on Climate Change (2001), *Climate change 2001 : the scientific basis : contribution of Working Group I to the third assessment report of the Intergovernmental Panel on Climate Change*, x, 881 p. pp., Cambridge University Press, Cambridge, UK ; New York.

Intergovernmental Panel on Climate Change (2007), *Climate change 2007: impacts, adaptations and vulnerability*, Cambridge University Press.

Kanakidou, M., and P. J. Crutzen (1999), The photochemical source of carbon monoxide: Importance, uncertainties and feedbacks, *Chemosphere - Global Change Science*, *1,* 91-109.

Kar, J., et al. (2004), Evidence of vertical transport of carbon monoxide from Measurements of Pollution in the Troposphere (MOPITT), *Geophys Res Lett*, *31*(23).

Lamarque, J. F., et al. (1999), Assimilation of Measurement of Air Pollution from Space (MAPS) CO in a global three-dimensional model, *J Geophys Res-Atmos*, *104*(D21), 26209-26218.

Livesey, N., et al. (2008), Validation of Aura Microwave Limb Sounder O3 and CO observations in the upper troposphere and lower stratosphere, *J Geophys Res-Atmos*, *113*.

Logan, J. A., et al. (2008), Effects of the 2006 El Nino on tropospheric composition as revealed by data from the Tropospheric Emission Spectrometer (TES), *Geophys Res Lett*, *35*(3).

Lopez, J. P., et al. (2008), TES carbon monoxide validation during two AVE campaigns using the Argus and ALIAS, *J Geophys Res-Atmos*, *In press*.

Lubrano, A. M., et al. (2000), Simultaneous inversion for temperature and water vapor from IMG radiances, *Geophys Res Lett*, *27*(16), 2533-2536.

Luo, M., et al. (2007), Comparison of carbon monoxide measurements by TES and MOPITT: Influence of a priori data and instrument characteristics on nadir atmospheric species retrievals, *J Geophys Res-Atmos*, *112*.

Matricardi, M., et al. (2001), An improved general fast radiative transfer model for the assimilation of radiance observations., ECMWF.

McConnell, J. C., et al. (1971), Natural Sources of Atmospheric CO, *Nature, 233*(5316), 187-188.

McMillan, W. W., et al. (2005), Daily global maps of carbon monoxide from NASA's Atmospheric Infrared Sounder, *Geophys Res Lett, 32*(11).

Migeotte, M. V. (1949), The Fundamental Band of Carbon Monoxide at 4.7-Mu in the Solar Spectrum, *Phys Rev, 75*(7), 1108-1109.

Newell, R. E., et al. (1999), Atmospheric processes influencing measured carbon monoxide in the NASA Measurement of Air Pollution From Satellites (MAPS) experiment, *J Geophys Res-Atmos, 104*(D17), 21487-21501.

Niu, J. G., et al. (2004), Carbon monoxide total column retrievals by use of the measurements of pollution in the troposphere airborne test radiometer, *Appl Optics, 43*(24), 4685-4696.

Novelli, P. (1999), CO in the atmosphere: measurement techniques and related issues, *Chemosphere - Global Change Science, 1*(1), 115-126.

Novelli, P. C., et al. (1998), Distributions and recent changes of carbon monoxide in the lower troposphere, *J Geophys Res-Atmos, 103*(D15), 19015-19033.

Novelli, P. C., et al. (2003), Reanalysis of tropospheric CO trends: Effects of the 1997-1998 wildfires, *J Geophys Res-Atmos, 108*(D15).

Olivier, J. G. J., et al. (1999), A 1990 global emission inventory of anthropogenic sources of carbon monoxide on 1° ´1° developed in the framework of EDGAR/GEIA, *Chemosphere - Global Change Science, 1*(1), 1-17.

Olsen, E. T., et al. (2007), AIRS/AMSU/HSB Version 5 Changes from Version 4, Jet Propulsion Laboratory, Pasadena, CA.

Palmer, P. I., et al. (2006), Using CO2 : CO correlations to improve inverse analyses of carbon fluxes, *J Geophys Res-Atmos, 111*(D12).

Pfister, G. G., et al. (2008), Contribution of isoprene to chemical budgets: A model tracer study with the NCAR CTM MOZART-4, *J Geophys Res-Atmos, 113*(D5).

Reichle, H. G., et al. (1999), Space shuttle based global CO measurements during April and October 1994, MAPS instrument, data reduction, and data validation, *J Geophys Res-Atmos, 104*(D17), 21443-21454.

Reuters (2006), Hotspots drop in Indonesia but some haze lingers, Reuters, 01/11/06.

Rinsland, C. P., et al. (2006), Nadir measurements of carbon monoxide distributions by the Tropospheric Emission Spectrometer instrument onboard the Aura Spacecraft: Overview of analysis approach and examples of initial results, *Geophys Res Lett*, *33*(22).

Rodgers, C. D. (2000), *Inverse methods for atmospheric sounding: theory and practice*, World Scientific, Singapore ; London.

Rodgers, C. D., and B. J. Connor (2003), Intercomparison of remote sounding instruments, *J Geophys Res-Atmos*, *108*(D3).

Rothman, L. S., et al. (2003), The HITRAN molecular spectroscopic database: edition of 2000 including updates through 2001, *J Quant Spectrosc Ra*, *82*(1-4), 5-44.

Saunders, R., et al. (2007), A comparison of radiative transfer models for simulating Atmospheric Infrared Sounder (AIRS) radiances, *J Geophys Res-Atmos*, *112*(D1).

Shindell, D. T., et al. (2006), Multi-model simulations of carbon monoxide: Comparison with observations and projected near-future changes, *J Geophys Res-Atmos*, *111*.

Strow, L. L., et al. (2003), An overview of the AIRS radiative transfer model, *Ieee T Geosci Remote*, *41*(2), 303-313.

Susskind, J., et al. (2003), Retrieval of atmospheric and surface parameters from AIRS/AMSU/HSB data in the presence of clouds, *Ieee T Geosci Remote*, *41*(2), 390-409.

Taylor, J. (2005), EAQUATE - European AQUA Thermodynamic Experiment, http://ensembles-eu.metoffice.com/met-res/eaquate/.

Turquety, S., et al. (2004), Operational trace gas retrieval algorithm for the Infrared Atmospheric Sounding Interferometer, *J Geophys Res-Atmos*, *109*(D21).

Warner, J., et al. (2007), A comparison of satellite tropospheric carbon monoxide measurements from AIRS and MOPITT during INTEX-A, *J Geophys Res-Atmos*, *112*(D12S17).